# Chapter 3: Adaptive Concurrent Multilevel Model for Multiscale Analysis of Composite Materials Including Damage

Somnath Ghosh

John B. Nordholt Professor, Department of Mechanical Engineering,
The Ohio State University, Columbus, OH, USA

## 3.1 Introduction

The past few decades have seen rapid developments in the science and technology of a variety of advanced heterogeneous materials like polymer, ceramic, or metal matrix composite, functionally graded materials, and porous materials, as well as various alloy systems. Many of these engineered materials are designed to possess optimal properties for different functions, e.g., low weight, high strength, superior energy absorption and dissipation, high impact and penetration resistance, superior crashworthiness, better structural durability, etc. Tailoring their microstructures and properties to yield high structural efficiency has enabled these materials to provide enabling mission capabilities, which has been a key factor in their successful deployment in the aerospace, automotive, electronics, defense, and other industries.

Reinforced composites are constituted of stiff and strong fibers, whiskers or particulates of, e.g., glass, graphite, boron, or aluminum oxide, which are dispersed in primary phase matrix materials made of, e.g., epoxy, steel, titanium, or aluminum. Micrographs of a silicon particulate reinforced aluminum alloy (DRA) and an epoxy matrix composite (PMC), consisting of graphite fibers, are shown in Fig. 3.1. The presence of reinforcing phases generally enhances physical and mechanical properties like strength, thermal expansion coefficient, and wear resistance of the composite.

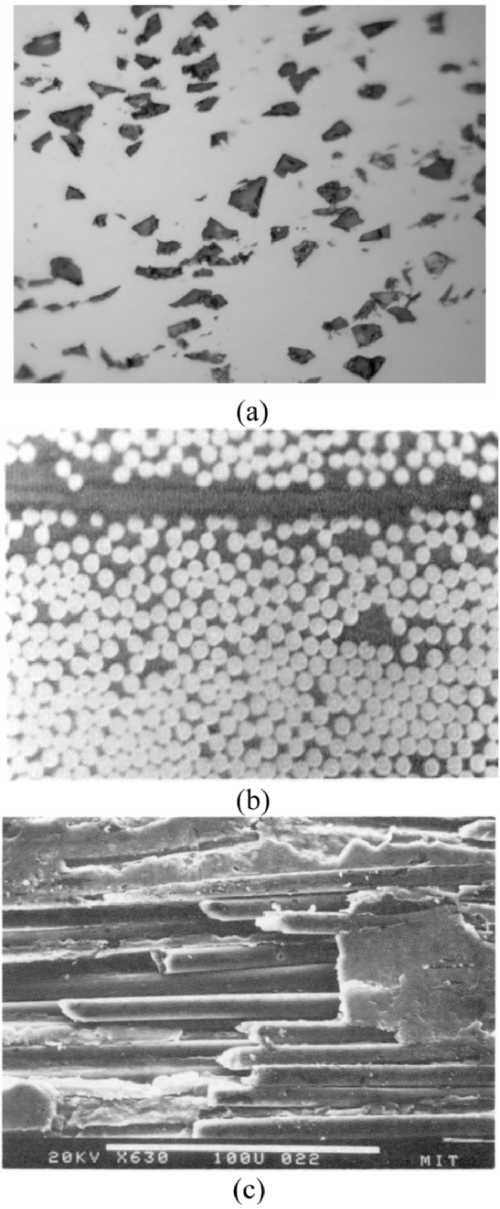


**Fig. 3.1.** Micrographs of (**a**) SiC particle-reinforced aluminum matrix composite showing particle cracking, (**b**) graphite-epoxy, fiber-reinforced polymer matrix composite, (**c**) fiber breakage in a polymer matrix composite

Processing methods, like powder metallurgy or resin transfer molding, often contribute to nonuniformities in microstructural morphology, e.g., in reinforcement spatial distribution, size or shape, or in the constituent material and interface properties. These nonuniformities can influence the degree of property enhancement. However, the presence of the nonuniform microstructural heterogeneities can have a strong adverse effect on their failure properties like fracture toughness, strain to failure, ductility, and fatigue resistance. Damage typically initiates at microstructural "weak spots" by inclusion (fiber or particle) fragmentation or decohesion at the inclusion-matrix interface. The cracks often bifurcate into the matrix and link up with other damage sites and cracks to evolve across larger scales and manifest as dominant cracks that cause structural failure. Structural failure of composite materials is thus inherently a multiple scale phenomenon. Microstructural damage mechanisms and structural failure properties are sensitive to the local variations in morphology, such as clustering, directionality, or connectivity and variations in reinforcement shape or size. Figure 3.1a shows particle and matrix cracking in a SiC-reinforced DRA microstructure, and Fig. 3.1c is the micrograph of a graphite-epoxy PMC showing failure by fiber breakage and matrix rupture. Experimental studies, e.g., in [5, 18], have established that particles in regions of clustering or alignment have a greater propensity toward fracture.

The need for robust design procedures for reliable and effective composite materials provides a compelling reason for the accelerated development of competent modeling methods that can account for the structure–material interaction and relate the microstructure to properties and failure characteristics. The models should accurately represent phenomena at different length scales and also optimize the computational efficiency through effective multiscale domain decomposition.

## 3.2 Homogenization and Multiscale Models

It is prudent to use the notion of multispatial scales in the analysis of composite materials and structures due to the inherent existence of various scales. Conventional methods of analysis have used effective properties obtained from homogenization of response at microscopic length scales. A number of analytical models have evolved within the framework of small deformation linear elasticity theory to predict homogenized macroscale constitutive response of heterogeneous materials, accounting for the characteristics of microstructural behavior. The underlying principle of these models is the Hill–Mandel condition of homogeneity [41], which states

that for large differences in microscopic and macroscopic length scales, the volume averaged strain energy is obtained as the product of the volume averaged stresses and strains in the representative volume element or RVE, i.e.,

$$\int_{\Omega} \sigma_{ij}^{*} \varepsilon_{ij}^{*} \, \mathrm{d}\Omega = \left\langle \sigma_{ij}^{*} \varepsilon_{ij}^{*} \right\rangle = \left\langle \sigma_{ij}^{*} \right\rangle \left\langle \varepsilon_{ij}^{*} \right\rangle. \tag{3.1}$$

Here $\sigma_{ij}^{*}$ and $\varepsilon_{ij}^{*}$ are the general statically admissible stress field and kinematically admissible strain field in the microstructure, respectively, and $\Omega$ is a microstructural volume that is equal to or larger than the RVE. The representative volume element or RVE in (3.1) corresponds to a microstructural subregion that is representative of the entire microstructure in an average sense. For composites, it is assumed to contain a sufficient number of inclusions, which makes the effective moduli independent of assumed homogeneous tractions or displacements on the RVE boundary. The Hill–Mandel condition introduces the notion of a homogeneous material that is energetically equivalent to a heterogeneous material. Cogent reviews of various homogenization models are presented in Mura [9, 52]. Based on the eigenstrain formulation, an equivalent inclusion method has been introduced by Eshelby [22] for stress and strain distributions in an infinite elastic medium containing a homogeneous inclusion. Mori–Tanaka estimates, e.g., in [8], consider nondilute dispersions where inclusion interaction is assumed to perturb the mean stress and strain field. Self-consistent schemes introduced by Hill [40] provide an alternative iterative methodology for obtaining mean field estimates of thermoelastic properties by placing each heterogeneity in an effective medium. Notable among the various estimates and bounds on the elastic properties are the variational approach using extremum principles by Hashin et al. [39] and Nemat-Nasser et al. [53], the probabilistic approach by Chen and Acrivos [14], the self-consistent model by Budiansky [11], the generalized self-consistent models by Christensen and Lo [16], etc. These predominantly analytical models, however, do not offer adequate resolution to capture the fluctuations in microstructural variables that have significant effects on properties. Also, arbitrary morphologies, material nonlinearities, or large property mismatches in constituent phases cannot be adequately treated.

The use of computational micromechanical methods like the finite element method, boundary element method, spring lattice models, etc. has become increasingly popular for accurate prediction of stresses, strains, and other evolving variables in composite materials [9, 10, 83]. Within the framework of computational multispatial scale analyses of heterogeneous materials, two classes of methods have emerged, depending on the nature of coupling between the scales. The first group, known as “hierarchical

models" [17, 23, 30, 31, 37, 43, 63, 77, 78] entails bottom-up coupling in which information is passed unidirectionally from lower to higher scales, usually in the form of effective material properties. A number of hierarchical models have incorporated the asymptotic homogenization theory developed by Benssousan [7], Sanchez-Palencia [68], and Lions [47] in conjunction with computational micromechanics models. Homogenization implicitly assumes uniformity of macroscopic field variables. Uncoupling of governing equations at different scales is achieved through incorporation of periodicity boundary conditions on the microscopic representative volume elements or RVEs, implying periodic repetition of a local microstructural region. Consequently, the models are used to predict evolution of variables at the macroscopic scale using homogenized constitutive relations, as well as in the periodic microstructural RVE. The latter analysis can be conducted as a postprocessor to the macroscopic analysis with macroscopic strain as the input. Hierarchical multiscale computational analyses of reinforced composites have been conducted by, e.g., Fish et al. [23], Kikuchi et al. [37], Terada et al. [78], Tamma and Chung [17, 77], and Ghosh et al. [30, 31, 43]. Hierarchical models involving homogenization for damage in composites have also been developed by Ghosh et al. in [63, 65] from the microstructural Voronoi cell FEM model, Lene et al. [21, 44], Fish et al. [25], and Allen et al. [2, 3, 20], among others.

While the "bottom-up" hierarchical models are efficient and can accurately predict macroscopic or averaged behavior, such as stiffness or strength, their predictive capabilities are limited with problems involving localization, failure, or instability. Macroscopic uniformity of response variables, like stresses or strains, is not a suitable assumption in regions of high gradients like free edges, interfaces, material discontinuities, or in regions of localized deformation and damage. On the other hand, RVE periodicity is unrealistic for nonuniform microstructures, e.g., in the presence of clustering of heterogeneities or localized microscopic damage. Even with a uniform phase distribution in the microstructure, the evolution of localized stresses, strains, or damage path can violate periodicity conditions. Such shortcomings for composite material modeling have been discussed for modeling heterogeneous materials by Pagano and Rybicki [58, 67], Oden and Zohdi [55, 84], Ghosh et al. [35, 62, 64], Fish et al. [24]. The solution of micromechanical problems in the vicinity of stress singularity was suggested in [58, 67] in the context of composite laminates with free edges. These problems have been effectively tackled by the second class of models known as "concurrent" multiscale modeling methods [24, 29, 35, 36, 51, 55, 56, 58, 61, 62, 64, 67, 71, 79, 82, 84].

Concurrent multiscale models differentiate between regions requiring different resolutions to invoke two-way (bottom-up and top-down) coupling

of scales in the computational domain. These models provide effective means for analyzing heterogeneous materials and structures involving high solution gradients. Substructuring allows for macroscopic analysis using homogenized material properties in some parts of the domain while zooming in at selected regions for detailed micromechanical modeling. Macroscopic analysis, using bottom-up homogenization in regions of relatively benign deformation, enhances the efficiency of the computational analysis due to the reduced order models with limited information on the microstructural morphology. The top-down localization process, on the other hand, incorporates cascading down to the microstructure in critical regions of localized damage or instability. These regions need explicit representation of the local microstructure, and micromechanical analysis is conducted for accurately predicting localization or damage path. Microscopic computations involving complex microstructures are often intensive and computationally prohibitive. Selective microstructural analysis in the concurrent setting makes the overall computational analysis feasible, provided the "zoom-in" regions are kept to a minimum.

A variety of alternative methods have been explored for adaptive concurrent multiscale analysis in [51, 55, 56, 84, 79, 82]. Concurrent multiscale analysis using adaptive multilevel modeling with the microstructural Voronoi cell FEM model has been conducted by Ghosh et al. [29, 35, 36, 61, 62, 64] for modeling composites with free edges or with evolving damage resulting in dominant cracks. Guided by physical and mathematical considerations, the introduction of adaptive multiple scale modeling is a desirable feature for optimal selection of regions requiring different resolutions to minimize discretization and modeling errors. Ghosh and coworkers have also developed adaptive multilevel analysis using the microstructural Voronoi cell FEM model for modeling elastic–plastic composites with particle cracking and porosities in [35] and for elastic composites with debonding at the fiber–matrix interface in [29, 36]. This chapter is devoted to a discussion of adaptive concurrent multiple scale models developed by the author for composites with and without damage.

## 3.3 Multilevel Computational Model for Concurrent Multiscale Analysis of Composites Without Damage

A framework of an adaptive multilevel model is presented for macroscale to microscale analysis of composite materials in the absence of microstructural damage. The model consists of three levels of hierarchy, as shown in Fig. 3.2. These are:

(1) *Level-0* macroscopic computational domain of Fig. 3.2b using material properties that are obtained by homogenizing the material response in the microstructural RVE of Fig. 3.2a.
(2) *Level-1* computational domain of macroscopic analysis that is followed by a postprocessing operation of microscopic RVE analysis. This level, shown in Fig. 3.2c, is used to decipher whether RVE-based homogenization is justified in this region.
(3) *Level-2* computational domain of pure microscopic analysis, where the assumption of the microscopic RVE for homogenization is not valid.
(4) *Intermediate transition layer* sandwiched between the macroscopic (*level-0/level-1*) and microscopic (*level-2*) computational domains.

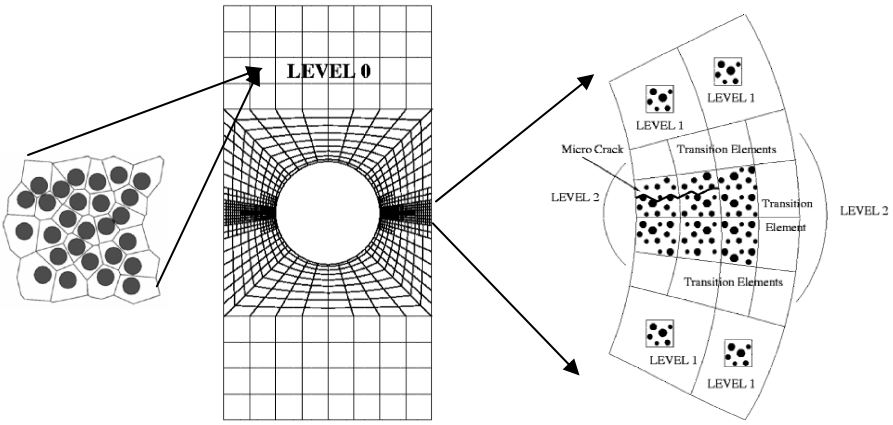


**Fig. 3.2.** An adaptive two-way coupled multiscale analysis model: (**a**) RVE for constructing continuum models for *level-0* analysis, (**b**) a *level-0* model with adaptive zoom-in, (**c**) zoomed-in *level-1*, *level-2 and transition layers*

Physically motivated error indicators are developed for transitioning from macroscopic to microscopic analysis and tested against mathematically rigorous error bounds. All microstructural computations of arbitrary heterogeneous domains are conducted using the adaptive Voronoi cell finite element model [26, 34, 48–50].

### 3.3.1 Hierarchy of Domains for Heterogeneous Materials

Consider a heterogeneous domain composed of multiple phases of linear elastic materials, which occupies an open bounded domain $\Omega_{\text{het}} \subset \mathfrak{R}^3$, with a Lipschitz boundary $\partial\Omega_{\text{het}} = \Gamma_u \bigcup \Gamma_t, \Gamma_u \bigcap \Gamma_t = \varnothing$. $\Gamma_u$ and $\Gamma_t$ corresponds to displacement and traction boundaries, respectively. The

body forces $\boldsymbol{f} \in L^2(\Omega_{\text{het}})$ and surface tractions $\boldsymbol{t} \in L^2(\Omega_{\text{het}})$ are vector-valued functions. The multilevel computational model for this domain uses problem descriptions for two types of domains.

### *Micromechanics problem for the heterogeneous domain* $\Omega_{\text{het}}$

The micromechanics problem for the entire domain includes explicit consideration of multiple phases in $\Omega_{\text{het}}$ with the location dependent elasticity tensor $\boldsymbol{E}(\boldsymbol{x})$, which is a bounded function in $\mathfrak{R}^{9\times 9}$ that satisfies conventional conditions of ellipticity (positive strain energy for admissible strain fields) and symmetry. The displacement field **u** for the actual problem can be obtained as the solution to the conventional statement of principle of virtual work, expressed as

$$\text{Find}\,\mathbf{u}, \mathbf{u}|_{\Gamma_{\mathbf{u}}} = \bar{\mathbf{u}},$$

such that

$$\int_{\Omega_{\text{het}}} \nabla \mathbf{v} : \mathbf{E} : \nabla \mathbf{u}\, \mathrm{d}\Omega = \int_{\Omega_{\text{het}}} \mathbf{f} \cdot \mathbf{v}\, \mathrm{d}\Omega + \int_{\Gamma_t} \mathbf{t} \cdot \mathbf{v}\, \mathrm{d}\Gamma \quad \forall \mathbf{v} \in \mathbf{V}(\Omega_{\text{het}}), \tag{3.2}$$

where $\mathbf{V}(\Omega)$ is a space of admissible functions defined as

$$\mathbf{V}(\Omega) = \{\mathbf{v} : \mathbf{v} \in \mathbf{H^1}(\Omega); \mathbf{v}|_{\Gamma_{\mathbf{u}}} = 0\}. \tag{3.3}$$

For heterogeneous materials with a distribution of different phases, such as fibers, particles, or voids, the constituent material properties $\boldsymbol{E}(\boldsymbol{x})$ may vary considerably with spatial position. Consequently, conventional finite element models are likely to incorporate inordinately large meshes for accuracy, which results in expensive computations. A regularized version of the actual problem, using homogenization methods can be of significant value in reducing the computing efforts through reduced order models.

### *Regularized problem in a homogenized domain* $\Omega_{\text{hom}}$

A regularized solution $\mathbf{u}^H$ to the actual problem can be obtained by using a homogenized linear elasticity tensor $\boldsymbol{C}^H(\boldsymbol{x})$ in solving the boundary value problem, which is characterized by the principle of the virtual work:

$$\text{Find}\,\mathbf{u}^H, \mathbf{u}^H|_{\Gamma_{\mathbf{u}}} = \bar{\mathbf{u}}$$

such that

$$\int_{\Omega_{\text{hom}}} \nabla \mathbf{v} : \boldsymbol{C}^H : \nabla \mathbf{u}^H \, \mathrm{d}\Omega = \int_{\Omega_{\text{hom}}} \mathbf{f} \cdot \mathbf{v} \, \mathrm{d}\Omega + \int_{\Gamma_{\mathbf{t}}} \mathbf{t} \cdot \mathbf{v} \, \mathrm{d}\Gamma \quad \forall \mathbf{v} \in \mathbf{V}(\Omega_{\text{hom}}). \tag{3.4}$$

The homogenized elasticity tensor is assumed to satisfy symmetry and ellipticity conditions, and it is required to produce an admissible stress field $\boldsymbol{\sigma}^H (= \boldsymbol{C}^H : \nabla \mathbf{u}^H)$ satisfying the traction boundary condition: $\boldsymbol{n} \cdot \boldsymbol{\sigma}^H = \mathbf{t}(\boldsymbol{x}) \; \forall \, \boldsymbol{x} \in \Gamma_t$. Determination of statistically homogeneous material parameters requires an isolated representative volume element or RVE $Y(\boldsymbol{x}) \subset \mathfrak{R}^3$, over which averaging can be performed. The resulting field variables like stresses and strains are also statistically homogeneous in the RVE and may be obtained from volumetric averaging as

$$\sigma^H = \frac{1}{|Y|} \int_Y \sigma(\mathbf{y}) \, \mathrm{d}Y, \quad \varepsilon^H = \frac{1}{|Y|} \int_Y \varepsilon(\mathbf{y}) \, \mathrm{d}Y, \qquad |Y| = \int_Y \mathrm{d}Y. \tag{3.5}$$

In classical methods of estimating homogenized elastic moduli $\boldsymbol{C}^H(\boldsymbol{x})$, the RVE is subjected to prescribed surface displacements or tractions, which in turn produce uniform stresses or strains in a homogenous medium. Various micromechanical theories have been proposed to predict the overall constitutive response by solving RVE-level boundary value problems, followed by volumetric averaging [9, 52]. The scale of the RVE $Y(\boldsymbol{x})$ is typically very small in comparison with the dimension $L$ of the structure. The asymptotic homogenization theory, proposed in [7, 47, 68], is also effective in multiscale modeling of physical systems that contain multiple length scales. This method is based on asymptotic expansion of the solution fields, e.g., displacement and stress fields, in the microscopic spatial coordinates about their respective macroscopic values. The composite microstructure in the RVE is assumed to be locally $Y$-periodic. Correspondingly, any variable $\boldsymbol{f}^\varepsilon$ in the RVE is also assumed to be $Y$-periodic, i.e., $\boldsymbol{f}^\varepsilon(\boldsymbol{x}, \boldsymbol{y}) = \boldsymbol{f}^\varepsilon(\boldsymbol{x}, \boldsymbol{y} + \boldsymbol{k}\boldsymbol{Y})$. Here $\boldsymbol{y} = \boldsymbol{x}/\varepsilon$ corresponds to the microscopic coordinates in $Y(\boldsymbol{x})$. Here, $\varepsilon \ll 1$ is a small positive number representing the ratio of microscopic to macroscopic length scales, and $\boldsymbol{k}$ is a $3 \times 3$ array of integers. Superscript $\varepsilon$ denotes the association with both length scales $(\boldsymbol{x}, \boldsymbol{y})$. In homogenization theory, the displacement field is asymptotically expanded about $\boldsymbol{x}$ with respect to the parameter $\varepsilon$ as

$$u_i^{\varepsilon}(\boldsymbol{x}) = u_i^0(\boldsymbol{x},\boldsymbol{y}) + \varepsilon u_i^1(\boldsymbol{x},\boldsymbol{y}) + \varepsilon^2 u_i^2(\boldsymbol{x},\boldsymbol{y}) + \cdots. \tag{3.6}$$

Since the stress tensor is obtained from the spatial derivative of $u_i^{\varepsilon}(\boldsymbol{x})$ as

$$\sigma_{ij}^{\varepsilon}(\boldsymbol{x},\boldsymbol{y}) = \frac{\mathbf{1}}{\varepsilon}\sigma_{ij}^0(\boldsymbol{x},\boldsymbol{y}) + \sigma_{ij}^1(\boldsymbol{x},\boldsymbol{y}) + \varepsilon\sigma_{ij}^2(\boldsymbol{x},\boldsymbol{y}) + \varepsilon^2\sigma_{ij}^3(\boldsymbol{x},\boldsymbol{y}) + \cdots, \tag{3.7}$$

where

$$\sigma_{ij}^0 = C_{ijkl}^{\varepsilon}\frac{\partial u_k^0}{\partial y_t}, \quad \sigma_{ij}^1 = C_{ijkl}^{\varepsilon}\left(\frac{\partial u_k^0}{\partial x_t} + \frac{\partial u_k^1}{\partial y_t}\right), \quad \sigma_{ij}^2 = C_{ijkl}^{\varepsilon}\left(\frac{\partial u_k^1}{\partial x_t} + \frac{\partial u_k^2}{\partial y_t}\right). \tag{3.8}$$

By applying periodicity conditions on the RVE boundary, i.e., $\int_{\partial Y}\sigma_{ij}n_j\,\mathrm{d}\partial Y = 0$, it is possible to decouple the governing equations into a set of microscopic and macroscopic problems, respectively. These are:

***Microscopic equations***

$$\begin{aligned} &\frac{\partial\hat{\sigma}_{ij}^{kl}(\boldsymbol{y})}{\partial y_j} = 0 && \text{(Equilibrium)},\\ &\hat{\sigma}_{ij}^{kl}(\boldsymbol{y}) = C^{\varepsilon}{}_{ijpm}\left[\delta_{kp}\delta_{lm} + \frac{\partial\chi^{kl}{}_p}{\partial y_m}\right] && \text{(Constitutive)}. \end{aligned} \tag{3.9}$$

The superscripts $k$ and $l$ in (3.9) correspond to the components of the macroscopic strain that cause the microscopic stress components $\hat{\sigma}_{ij}^{kl}$. The subscripts $i$, $j$, etc. in this equation on the other hand correspond to microscopic tensor components.

***Macroscopic equations***

$$\begin{aligned} &\frac{\partial\Sigma_{ij}(\boldsymbol{x})}{\partial x_j} + f_i = 0 && \text{(Equilibrium)},\\ &\Sigma_{ij}(\boldsymbol{x}) = \frac{1}{|Y|}\left[\int_Y C_{ijkl}^{\varepsilon}\left(\delta_{km}\delta_{lm} + \frac{\partial\chi_k^{mn}}{\partial y_l}\right)\mathrm{d}Y\right]\frac{\partial u_m^0}{\partial x_n} = C_{ijmn}^H e_{mn}(\boldsymbol{x}) && \text{(Constitutive)}. \end{aligned} \tag{3.10}$$

The interscale transfer operators in these relations are defined as

$$\sigma_{ij}^{1} = \hat{\sigma}_{ij}^{kl}(\boldsymbol{y})\frac{\partial u_k^0}{\partial x_t}(\boldsymbol{x}) \quad \text{(Stress–strain)},$$

$$u_i^1 = \chi_i^{kl}(\boldsymbol{y})\frac{\partial u_k^0}{\partial x_l}(\boldsymbol{x}) \quad \text{(Strain–displacement)}. \tag{3.11}$$

In (3.9)–(3.11), $\chi_i^{kl}$ is a *Y*-periodic function representing the characteristic modes of deformation in the RVE and

$$\Sigma_{ij}(\boldsymbol{x}) = \left\langle \sigma^{\varepsilon}{}_{ij}(\boldsymbol{x},\boldsymbol{y}) \right\rangle_Y, \quad e_{ij}(\boldsymbol{x}) = \frac{1}{2}\left\{ \frac{\partial u_i^0}{\partial x_j} + \frac{\partial u_j^0}{\partial x_i} \right\} = \left\langle e^{\varepsilon}{}_{ij}(\boldsymbol{x},\boldsymbol{y}) \right\rangle_Y \tag{3.12}$$

are homogenized macroscopic stress and strain tensors, respectively, that are obtained by volumetric averaging. The asymptotic homogenization method provides good convergence characteristics with respect to certain norms, in addition to bounds on effective properties. Solutions of RVE boundary value problems with imposed unit macroscopic strains are used in the calculation of the anisotropic homogenized elasticity tensor $C^H{}_{ijkl}(\boldsymbol{x})$. The RVE boundaries are subjected to periodicity conditions, implying that all boundary nodes separated by the periods $Y_1$, $Y_2$, $Y_3$ along the three orthogonal coordinate directions will follow the displacement constraints:

$$u_i(x_1, x_2, x_3) = u_i(x_1 \pm k_1 Y_1, x_2 \pm k_2 Y_2, x_3 \pm k_3 Y_3), \quad i = 1,2,3. \tag{3.13}$$

Following macroscopic analysis with the homogenized moduli $C_{ijkl}{}^H(\boldsymbol{x})$, numerical simulations of the RVE boundary value problems yield stresses and strains in the microstructural RVE.

#### *Limitations of the regularized problem in* $\Omega_{\text{hom}}$

Limitations in solving the regularized problem for variables in heterogeneous microdomains arise from assumptions of relatively uniform macroscopic fields and periodicity of the RVE. In uncoupling the macroscopic problem in $\Omega_{\text{hom}}$ from the microscopic RVE problem in *Y*, it is assumed that the RVE has infinitesimal dimensions in comparison with the macroscopic scale, i.e., $\varepsilon \to 0$. While solutions of the problems in $\Omega_{\text{hom}}$ approach those for the actual domain $\Omega_{\text{het}}$ in this limit, considerable differences may result when the scale factor $\varepsilon$ is finite and the RVE solutions are not periodic. The occurrence of such errors is significant in regions of high local gradients, free edges, or discontinuities.

### 3.3.2 Multiple Levels Coupling Multiple Scales

In the multilevel methodology developed in Ghosh et al. [35, 62, 64], the overall heterogeneous computational domain is adaptively decomposed into a set of nonintersecting open subdomains, which may each belong to one of $\Omega_{\text{het}}$ (domain for microscopic analysis) $\Omega_{\text{hom}}$ (regularized domain for macroscopic analysis), or to a combination thereof. The resulting computational domain $\overline{\Omega}_{\text{het}}$ may be expressed as the union of subdomains belonging to different levels expressed as

$$\begin{aligned}
&\overline{\Omega}_{\text{het}} = \bigcup_{k=1}^{N_0} \Omega_k^{l0} \cup \bigcup_{k=1}^{N_1} \Omega_k^{l1} \cup \bigcup_{k=1}^{N_2} \Omega_k^{l2} \cup \bigcup_{k=1}^{N_{\text{tr}}} \Omega_k^{\text{tr}}, \quad \text{where} \quad \Omega_k^{l0} \cap \Omega_l^{l0} = 0, \\
&\Omega_k^{l1} \cap \Omega_l^{l1} = 0, \quad \Omega_k^{l2} \cap \Omega_l^{l2} = 0, \quad \Omega_k^{\text{tr}} \cap \Omega_l^{\text{tr}} = 0 \quad \forall k \neq l, \\
&\text{and } \Omega_k^{l0} \cap \Omega_l^{l1} = 0, \quad \Omega_k^{l0} \cap \Omega_l^{l2} = 0, \quad \Omega_k^{l1} \cap \Omega_l^{l2} = 0, \\
&\Omega_k^{l1} \cap \Omega_l^{\text{tr}} = 0 \quad \forall k,l.
\end{aligned} \tag{3.14}$$

Here the superscripts $l0$, $l1$, and $l2$ correspond to *level-0*, *level-1*, or *level-2* subdomains in the computational hierarchy; and superscripts tr correspond to the transition region between *level-0/1* and *level-2* subdomains. Computations in different levels require different algorithmic treatments. The number of levels may not exactly correspond to the number of scales, even though they are connected to individual scales. The constituent subdomains, e.g., $\Omega_k^{l0}$ need not be contiguous and may occupy disjoint locations in $\overline{\Omega}_{\text{het}}$. However, certain restrictions apply with respect to sharing of contiguous subdomain boundaries. If $\partial\Omega_k^{l1}, \partial\Omega_k^{l1}, \partial\Omega_k^{l2}$ and $\partial\Omega_k^{\text{tr}}$ represent boundaries of the corresponding level subdomains, then,

- $\partial\Omega_k^{l0} \cap \partial\Omega_l^{l1} = \partial\Omega_{kl}^{l0-l1} \quad \forall k,l$. Also $\partial\Omega_{kl}^{l0-l1}$ has the same characteristics as $\partial\Omega_k^{l0}$ or $\partial\Omega_l^{l1}$, since $\partial\Omega_k^{l0}$ and $\partial\Omega_l^{l1}$ have compatible displacements.
- $\partial\Omega_k^{l0} \cap \partial\Omega_l^{l2} = 0 \quad \forall k,l$, i.e., $\partial\Omega_k^{l0}$ and $\partial\Omega_l^{l2}$ are not contiguous or may not share common edges.
- $\partial\Omega_k^{l2} \cap \partial\Omega_l^{\text{tr}} = \partial\Omega_{kl}^{l2-\text{tr}} \quad \forall k,l$. Also $\partial\Omega_{kl}^{l2-\text{tr}}$ has the same characteristics as $\partial\Omega_k^{l2}$, since $\partial\Omega_k^{l2}$ and $\partial\Omega_l^{\text{tr}}$ have compatible displacements.
- $\partial\Omega_k^{l0/l1} \cap \partial\Omega_l^{\text{tr}} = \partial\Omega_{kl}^{l0/l1-\text{tr}} \quad \forall k,l$. Also the interfaces of $\partial\Omega_k^{l0/l1}$ and $\partial\Omega_l^{\text{tr}}$ are not compatible in general, and hence special constraint conditions need to be developed for $\partial\Omega_{kl}^{l0/l1-\text{tr}}$.

A few cycles in the iterative solution process are required to settle into an "optimal" distribution of the computational levels, even for linear elastic problems. The three levels of computational hierarchy, in the order of sequence of evolution are discussed next.

***Computational subdomain level-0*** $\Omega^{l0}$

Macroscopic analysis with homogenized properties is performed in the *level-0* subdomain. Unless the microstructural morphology suggests strong nonperiodicity, the computational model can generally start with the assumption that $\bar{\Omega}_{\text{het}} = \Omega^{l0}\left(=\bigcup_{k=1}^{N_0}\Omega_k^{l0}\right) \subset \Omega_{\text{hom}}$, i.e., all elements belong to the *level-0* subdomain. This subdomain assumes relatively uniform deformation with "statistically" periodic microstructures, where the regularized problem formulation is nearly applicable. Upon establishing a representative volume element $Y(\boldsymbol{x})$ for the material at a point $\boldsymbol{x}$, the asymptotic expansion-based homogenization method is implemented to yield an assumed orthotropic homogenized elasticity tensor $C^H{}_{ijkl}(\mathbf{x})$ from (3.10). Components of $C^H{}_{ijkl}(\boldsymbol{x})$ for plane problems are calculated from the solution of three separate boundary value problems of the RVE with periodic boundary conditions and imposed unit macroscopic strains given as

$$\begin{Bmatrix} e_{11} \\ e_{22} \\ e_{12} \end{Bmatrix} = \begin{Bmatrix} 1 \\ 0 \\ 0 \end{Bmatrix}, \quad \begin{Bmatrix} e_{11} \\ e_{22} \\ e_{12} \end{Bmatrix} = \begin{Bmatrix} 0 \\ 1 \\ 0 \end{Bmatrix}, \quad \begin{Bmatrix} e_{11} \\ e_{22} \\ e_{12} \end{Bmatrix} = \begin{Bmatrix} 0 \\ 0 \\ 1 \end{Bmatrix}. \tag{3.15}$$

The homogenized elastic stiffness components $C^H{}_{1111}$, $C^H{}_{2222}$, $C^H{}_{1212}$, $C^H{}_{1133}$, $C^H{}_{2233}$, and $C^H{}_{1122}$ are calculated from the volume averaged stresses $\Sigma_{ij}$ according to (3.10). In the event that the elastic coefficient $C^H{}_{3333}$ is needed, a fourth boundary value problem should be solved with $\left(e_{11,}e_{22,}e_{12,}e_{33}\right)^{\mathrm{T}} = (0,0,0,1)^{\mathrm{T}}$. Since the microstructure and the corresponding RVE can change from element to element $\left(E_{l0} \in \Omega^{l0}\right)$ in the computational domain, each element $E_{l0}$ should be assigned its location specific RVE $Y(\boldsymbol{x})$. Drastically different moduli in adjacent elements could lead to nonphysical stress concentrations. Smoothing schemes may be needed for regularization in these regions for macroscopic analysis. However, switching levels can enable a smooth transition from one RVE to another through the introduction of intermediate *level-2* regions.

***Level-0 mesh enrichment by h- and hp-adaptation***

Computational models in the level-0 subdomains are enhanced adaptively by selective *h*- or *hp*-mesh refinement strategy based on suitably chosen "error" criteria. Local enrichment through successive mesh refinement or interpolation function augmentation serves a dual purpose in the multilevel computational strategy. The first goal is to identify regions of high discretization "error" and improve convergence through mesh enhancement in a finite element subspace $\mathbf{V}_{\text{adap}} \subset \mathbf{V}$ with the requirement

Find $\mathbf{u}^{\text{H}}_{\text{adap}}, \mathbf{u}^{\text{H}}_{\text{adap}}|_{\Gamma_{\mathbf{u}}} = \bar{\mathbf{u}}$, satisfying:

$$\int_{\Omega_{\text{hom}}} \nabla \mathbf{v} : \mathbf{E}^{\mathbf{H}} : \nabla \mathbf{u}^{\text{H}}_{\text{adap}} \, \text{d}\Omega = \int_{\Omega_{\text{hom}}} \mathbf{f} \cdot \mathbf{v} \, \text{d}\Omega + \int_{\Gamma_t} \mathbf{t} \cdot \mathbf{v} \, \text{d}\Gamma \quad \forall \mathbf{v} \in \mathbf{V}_{\text{adap}} \tag{3.16}$$

such that $\left\| \mathbf{u}^{\text{H}} - \mathbf{u}^{\text{H}}_{\text{adap}} \right\| \leq$ preset tolerance.

The second is to identify regions of high modeling error due to limitations of the regularized problem in representing the heterogeneous domain and to zoom in on these regions to create higher resolution. These regions are generally characterized by large solution gradients and localization of regularized macroscopic variables. Element refinement is helpful in reducing the length-scale disparity between macroscopic elements in $\Omega_{\text{hom}}$ and the local microstructure $\Omega_{\text{het}}$.

In [35, 64], the *h*-adaptation procedure has been used to subdivide macroscopic elements into smaller elements in regions of high stress or strain gradients, while keeping the order of interpolation fixed. The rate of convergence of this method for nonsmooth domains is quite limited, especially with solution singularities, e.g., in Szabo and Babuska [74]. As a remedy, the *hp*-version of finite element refinement has been established [1]. This method is capable of producing exponentially fast convergence in the finite element approximations to the energy norm for solutions of linear elliptic boundary value problems on nonsmooth domains, such as those with singularities. The rate of convergence of the *hp*-finite element model is estimated by the inequality

$$\left\| \mathbf{u} - \mathbf{u}^{hp}_{fe} \right\| \leq C h^{\mu} p^{-(m-1)} \left\| u \right\|, \tag{3.17}$$

where *h* is the mesh size, *p* is the order of interpolation polynomial, *m* corresponds to the regularity of the solution, *C* is a constant and $\mu = \min(p, m-1)$. The parameter *m* dictates the distribution and sequence of *h*- and *p*-refinements in the *hp*-adaptation scheme. Smaller *m* leads to

algebraic rates, while large $m$ for smooth solutions yield exponential rate of convergence with successive $p$-refinements. The adaptation scheme follows the criteria: Perform $p$-refinement if $p+2 \le m$; and perform $h$-refinement if $p+2 > m$.

It is necessary to solve a sequence of element level regularized boundary value problems in $\Omega_{\text{hom}}$ to estimate the local regularity parameter $m$. If $\boldsymbol{\phi}_{p+q}(k)$ characterizes the error estimator in the FE space $Y_{p+q}(k)$ for the $k$th element, using polynomials of order $p+q$ ($q$ is the enhancement), i.e.,

$$B_k(\boldsymbol{\phi}_{p+q}, \mathbf{v}) = -\int_{\Omega^k{}_{\text{hom}}} \nabla \mathbf{v} : (\mathbf{E}^{\mathbf{H}} \nabla \mathbf{u}^{\text{H}}_{\text{fem}} \, \mathrm{d}\Omega + \int_{\Omega^k{}_{\text{hom}}} \mathbf{f} \cdot \mathbf{v} \, \mathrm{d}\Omega + \int_{\partial\Omega^k{}_{\text{hom}}} \mathbf{g}_k \cdot \mathbf{v} \, \mathrm{d}\partial\Omega \quad \forall \mathbf{v} \in Y_{p+q}(k), \tag{3.18}$$

where $\mathbf{g}_k = \frac{1}{2}[\boldsymbol{\sigma}_k \cdot \mathbf{n}_k + \boldsymbol{\sigma}_{k'} \cdot \mathbf{n}_k] \in \partial\Omega^k_{\text{hom}} \bigcap \partial\Omega^{k'}_{\text{hom}}$

and $\mathbf{g}_k = \mathbf{t} \in \partial\Omega^k_{\text{hom}} \bigcap \Gamma_t$ is the approximate traction on $\partial\Omega^k_{\text{hom}}$. (3.19)

Here $\boldsymbol{\phi}_{p+q}(k)$ is interpreted as the finite element approximation to the true error $\mathbf{e}(k) = \mathbf{u}^H - \mathbf{u}^H_{\text{fem}}$ in element $k$, such that the total error is bounded by the sum of the element-wise error estimators $\|\mathbf{e}\|^2 \le \sum_k \|\boldsymbol{\phi}\|^2_k$. The parameter $m$ is estimated by solving the local element boundary value problem in (3.18) for three successive values of $q$ and solving for $C_k$, $m$ and $\|\boldsymbol{\phi}\|_k$ from the approximate convergence criterion.

### *A numerical example of the regularized problem*

Convergence of the *hp*-adaptive refinement is explored for a composite laminate (Fig. 3.3a) in this example. The top half of the laminate (above A-A) consists of 30.7% volume fraction of silicon carbide fibers in an epoxy matrix with homogenized orthotropic elasticity matrix (in GPa) as $C^H{}_{1111} = 9.1$, $C^H{}_{2222} = 9.1$, $C^H{}_{1212} = 2.3$, $C^H{}_{1133} = 3.7$, $C^H{}_{2233} = 4.1$, and $C^H{}_{1122} = 104.2$. The bottom half consists of a monolithic matrix material with properties $E_{\text{epoxy}} = 3.45$ GPa, $\nu_{\text{epoxy}} = 0.35$. Due to symmetry in the *xz* and *yz* planes, only one quarter of the laminate is modeled. Symmetric boundary conditions are employed on the surfaces $x = 0$ and $y = 0$, and the top and right surfaces are assumed to be traction free.

The regularized laminate problem is subsequently analyzed using the *h*- and *hp*-adapted *level-0* finite element codes, subjected to constant axial strain $\varepsilon_{zz} = 1.0$ in the out-of-plane direction. While the analytical transverse stress $\sigma_{yy}$ is approximately two orders lower compared to the leading order stress $\sigma_{zz}$, it exhibits a singularity of the form $\sigma_{yy} = C_s r^{\lambda+1}$ near the interface-free edge juncture $A$ ($x/h = 4$). Here $r$ is the distance from the singular point at the free edge and $C_s$ is a constant along each radial line at a fixed angle $\theta$, depending on material properties. The exponent $\lambda$ has been evaluated to be 0.9629358 in [6] from traction and displacement continuity at the material interface and traction free conditions on edges. The initial mesh consists of 200 QUAD4 elements. Adaptations are performed in each element until the element error meets the criterion $\|\phi\|_k \leq 0.25\|\phi\|_{\max}$. The *h*- and *hp*-adapted mesh are shown in Figs. 3.2c and 3.3a, respectively. Following iterative cycles, the converged *h*-adapted mesh consists of 1,664 elements with 3,282 degrees of freedom, while the converged *hp*-adapted mesh consists of 344 elements with 1,834 degrees of freedom. The smallest element size in both cases is $0.0025h_e$, where $h_e$ is the initial element size.

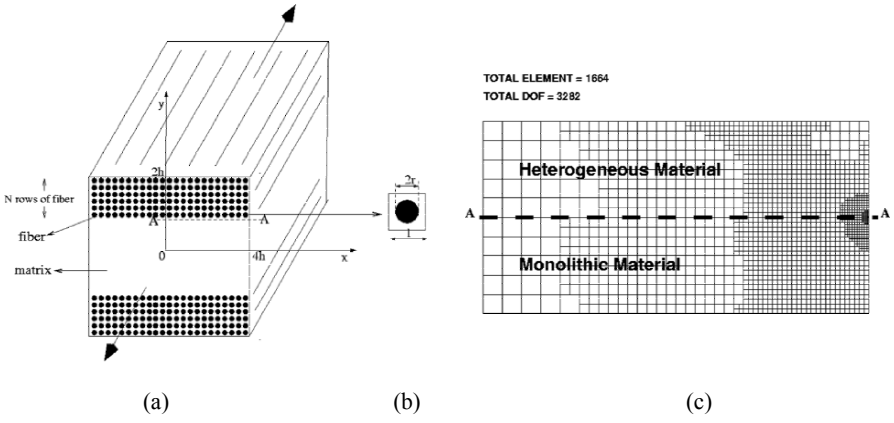


**Fig. 3.3.** (**a**) Unidirectional composite laminate subjected to out-of-plane loading; (**b**) a representative volume element of the microstructure, with a single fiber in a square matrix; (**c**) FE model with *h*-adapted mesh

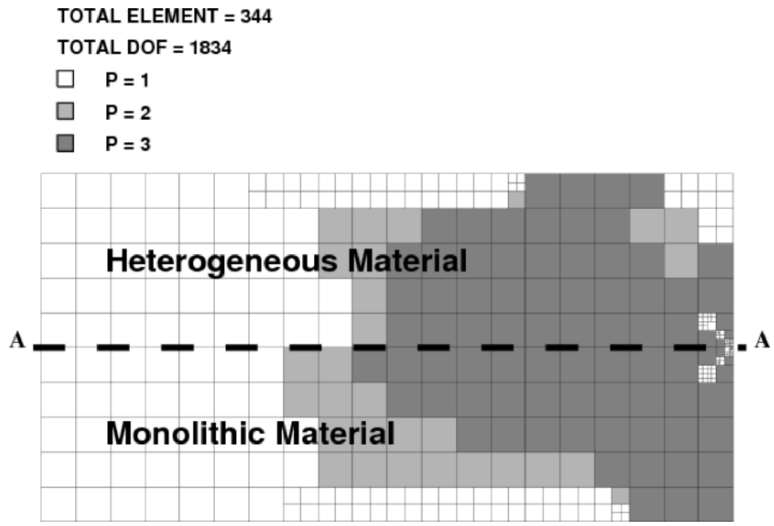


(a)

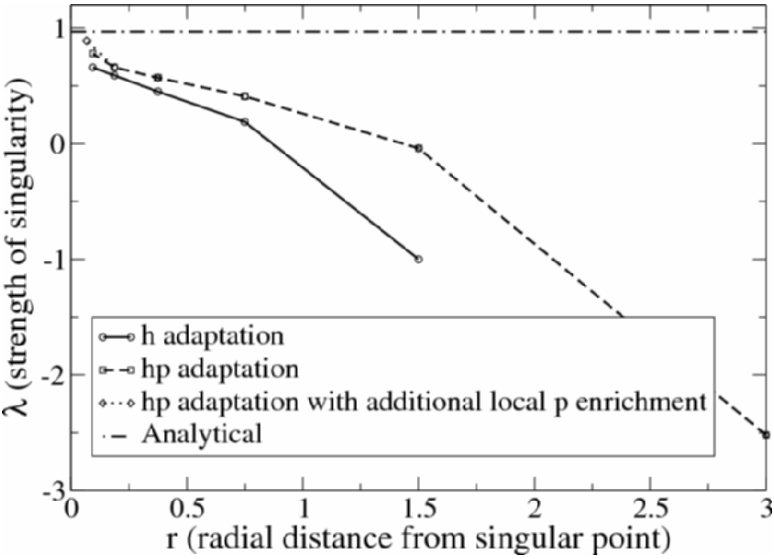


(b)

**Fig. 3.4.** (**a**) hp-adapted meshes in the regularized domain $\Omega^{l0}$, (**b**) convergence of the strength of singularity for the h- and hp-adapted meshes

The strength of the singularity $\lambda$ controls the rate of convergence and its value may be determined in the course of the adaptive refinements. The value of $\lambda$ is obtained by evaluating $\sigma_{yy}$ at two different values of $r$ close

to the singular point, and its convergence is shown in Fig. 3.4b. For the same smallest element size, the *h*-adapted mesh reaches up to a value of $\lambda = 0.66$, whereas the *hp*-adapted mesh goes up to $\lambda = 0.78$. Upon further enriching elements near the singular point by *p*-adaptation, $\lambda$ reaches 0.89.

### *Local and pollution errors in the regularized problem*

A posteriori error estimates based on elemental stresses or strain energy, e.g., jumps in variables, their gradients, or element residuals, are *local* in nature. Babuska [6] and Oden [54] have introduced element pollution error as one that is produced due to residual forces in other contiguous and noncontiguous elements in the mesh. Pollution error can be significant with uniform meshes in problems containing singularities, and local error estimation methods are incapable of detecting them. Consequently, in domains consisting of cracks, free edges, laminate interfaces, etc. accurate element error estimates in the energy norm may benefit from the addition of pollution errors to the local errors, i.e.,

$$\|\boldsymbol{er}\|^e = \|\boldsymbol{er}\|^e_{\text{local}} + \|\boldsymbol{er}\|^e_{\text{pollution}} \tag{3.20}$$

with equidistribution of error estimates in the mesh, the pollution error is negligible. However in problems where the singularity exponent $\lambda$ is less than half the order of interpolation *p*, i.e., $2\lambda < p$, the pollution error is significant. The basic algorithm develops an equivalent residual as the sum of element-wise local and pollution residuals as

$$\begin{aligned}
&B(\mathbf{er}_h, \mathbf{v}_h) = \sum_{k=1}^{N_E} [B(\mathbf{er}^{\text{local}}_{kh}, \mathbf{v}_h) + B(\mathbf{er}^{\text{poll}}_{kh}, \mathbf{v}_h)], \quad \text{where} \quad \sum_{k=1}^{N_E} B(\mathbf{er}^{\text{local}}_{kh}, \mathbf{v}_h) \\
&= \sum_{k=1}^{N_E} \int_{\Omega^k} [\mathbf{f} + \nabla \cdot (\mathbf{E} \nabla \mathbf{u}_{\text{H}})]_k \mathbf{v}_h \, \mathrm{d}\Omega + \int_{\partial\Omega^k} \hat{\mathbf{g}}_k \cdot \mathbf{v}_h \, \mathrm{d}\partial\Omega \quad \forall \mathbf{v}_h \in V^h \\
&\sum_{k=1}^{N_E} B(\mathbf{er}^{\text{poll}}_{kh}, \mathbf{v}_h) = \sum_{j=1, j\neq k}^{N_E} \int_{\Omega^j} [\mathbf{f} + \nabla(\mathbf{E} : \nabla \mathbf{u}_{\text{H}})]_j \mathbf{v}_h \, \mathrm{d}\Omega + \int_{\partial\Omega^j} \hat{\mathbf{g}}_j \mathbf{v}_h \, \mathrm{d}\partial\Omega \quad \forall \mathbf{v}_h \in V^h
\end{aligned} \tag{3.21}$$

$$\begin{aligned}
&\text{and} \quad \hat{\mathbf{g}}_k = \left[ \boldsymbol{\sigma}_k \cdot \mathbf{n}_k - \boldsymbol{\sigma}_{k'} \cdot \mathbf{n}_{k'} \right] \in \partial\Omega^k_{\text{hom}} \cap \partial\Omega^{k'}_{\text{hom}}, \\
&\qquad \hat{\mathbf{g}}_k = \mathrm{t} - \boldsymbol{\sigma}_{\mathrm{k}} \cdot \mathbf{n}_k \in \partial\Omega^k_{\text{hom}} \cap \Gamma_{t'}.
\end{aligned} \tag{3.22}$$

Here $\boldsymbol{V}^H$ is the polynomial subspace of $\boldsymbol{V}$, $\boldsymbol{V}^h$ is an enriched space approximation of $\boldsymbol{V}^H$. The major steps in the evaluation of the pollution error are given in [54, 62].

### *Composite laminate subjected to out-of-plane loading*

The problem of composite laminate with free edge, similar to the one in Sect. 3.2.1 is studied to understand the effect of local and pollution errors. The top half of the laminate is a composite with 28.2% volume fraction of boron fiber in epoxy matrix with effective orthotropic homogenized properties:

| $E_{11}$ (psi) | $E_{22}$ (psi) | $E_{33}$ (psi) | $G_{12}$ (psi) | $\nu_{12}$ | $\nu_{31}$ | $\nu_{23}$ |
|---|---|---|---|---|---|---|
| $0.99\times10^6$ | $0.99\times10^6$ | $17.2\times10^6$ | $0.27\times10^6$ | 0.43 | 0.29 | 0.29 |

The bottom half is monolithic epoxy material with properties $E_{\text{epoxy}} = 0.5\times10^6$ psi and $\nu_{\text{epoxy}} = 0.34$. Out-of-plane loading is simulated using generalized plane strain condition with prescribed $\varepsilon_{zz} = 0.1\%$. Due to symmetry in the *xz* and *yz* planes, only one quarter of the laminate is modeled. Symmetric boundary conditions are employed on the surfaces $x = 0$ and $y = 0$, and the top and right surfaces are assumed to be traction free.

For a uniform mesh, the local error is concentrated near the intersection of the interface and the free edge region, whereas the pollution error is more diffused and occurs in bands, starting at points slightly away from the intersection point around the free edge. When *h*-adaptation is applied, the maximum local error reduces from $6.285\times10^{-3}$ to $1.176\times10^{-4}$, while the pollution error reduces from $5.115\times10^{-4}$ to $3.105\times10^{-5}$. This is shown in Fig. 3.5. For this problem, the inclusion of pollution error in the total element error estimate is found to add little to the criteria for *h*- and *hp*-adaptation and only local error is considered henceforth.

### *Micromechanical analysis with the Voronoi cell FEM*

Accurate micromechanical modeling of deformation and damage in complex heterogeneous microstructures requires very high resolution models. Micromechanical analysis in the multilevel computational framework is conducted by the Voronoi cell finite element model (VCFEM) developed by Ghosh et al. in [26, 34, 46, 48–50] for accurate and efficient image-based modeling of nonuniform heterogeneous microstructures. Morphological arbitrariness in dispersion, shape, and size of heterogeneities, as acquired from actual micrographs are readily modeled by this method. The VCFEM computational mesh results from tessellating the microstructure

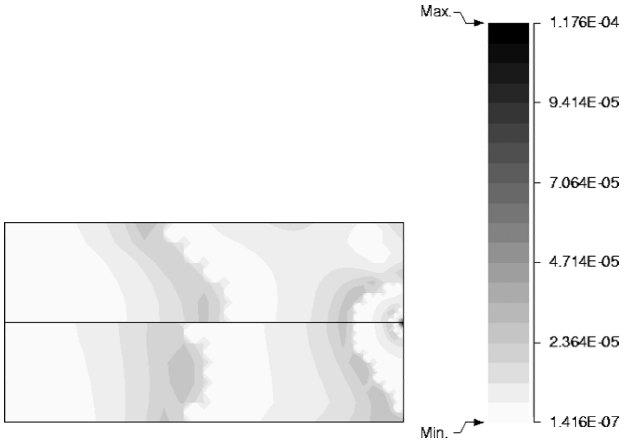


(a)

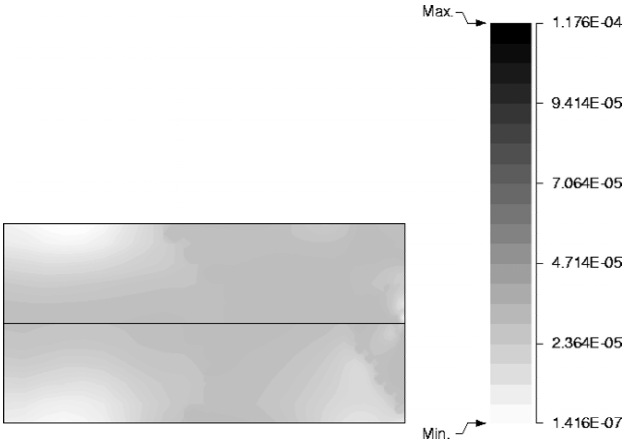


(b)

**Fig. 3.5.** Distribution of (**a**) local and (**b**) pollution error for the *h*-adapted mesh

$\Omega_{\text{micro}}^{\text{VCE}}$ with dispersed heterogeneities into a network of $N_{\text{VCE}}$ multisided Voronoi polygon or cell elements, i.e., $\Omega_{\text{micro}}^{\text{VCE}} = \bigcup_{e=1}^{N_{\text{VCE}}} \Omega_e^{\text{VCE}}$, as shown in Fig. 3.8. Each Voronoi cell with embedded heterogeneities (particle, fiber, void, crack, etc.) represents the region of contiguity for the heterogeneity and is treated as an element in VCFEM. In this sense, a Voronoi cell element manifests the basic structure of the material microstructure and its evolution and is considerably larger than conventional FEM elements. Incorporation of known functional forms from analytical micromechanics substantially enhances its convergence. The VCFEM formulation is based on the assumed stress hybrid finite element method, and makes independent assumptions of equilibrated stress fields $\left(\sigma_{ij}^{m/c}\right)$ in the interior of each

element $\Omega_{\text{micro}}^{\text{VCE}}$ for both the matrix and inclusion phases as well as compatible displacement fields $\left(u_i^e\right)$ on the element boundary $\partial\Omega_e^{\text{VCE}}$ and $\left(u_i^c\right)$ on the matrix–inclusion interface $\partial\Omega_c^{\text{VCE}}$. Considerable success has been achieved in modeling thermoelastic–plastic problems [48, 50], problems with microstructural damage by particle cracking [26, 49] and debonding [34, 45] by VCFEM. Recent extensions of VCFEM include multiple crack simulations by an extended VCFEM or X-VCFEM [46] and 3D VCFEM model in [27].

VCFEM is based on a hybrid formulation with independent assumptions on equilibrated stress fields $\sigma_{ij}$ defined in the matrix phase $\Omega_m^{\text{VCE}}$ and the inclusion phase $\Omega_c^{\text{VCE}}$ of each Voronoi cell element. Special forms of stress functions are developed for equilibrated stress fields from known analytical micromechanics solutions. The stress functions are comprised of polynomials, shape-based reciprocal functions, and wavelet functions to facilitate accurate stress concentrations near the interface or crack tips. Compatible displacements are generated on the boundaries $\partial\Omega_e^{\text{VCE}}$ and interfaces $\partial\Omega_c^{\text{VCE}}$ (shown in Fig. 3.13b) by interpolating nodal displacements using polynomial shape functions. The stress and displacement interpolations may be expressed in matrix equation forms as

$$\begin{aligned}
&\left\{\boldsymbol{\sigma}^m\right\}=\left[\mathbf{P}^m\left(x,y\right)\right]\left\{\boldsymbol{\beta}^m\right\}\subset\Omega_m^{\text{VCE}} \text{ and } \left\{\boldsymbol{\sigma}^c\right\}=\left[\mathbf{P}^c\left(x,y\right)\right]\left\{\boldsymbol{\beta}^c\right\}\subset\Omega_c^{\text{VCE}},\\
&\left\{\mathbf{u}^e\right\}=\left[\mathbf{L}^e\right]\left\{\mathbf{q}^e\right\} \text{ on } \partial\Omega_e^{\text{VCE}} \text{ and } \left\{\mathbf{u}^c\right\}=\left[\mathbf{L}^c\right]\left\{\mathbf{q}^c\right\} \text{ on } \partial\Omega_c^{\text{VCE}},
\end{aligned} \tag{3.23}$$

where $\left\{\boldsymbol{\beta}\right\}, \left\{\boldsymbol{\beta}\right\}, \left[\mathbf{P}\left(x,y\right)\right]$ and $\left[\mathbf{P}\left(x,y\right)\right]$ are the stress coefficients and interpolating functions, and $\left\{\mathbf{q}^e\right\}, \left\{\mathbf{q}^c\right\}, \left[\mathbf{L}^e\right]$ and $\left[\mathbf{L}^c\right]$ are the nodal displacement vectors and the corresponding interpolation matrices, respectively. A complementary energy functional for a Voronoi cell element may be defined as

$$\begin{aligned}
&\Pi_e^{\text{VCE}}(\boldsymbol{\sigma}^m,\boldsymbol{\sigma}^c,\mathbf{u}^e,\mathbf{u}^c)=\int_{\Omega_m^{\text{VCE}}}\frac{1}{2}\boldsymbol{\sigma}^m:\mathbf{S}^m:\boldsymbol{\sigma}^m\,\mathrm{d}\Omega+\int_{\Omega_c^{\text{VCE}}}\frac{1}{2}\boldsymbol{\sigma}^c:\mathbf{S}^c:\boldsymbol{\sigma}^c\,\mathrm{d}\Omega\\
&-\int_{\partial\Omega_e^{\text{VCE}}}\boldsymbol{\sigma}^m\cdot\mathbf{n}^e\cdot\mathbf{u}^e\,\mathrm{d}\partial\Omega+\int_{\Gamma_t^{\text{VCE}}}\overline{\mathbf{t}}\cdot\mathbf{u}^e\,\mathrm{d}\Gamma+\int_{\partial\Omega_c^{\text{VCE}}}(\boldsymbol{\sigma}^m-\boldsymbol{\sigma}^c)\cdot\mathbf{n}^c\cdot\mathbf{u}^c\,\mathrm{d}\partial\Omega\\
&\forall\Omega_e^{\text{VCE}}=\Omega_m^{\text{VCE}}\bigcup\Omega_c^{\text{VCE}},
\end{aligned} \tag{3.24}$$

where $\mathbf{S}^m$ and $\mathbf{S}^c$ are the elastic compliance tensors in the matrix phase $\Omega_m^{\mathrm{VCE}}$ and inclusion phase $\Omega_c^{\mathrm{VCE}}$ of each element, $\mathbf{n}^e$ and $\mathbf{n}^c$ are the outward normals on $\partial\Omega_e^{\mathrm{VCE}}$ and interfaces $\partial\Omega_c^{\mathrm{VCE}}$, respectively, and $\bar{\mathbf{t}}$ is the prescribed traction on the boundary $\Gamma_{tm}^{\mathrm{VCE}}$. The corresponding total energy functional for the ensemble of all Voronoi cell elements in the domain is

$$\Pi_{\mathrm{Total}}^{\mathrm{VCE}} = \sum_{e=1}^{N_{\mathrm{VCE}}} \Pi_e^{\mathrm{VCE}} = \sum_{e=1}^{N_{\mathrm{VCE}}} \int_{\Omega_e^{\mathrm{VCE}}} \frac{1}{2}\boldsymbol{\sigma} : \mathbf{S} : \boldsymbol{\sigma}\, \mathrm{d}\Omega - \sum_{e=1}^{N_{\mathrm{VCE}}} \int_{\partial\Omega_e^{\mathrm{VCE}}} \boldsymbol{\sigma}\cdot\mathbf{n}^e \cdot \mathbf{u}^e\, \mathrm{d}\partial\Omega$$
$$+ \sum_{e=1}^{N_\Gamma} \int_{\Gamma_t^{\mathrm{VCE}}} \bar{\mathbf{t}}\cdot\mathbf{u}^e\, \mathrm{d}\Gamma + \sum_{e=1}^{N_{\mathrm{VCE}}} \int_{\partial\Omega_c^{\mathrm{VCE}}} (\boldsymbol{\sigma}^m - \boldsymbol{\sigma}^c)\cdot\mathbf{n}^c\cdot\mathbf{u}^c\, \mathrm{d}\partial\Omega. \tag{3.25}$$

Setting the first variations of $\Pi^{\mathrm{VCE}}$ with respect to the element stresses $\boldsymbol{\sigma}^m, \boldsymbol{\sigma}^c$, and also the first variations of $\Pi_{\mathrm{Total}}^{\mathrm{VCE}}$ with respect to the displacements $\mathbf{u}^e$ and $\mathbf{u}^c$ to zero results in the following equations, respectively,

$$\begin{aligned}
&\int_{\Omega_{\mathrm{in}}^{\mathrm{VCE}}} \boldsymbol{\sigma}^m : \mathbf{S}^m : \delta\boldsymbol{\sigma}^m\, \mathrm{d}\Omega - \int_{\partial\Omega_e^{\mathrm{VCE}}} \delta\boldsymbol{\sigma}^m\cdot\mathbf{n}^e\cdot\mathbf{u}^e \mathrm{d}\partial\Omega + \int_{\partial\Omega_c^{\mathrm{VCE}}} \delta\boldsymbol{\sigma}^m\cdot\mathbf{n}^c\cdot\mathbf{u}^c \mathrm{d}\partial\Omega = 0 \quad \text{(a)}\\
&\int_{\Omega_{\mathrm{in}}^{\mathrm{VCE}}} \boldsymbol{\sigma}^c : \mathbf{S}^c : \delta\boldsymbol{\sigma}^c\, \mathrm{d}\Omega - \int_{\partial\Omega_c^{\mathrm{VCE}}} \delta\boldsymbol{\sigma}^c\cdot\mathbf{n}^c\cdot\mathbf{u}^c\, \mathrm{d}\partial\Omega = 0 \quad \text{(b)}\\
&-\sum_{e=1}^{N_{\mathrm{VCE}}} \int_{\partial\Omega_e^{\mathrm{VCE}}} \boldsymbol{\sigma}^m\cdot\mathbf{n}^e\cdot\delta\mathbf{u}^e\, \mathrm{d}\partial\Omega + \sum_{e=1}^{N_{\mathrm{VCE}}} \int_{\Gamma_t^{\mathrm{VCE}}} \bar{\mathbf{t}}\cdot\delta\mathbf{u}^e\, \mathrm{d}\Gamma = 0 \quad \text{(c)}\\
&\sum_{e=1}^{N_{\mathrm{VCE}}} \int_{\partial\Omega_c^{\mathrm{VCE}}} (\boldsymbol{\sigma}^m - \boldsymbol{\sigma}^c)\cdot\mathbf{n}^c\cdot\delta\mathbf{u}^c\, \mathrm{d}\partial\Omega = 0 \quad \text{(d)}
\end{aligned} \tag{3.26}$$

Equations (3.26a) and (3.26b) correspond to weak forms of the kinematic relations in the matrix and inclusion domains of each element, respectively. Solving these equations yields the relations between domain stresses and the boundary/interface displacements. Equations (3.26c) and (3.26d) correspond to weak forms of the traction reciprocity condition at the element boundary and the matrix–inclusion interface, respectively. The boundary and interface displacements can be determined by substituting the stress–displacement relations from (3.26a) and (3.26b), into (3.26c) and (3.26d) and solving them. The reader is referred to [26, 34, 46, 48–50] for details on VCFEM.

An adaptive VCFEM is developed in [50] to enhance solution accuracy and convergence of micromechanical solutions. Two error indicators are introduced to facilitate this adaptation:

1. *Traction reciprocity error on element boundaries and internal interfaces.* To estimate the quality of solution induced by the weak satisfaction of traction continuity on the Voronoi cell element boundary, an average traction continuity error (ATRE) is defined as

$$\text{ATRE}=\frac{\sum_{\hat{e}=1}^{\hat{N}_e} er_T^{\hat{e}}+\sum_{\hat{e}=1}^{\hat{N}_e} er_T^{\hat{c}}}{\hat{N}_e+\hat{N}_c},\ \text{where}\ \ er_T^{\hat{e}}=\frac{1}{\bar{\sigma}}\left[\frac{\int_{\partial Y_e^{\hat{e}}}\left([[\mathbf{t}]]\cdot[[\mathbf{t}]]\right)^{1/2}\mathrm{d}\partial Y}{n^*\int_{\partial Y_e^{\hat{e}}}\mathrm{d}\partial Y}\right]$$

$$\text{and}\quad er_T^{\hat{c}}=\frac{1}{\bar{\sigma}}\left[\frac{\int_{\partial Y_e^{\hat{c}}}\left([[\mathbf{t}]]\cdot[[\mathbf{t}]]\right)^{1/2}\mathrm{d}\partial Y}{n^*\int_{\partial Y_e^{\hat{c}}}\mathrm{d}\partial Y}\right]. \tag{3.27}$$

Equations (3.27), $\hat{N}_e$ and $\hat{N}_c$ are the total of all segments $\partial Y_e^{\hat{e}}$ and $\partial Y_e^{\hat{c}}$ on all element boundaries $\partial\Omega_e^{\text{VCE}}$ and interfaces $\partial\Omega_c^{\text{VCE}}$, respectively. The stress $\bar{\sigma}$ in the denominator is the absolute maximum principal value of the volume-averaged stress tensor in the microstructure, i.e.,

$$\bar{\sigma}_{ij}=\frac{\int_{\partial\Omega}\sigma_{ij}\,\mathrm{d}\partial\Omega}{\int_{\partial\Omega}\mathrm{d}\partial\Omega},$$

$n^*$ is the number of degrees of freedom per node and $[[\mathbf{t}]]$ is the traction discontinuity along element boundaries and interfaces.

2. *Error in kinematic relations in the element matrix and reinforcement phases.* The source of this error is the weak satisfaction of kinematic or compatibility relations in the matrix and inclusion phases of each Voronoi cell element. To quantify this effect, an average strain energy error indicator (ASEE) related to the kinematic relation is defined in [50] as

$$\text{ASEE}=\frac{\sqrt{\sum_{e=1}^{\text{N}} er_{\text{SE}}^2}}{\text{N}},\quad \text{where}\quad er_{\text{SE}}^2=\frac{1}{SE^2}\Bigg[\int_{\Omega_m^{\text{VCE}}}{}^*\boldsymbol{\sigma}^m:{}^*\boldsymbol{\varepsilon}^m\,\mathrm{d}\Omega$$

$$+\int_{\Omega^{\text{VCE}}}{}^*\boldsymbol{\sigma}^c:{}^*\boldsymbol{\varepsilon}^c\,\mathrm{d}\Omega-\int_{\partial\Omega_e^{\text{VCE}}}{}^*\boldsymbol{\sigma}^m\cdot\mathbf{n}^e\cdot{}^*\mathbf{u}^e\,\mathrm{d}\partial\Omega+\int_{\partial\Omega_c^{\text{VCE}}}{}^*\boldsymbol{\sigma}^m\cdot\mathbf{n}^c\cdot{}^*\mathbf{u}^c\,\mathrm{d}\partial\Omega$$

$$-\int_{\partial\Omega_c^{\text{VCE}}}{}^*\boldsymbol{\sigma}^c\cdot\mathbf{n}^c\cdot{}^*\mathbf{u}^c\,\mathrm{d}\partial\Omega\Bigg]. \tag{3.28}$$

The variables with superscripts *, i.e., ${}^*\boldsymbol{\sigma}^m$, ${}^*\boldsymbol{\varepsilon}^m$, ${}^*\mathbf{u}^e$, and ${}^*\mathbf{u}^c$ correspond to the change in element stress, strain, and displacement fields that result

from enrichments in the stress interpolations $\boldsymbol{\sigma}^m$ and $\boldsymbol{\sigma}^c$. SE in ASEE is the strain energy of the entire micromechanical domain that is expressed as

$$\mathrm{SE}^2 = \sum_{e=1}^{N} \frac{1}{2} \int_{\Omega_m^{\mathrm{VCE}}} \boldsymbol{\sigma}^m : \boldsymbol{\varepsilon}^m \, \mathrm{d}\Omega + \sum_{e=1}^{N} \frac{1}{2} \int_{\Omega_c^{\mathrm{VCE}}} \boldsymbol{\sigma}^c : \boldsymbol{\varepsilon}^c \, \mathrm{d}\Omega. \tag{3.29}$$

$er_{\mathrm{SE}}$ is the element level error estimator in strain energy. The latter estimator is a measure of the change in strain energy due to stress enrichment and, hence, is positive for positive definite stiffness matrices. Adaptation for enhancing the rate of convergence of VCFEM solutions is executed in two stages. In the first stage, the traction continuity error in (3.27) is minimized by selectively enhancing boundary and interface displacement degrees of freedom in the directions of optimal displacement enrichments. In the second stage, stress function enrichment with higher order polynomial terms ($^{enr}p$-adaptation) of each element is performed for reducing the strain energy error [32].

The effectiveness of the adaptive Voronoi cell finite element model is tested by comparison with a well-known problem in micromechanics solved in [58, 67]. The boundary value problem, schematically illustrated in Fig. 3.8, demonstrates the limitations of the effective modulus theory in predicting stress states in laminated composites near a free edge. The composite has two rows of reinforcement, each consisting of eight aligned cylindrical boron fibers aligned in the *z*-direction, perpendicular to the plane of the paper. The fiber radius to edge dimension ratio is $r/l = 0.3$. Only a quarter of the cross section is analyzed due to symmetry about the *xy* and *xz* planes. The resulting mesh consists of four Voronoi cell elements as shown in Fig. 3.6a. The microstructure is subjected to a constant out-of-plane axial strain $\varepsilon_{zz} = 1$, which is modeled using generalized plane strain conditions. The material properties are given below:

| Material | Young's modulus, $E$ (psi) | Poisson ratio |
|---|---|---|
| Boron (fiber) | $E_{\mathrm{bo}} = 60 \times 10^6$ | $\nu_{\mathrm{bo}} = 0.2$ |
| Epoxy (matrix) | $E_{\mathrm{epoxy}} = 0.5 \times 10^6$ | $\nu_{\mathrm{epoxy}} = 0.34$ |

The analysis considers two boundary conditions:

(a) Edges $x = 0$ and $y = 0$ are symmetry surfaces, while $x = 4h$ and $y = 2h$ are traction free

(b) Edges $x = 0$ and $y = 2h$ are symmetry surfaces and $x = 4h$ and $y = 0$ are traction free

The matrix stresses are constructed from an Airy's stress function consisting of a fourth-order polynomial and a 36 term reciprocal function.

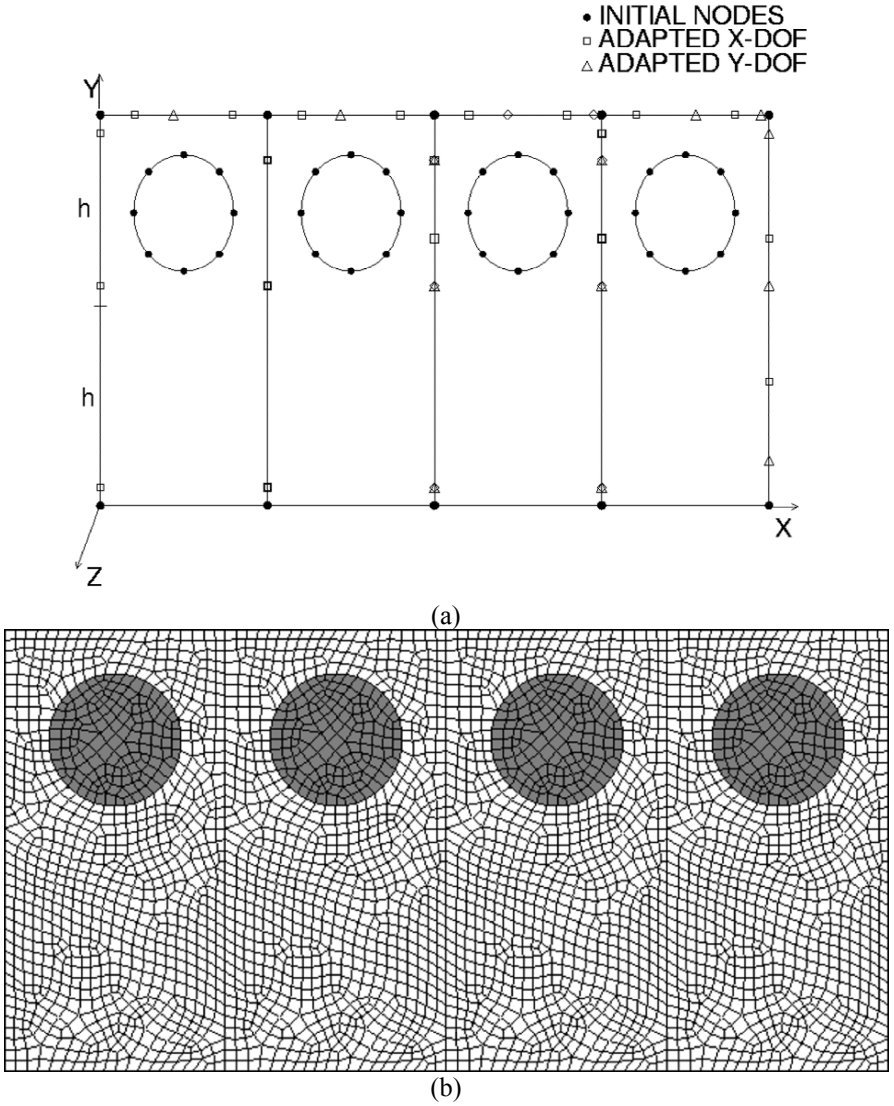


**Fig. 3.6.** (**a**) A microstructural hp-adapted VCFEM mesh showing locations of the initial and added nodes with $x$- and $y$-DOF – case (**a**); (**b**) ANSYS mesh

The inclusion stresses are constructed using a sixth-order polynomial function. Displacement fields are constructed with linear shape functions for element boundaries and quadratic shape functions for curved interface elements. The results of the adaptation cycle for the problem in case (a) are illustrated in Fig. 3.6 in terms of added displacement degrees of freedom. The preadaptation nodes are marked with a "filled circle." The *x*-direction nodal adaptations are marked with an "open square" while those in the *y*-direction are shown with "open triangle." The VCFEM solutions for both cases are compared with numerical results of micromechanical analysis provided in [67] and also with those from analysis by the finite element code ANSYS. The converged ANSYS mesh with 4230 QUAD4 elements and 4352 nodes is shown in Fig. 3.6b.

The transverse microscopic stress $\sigma_{yy}$, which is approximately two orders lower compared with the leading order stress $\sigma_{zz}$, is plotted along the horizontal section at $y = h$ in Fig. 3.7. Results are compared for the unadapted VCFEM, *hp*-adapted VCFEM, and the ANSYS model. The adapted VCFEM results agree very well with the ANSYS model. The figure also shows the singular stress solution near the free edge, which is obtained as a consequence of using the effective modulus theory by homogenization.

### *Statistically equivalent RVEs for nonuniform microstructures*

Identification of the appropriate representative volume element or RVE is essential for estimating homogenized material properties needed in the computations of *level-0* or *level-1* elements. An RVE is not easily identifiable for material microstructures with nonuniform morphological distributions as shown in Fig. 3.8a. It is possible to identify an RVE only in a statistical sense, otherwise called a statistically equivalent RVE or SERVE. The SERVE is expected to exhibit a macroscopic behavior that is equivalent to the average behavior of the entire microstructural ensemble. A variety of statistical and computational tools are developed for identifying the SERVE for elastic composites with nonuniform dispersion of inclusions in [72]. The evolution of the SERVE with microstructural damage by interfacial debonding is examined in [73] using various metrics. As an example, the marked correlation function introduced in [60] is used in this chapter to delineate the SERVE size. This function characterizes the region of influence of a chosen heterogeneity on others in a domain with respect to chosen variables like stresses, strains, etc. The marked correlation function for a domain of an area $A$ containing $N$ inclusions is expressed as

$$M(r)=\frac{\mathrm{d}\dfrac{H(r)}{\mathrm{d}r}}{g(r)}, \quad \text{where} \quad H(r)=\frac{1}{m^2}\frac{A}{N^2}\sum_{i}^{N}\sum_{k=1}^{k_i} m_i m_k(r). \tag{3.30}$$

In (3.30), $m_i$ is a mark associated with the $i$th inclusion, $k_i$ is the number of inclusions which have their centers within a circle of radius $r$ around the $i$th inclusion, and $m$ is the mean of all the marks. Marks can be any field variable like the maximum principal stress or Von Mises stress or even a geometric feature associated with each inclusion. $H(r)$ is called the mark intensity function and $g(r)$ is the pair distribution function defined as

$$g(r)=\frac{1}{2\pi r}\frac{\mathrm{d}K(r)}{\mathrm{d}r}, \tag{3.31}$$

where $K(r)$ is a second-order intensity function explained in [32, 33, 72]. The radius of influence $R_{\text{inf}}$ can be determined from a plot of $M(r)$ vs. $r$. $R_{\text{inf}}$ corresponds to the value of $r$ at which $M(r)$ stabilizes to a constant value. Upon determining $R_{\text{inf}}$, the SERVE may be constructed from the inclusions contained in a $R_{\text{inf}} \times R_{\text{inf}}$ square window of the micrograph. As shown in Fig. 3.8b, the local microstructure is first constructed by periodically repeating the set of inclusions that lie (wholly or partially) in the window in both the $y_1$ and $y_2$ directions for several period lengths. For each fiber at $(y_1,y_2)$, periodically repetitive inclusions are placed at $\left(y_1 \pm k_1 Y_1, y_2\right)$, $\left(y_1, y_2 \pm k_2 Y_2\right)$, and $\left(y_1 \pm k_1 Y_1, y_2 \pm k_2 Y_2\right)$, where $k_1, k_2$ are integers. The resulting domain is then tessellated into a network of Voronoi cells as shown in Fig. 3.8b. The SERVE boundary, shown with bold lines in Fig. 3.8b, is the aggregate of all outside edges of Voronoi cells that are associated with the primary inclusions in the domain (shown in black). For nonuniform inclusion arrangements, the SERVE boundary will consist of multiple nonaligned edges. Nodes on the SERVE boundary created by this procedure are periodic. For every boundary node, a periodic pair, e.g., AA, BB, etc., can be identified on the boundary at a distance of one period along one or both of the coordinate directions. Periodicity constraint conditions on nodal displacements can then be easily imposed.

A numerical example is considered to demonstrate the effect of the SERVE size on macroscopic properties as well as on microscopic stresses. Maximum principal stress in the fiber and maximum Von Mises stress in matrix in each Voronoi cell are considered as *marks* in the correlation function, since they are good indicators of microstructural failure initiation.

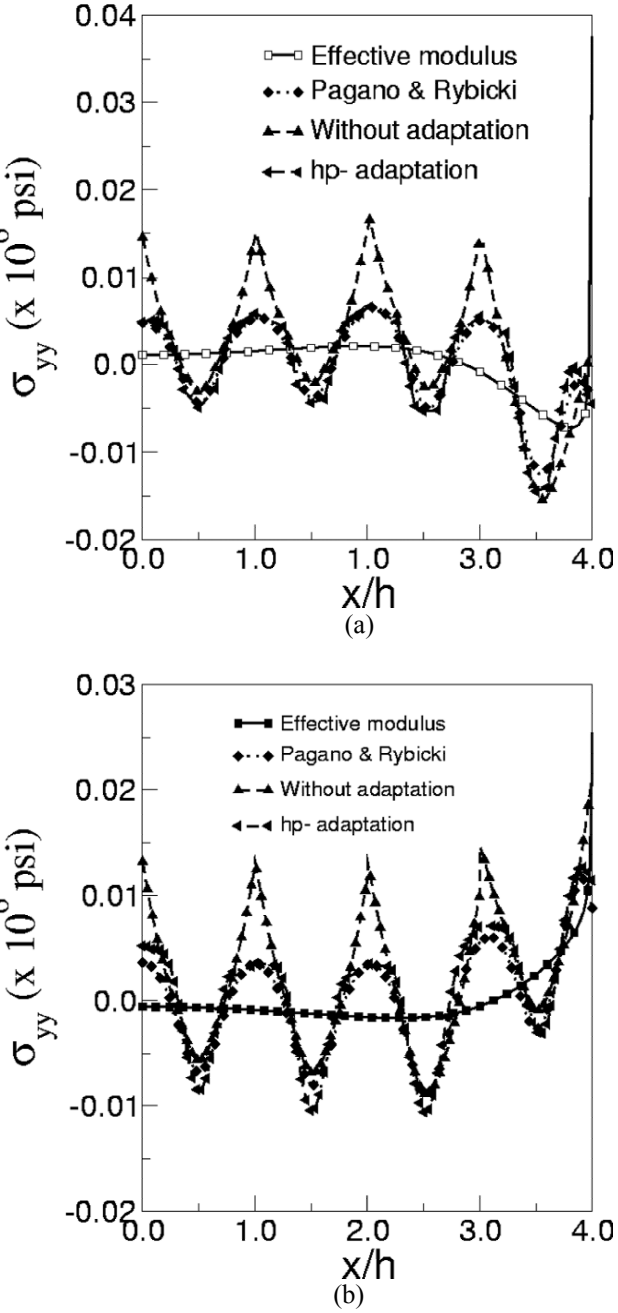


**Fig. 3.7.** $\sigma_{yy}$ distribution at section A–A ($y = h$) for the composite section with one row of fiber for (**a**) case-a and (**b**) case-b

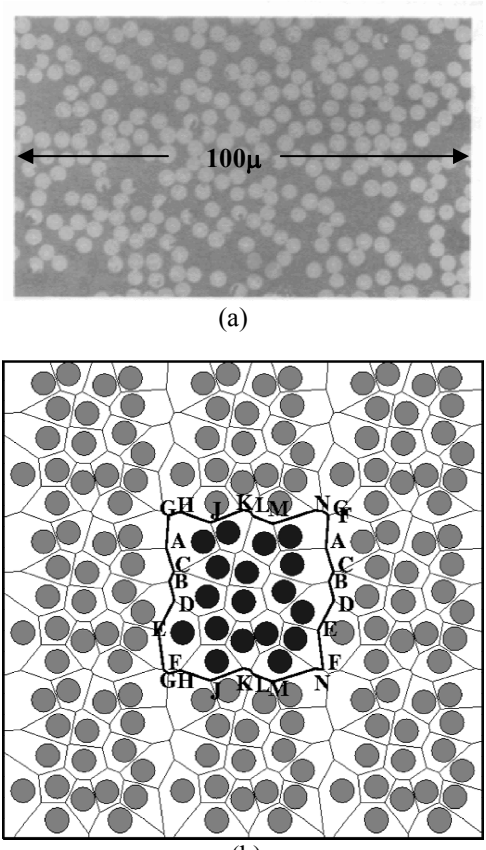


**Fig. 3.8.** (**a**) Optical micrograph of a polymer–matrix composite microstructure; (**b**) an RVE evolving from tessellation of microstructure with nonstraight edges

Plots of $M(r)$ for different marks are shown in Fig. 3.9a. The distance $r$ is normalized with respect to the fiber radius $r_0 = 1.75\,\mu\text{m}$. $M(r)$ is high at distances less than $8r_0$ but stabilizes to a unit value at distances approximately greater than $8r_0$, corresponding to the region of influence of stress. It can also be seen that $M(r)$ plots for both Von Mises stress and principal stress are similar and stabilize approximately in the same radial range $r$. A similar behavior of $M(r)$ is also observed when the micrograph is loaded under biaxial tension as shown in Fig. 3.9b and, hence, $8r_0$ characterizes the size scale of the SERVE.

Convergence of macroscopic moduli and maximum microscopic stress with RVE size are studied for five different RVEs, consisting of 1, 8, 18, 35, and 55 fibers as shown in Fig. 3.10. The corresponding SERVE sizes

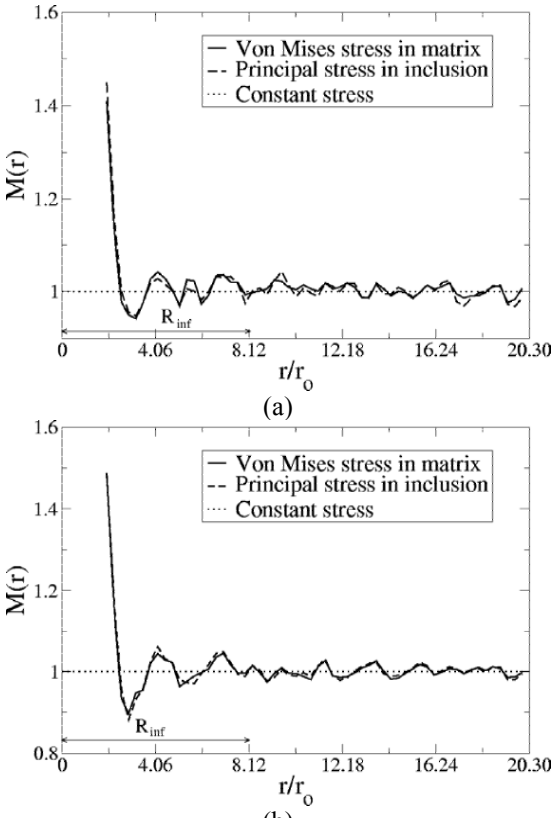


**Fig. 3.9.** Marked correlation functions $M(r)$ for (**a**) uniaxial and (**b**) biaxial load

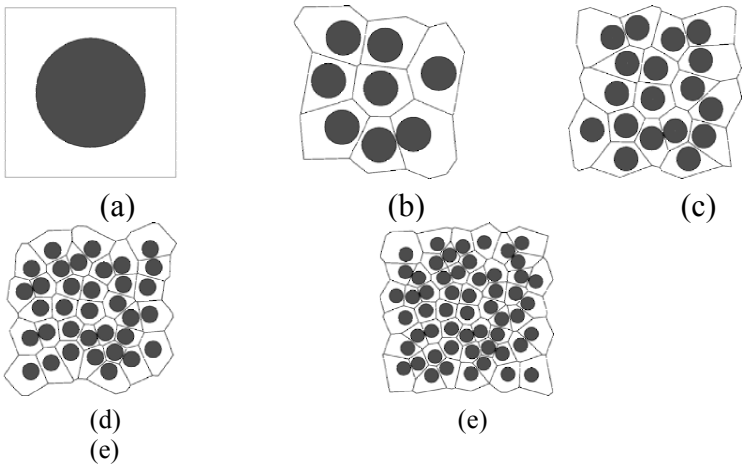


**Fig. 3.10.** SERVEs with 1, 8, 18, 35, and 55 fibers

are $r_0, 3r_0, 6r_0, 9r_0$, and $12r_0$, respectively. The morphology of each RVE is chosen from any arbitrary region in the micrograph. The Frobenius norm of the effective elastic modulus $\|E\|$ is plotted as a function of increasing RVE sizes at two different locations in the microstructure in Fig. 3.11a. The difference in the norm between the single fiber and 55 fibers is around $2\%$, while the difference between 18 fibers and 55 fibers is found to be less than 0.5%. A similar observation is also made when comparing the microscopic maximum Von Mises stress in the matrix and maximum principal stress in the fiber as functions of increasing RVE size in Fig. 3.11b.

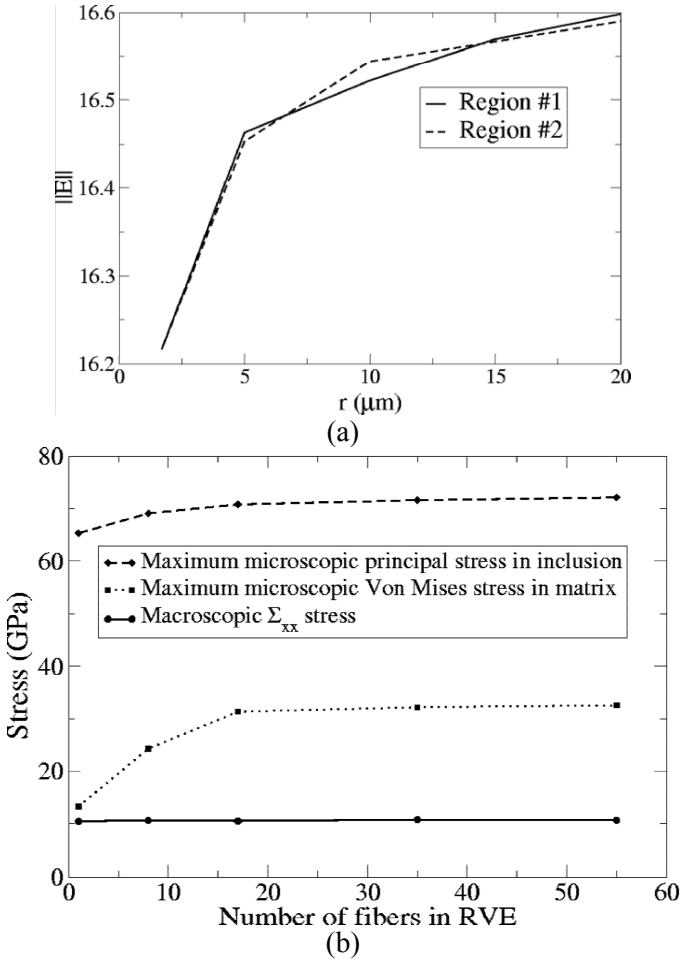


**Fig. 3.11.** Convergence of the (**a**) macroscopic stiffness and (**b**) microscopic stresses with increasing RVE sizes

The difference in maximum Von Mises stress in the matrix for the single fiber RVE and 55 fiber RVE is almost 60%, whereas the corresponding difference for the 18 fiber RVE and the 55 fiber RVE is less than 4%. Hence, a SERVE consisting of 18 fibers is deemed adequate for homogenization.

#### *Computational subdomain level-1* $\Omega^{l1}$

The *level-1* subdomains facilitate switchover from homogenization-based analysis in *level-0* subdomains to micromechanical analysis in *level-2* subdomains. They are seeded in regions of locally high gradients of macroscopic variables in *level-0* simulations. The formulation for $\Omega^{l1}$ is the same as for $\Omega_{\text{hom}}$ in Sect. 3.3.1. It serves as a "swing" region, where microscopic variables in the SERVE, as well as macroscopic gradients, are used to decide whether homogenization is valid in this region. Major steps in *level-1* element computations are:

1. Evaluate homogenized elastic stiffness $C^H_{ijkl}$ for the macroscopic analysis using (3.10) with applied macroscopic unit strains corresponding to (3.15) together with periodicity.
2. Evaluate element stiffness and load vectors for elements $E_{l0}$ and $E_{l1}$ using $C^H_{ijkl}$, and solve the global FE equations for macroscopic displacements, stresses, and strains.
3. Perform RVE analysis in the postprocessing stage with macroscopic strains $e_{ij} = (1/2)((\partial u^0_i / \partial x_j) + (\partial u^0_j / \partial x_i))$ imposed from Step 2 and periodic boundary conditions. Microscopic stresses, strains, and other variables are computed in the RVE of every element $\left(E_{l1} \in \Omega^{l1}\right)$ for developing appropriate level switching criteria.

Macroscopic elements in $\Omega^{l1}\left(E_{l1}\right)$ are also adaptively enriched by *h*- and *hp*-refinement. No special treatment is required for displacement compatibility between $E_{l0}$ and $E_{l1}$ elements, since their boundaries are similar with identical displacement interpolation.

#### *Criteria for level-0 to level-1 transition*

Elements in the computational subdomain $\Omega^{l1}\left(E_{l1} \in \Omega^{l1}\right)$ are computationally much more expensive than *level-0* elements $E_{l0}$. Hence, the selection of appropriate criteria for switching from $E_{l0}$ to $E_{l1}$ elements is

critical to enhance efficiency by optimally limiting the number of $E_{l1}$ elements. These criteria depend on the important variables for the problem in question. Various switching criteria, based on gradients of physically significant stress measures, have been tested in [29, 36, 61]. As an example, element *k* will be required to undergo a *level* $0 \to 1$ transition if

$$E_k \left( \frac{\left(\Sigma_{\text{eqv}}\right)_k}{\left(\Sigma_{\text{eqv}}\right)_{\max}} \right) \geq C_1 E_{\text{avg}}, \quad \text{where} \quad E_{\text{avg}} = \left( \frac{\sum_{i=1}^{N_E} E_i^2}{NE} \right)^{1/2}. \tag{3.32}$$

Here $C_1$ is a prescribed tolerance, $\Sigma_{\text{eqv}}$ is the equivalent stress in element *k*, and $E_k$ can have one of the following forms:

$$\begin{aligned}
&\text{(a)} \quad E_k^2 = \frac{\int_{\partial\Omega_{\text{hom}}^k} [[\Sigma_{ij}]]^2 \, \mathrm{d}\partial\Omega}{\int_{\partial\Omega_{\text{hom}}^k} \mathrm{d}\partial\Omega}, \\
&\text{(b)} \quad E_k^2 = \frac{\int_{\partial\Omega_{\text{hom}}^k} [[\Sigma_{\text{pr}}]]^2 \, \mathrm{d}\partial\Omega}{\int_{\partial\Omega_{\text{hom}}^k} \mathrm{d}\partial\Omega}, \\
&\text{(c)} \quad E_k^2 = \frac{\int_{\partial\Omega_{\text{hom}}^k} \left( [[T_x]]^2 + [[T_y]]^2 \right) \mathrm{d}\partial\Omega}{\int_{\partial\Omega_{\text{hom}}^k} \mathrm{d}\partial\Omega}.
\end{aligned} \tag{3.33}$$

$\Sigma_{ij}$ is a chosen macroscopic stress component, $\Sigma_{\text{pr}}$ is the dominant principal stress, $T_x, T_y$ are the element boundary traction components and $[[\cdots]]$ denotes the jump operator. The criterion in (3.32) reflects the fact that high gradients in regions of high stress levels are more relevant than those at low stress levels.

### *Computational subdomain level-2* $\Omega^{l2}$

*Level-2* subdomains of detailed microscopic analysis are characterized by the nonsatisfaction of homogenization conditions used in the *level-0* and *level-1* subdomains. Microstructural nonuniformities in the form of strongly nonperiodic, e.g., clustered dispersions or concentrated high stresses and strains with high gradients, occurring near a crack tip or free edge, necessitate the emergence of $\Omega^{l2}$. Appropriate adaptation criteria are

used to trigger switching from $E_{l1}\left(\in \Omega^{l1}\right)$ to $E_{l2}\left(\in \Omega^{l2}\right)$ elements for micromechanical analysis. It is expected that the local *h*- or *hp*-refinement in *level-0* or *level-1* elements will have reduced the size of these elements sufficiently prior to transition to the *level-2* elements such that a high spatial resolution is locally attained.

The elements $E_{l2}$ are constructed by filling the *level-0/1* elements with the exact microstructure at that location. The region $\Omega_{l2}^{k}$ encompassed in the *k*th *level-2* element $E_{l2}^{k}$ is obtained as the intersection of the local microstructural region $\Omega^{\varepsilon}$ with the *k*th *level-1* element $\Omega_{l1}^{k}$, i.e., $\Omega_{l2}^{k} = \Omega^{\varepsilon} \bigcap \Omega_{l1}^{k}$. The steps in creating a *level-2* element are as follows:

- Identify a region $\Omega_{\hat{k}} \in \Omega_{\text{het}}$ that is located in the same region as $\Omega_{l2}^{k}$ and extends beyond it by at least two fiber lengths.
- Tessellate $\Omega_{\hat{k}}$ to generate a mesh of Voronoi cell elements as shown in Fig. 3.12a.
- Carve out the region $\Omega_{l2}^{k}$ by superposing the boundary of $\Omega_{l1}^{k}$ on $\Omega_{\hat{k}}$. This procedure will result in dissecting some of the fibers on the boundary of $\Omega_{l2}^{k}$. When this happens, additional nodes are generated on the Voronoi cell boundary at locations where the fiber surface and Voronoi cell edges intersect the boundary of $\Omega_{l2}^{k}$.

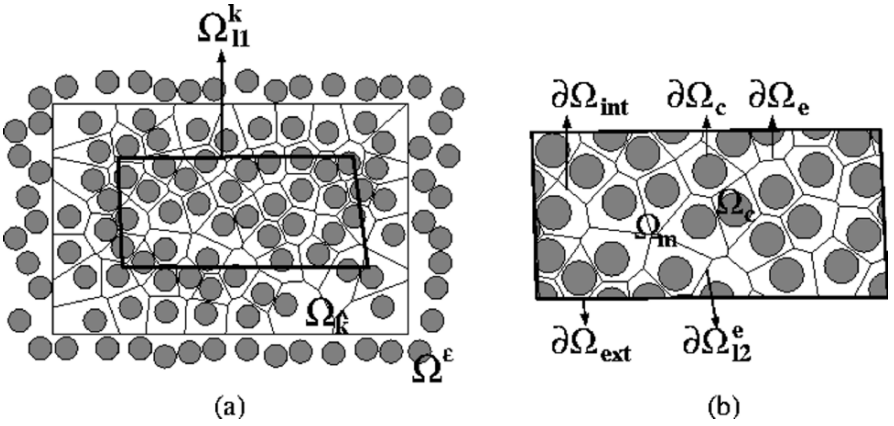


**Fig. 3.12.** (**a**) Carving out extended microstructural region in level-2 element; (**b**) level-2 element consisting of VC finite elements for microstructural modeling

Accurate, high-resolution modeling in these elements may require prohibitively high computing efforts with conventional finite element methods. The adaptive Voronoi cell finite element model [26, 34, 48–50] is, therefore, preferred for efficient micromechanical analysis.

***Criteria for switching from level-1 to level-2***

Departure from periodicity conditions in the microstructural SERVE is taken as an indicator for the *level-1→level-2* transition. This is in addition to the local gradients in macroscopic variables for *level-0→level-1* transition. A criterion for invoking the *level-1→level-2* change is defined as

$$\frac{\hat{\mathbf{F}}(\sigma_{ij},\varepsilon_{ij})^{l1} - \hat{\mathbf{F}}(\sigma_{ij},\varepsilon_{ij})^{\mathrm{RVE}}}{\hat{\mathbf{F}}(\sigma_{ij},\varepsilon_{ij})^{\mathrm{RVE}}} \geq C_2. \tag{3.34}$$

The function $\hat{\mathbf{F}}$ is a measure of a quantity of interest in terms of local variables $(\sigma_{ij},\varepsilon_{ij})$. In some of the numerical examples, $\hat{\mathbf{F}}$ is expressed as the average inclusion stress in the microstructure. The superscript $l1$ in (3.34) refers to element $E^k_{l1}$. The microstructural boundary value problem is solved with macroscopic displacement solutions from *level-0* imposed on $E^k_{l1}$ boundary. The superscript RVE corresponds to the function being evaluated within each RVE only, by imposing macroscopic strains with periodic boundary conditions on the RVE.

Other criteria have also been used in this level transition. Among them are:

1. *Criterion based on strain energy density.* The ratio of local strain energy density to the average energy density in the RVE is important in the prediction of localization. The criterion suggests that if local strain energy density due to multiaxial straining significantly exceeds that due to uniaxial straining used in the evaluation of homogenization parameters, the onset of damage is likely. Hence *level-1 to level-*2 transition is made if

$$^{\text{actual}}U^M_{\max} \geq R^M_{\max} \times {}^{\text{actual}}U^M_{\text{aver}} \quad \text{or} \quad {}^{\text{actual}}U^I_{\max} \geq R^I_{\max} \times {}^{\text{actual}}U^I_{\text{aver}} \tag{3.35}$$

at more than 1% of all integration points. Here, $U^M = (1/2)S^M_{ijkl}\sigma^M_{ij}\sigma^M_{kl}$, $U^I = (1/2)S^I_{ijkl}\sigma^I_{ij}\sigma^I_{kl}$, and the energy density concentration factors are $R^M = U^M_{\max}/U^M_{\text{aver}}$ and $R^I = U^I_{\max}/U^I_{\text{aver}}$ for unit strain components. $U^M_{\max}$ and $U^I_{\max}$ are the maximum values of $U^M$ and $U^I$ at all

integration points in the RVE, and $U^M_{\text{aver}}$ and $U^I_{\text{aver}}$ are the corresponding RVE-averaged energy densities. The maximum values for the four loading cases are noted as $R^M_{\max}$ and $R^I_{\max}$.

2. *Criterion based on equivalent stress*. In this criterion, *level-1→level-2* transition is made if the local equivalent stress exceeds the average, i.e.,

$$\left(\sigma^m_{\text{eqv}}\right)_{\max} > C_3 * \left(\sigma^m_{\text{eqv}}\right)_{\text{avg}}, \quad \left(\sigma^c_{\text{eqv}}\right)_{\max} > C_3 * \left(\sigma^c_{\text{eqv}}\right)_{\text{avg}} \tag{3.36}$$

at more than 1% of all integration points. $\left(\sigma^m_{\text{eqv}}\right)_{\max}, \left(\sigma^m_{\text{eqv}}\right)_{\text{avg}}$ and $\left(\sigma^c_{\text{eqv}}\right)_{\max}, \left(\sigma^c_{\text{eqv}}\right)_{\text{avg}}$ represent the maximum and average equivalent stresses in the matrix and inclusion phases.

3. *Criterion based on traction at the fiber–matrix interface*. Traction at the fiber–matrix interface is important for predicting failure by debonding. This criterion is postulated as *level-1→level-2* transition occurs if

$$|\hat{T}| > C_4 * |\hat{T}|_{\text{avg}} \quad \text{where} \quad |\hat{T}| = \left(\sqrt{T_n^2 + T_t^2}\right), \tag{3.37}$$

where $|\hat{T}|_{\text{avg}} = \dfrac{\sum_{i=1}^{N_I} |\hat{T}|}{N_I}$ is the average traction at the fiber–matrix interface and $N_I$ is the total number of integration points on interface in the RVE. $C_1, C_2, C_3, C_4$ are chosen from numerical experiments.

### *Transition elements between elements in $\Omega_{l2}$ and $\Omega_{l1/l0}$*

To facilitate gradual transition of scales across the element boundaries, a layer of transition elements $E_{\text{tr}}\left(\in \Omega^{\text{tr}}\right)$ is sandwiched between the macroscopic elements in $\Omega_{l1/l0}$ and microscopic elements in $\Omega_{l2}$, as shown in Fig. 3.13. The elements $E_{\text{tr}}$ are essentially *level-2* elements with compatibility and traction continuity constraints imposed at the interface with $E_{l1}$ or $E_{l0}$ elements. The transition elements are located beyond the *level-2* regions, away from critical hot spots.

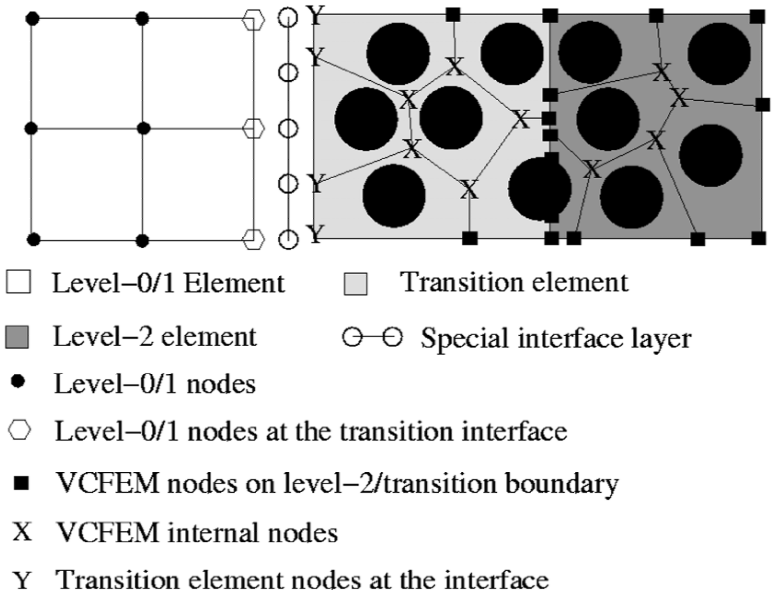


**Fig. 3.13.** Interface constraints between *level-0/1* and transition elements

A relaxed displacement constraint method is proposed in [36, 62], where a weak form of the interface displacement continuity is incorporated by using Lagrange multipliers, suggested in [4]. The total potential energy of the multilevel computational domain can then be expressed as

$$\Pi = \Pi_{\Omega_{l0}} + \Pi_{\Omega_{l1}} + \Pi_{\Omega_{l2}} + \Pi_{\Omega_{\mathrm{tr}}} + \int_{\Gamma_{\mathrm{int}}} \lambda_i^{l1}(v_i - u_i^{l1})\mathrm{d}\Gamma + \int_{\Gamma_{\mathrm{int}}} \lambda_i^{\mathrm{tr}}(v_i - u_i^{\mathrm{tr}})\mathrm{d}\Gamma, \quad (3.38)$$

where $\Pi_{\Omega_{l0}}, \Pi_{\Omega_{l1}}, \Pi_{\Omega_{l2}}$, and $\Pi_{\Omega_{\mathrm{tr}}}$ are the potential energies for elements in the respective subdomains, $\lambda_i^{l1}$ and $\lambda_i^{tr}$ are columns of Lagrange multipliers on the interfacial layer $\Gamma_{\mathrm{int}}$ belonging to $\Omega_{l1}$ and $\Omega_{\mathrm{tr}}$, respectively, for which the interfacial displacements are designated as $u_i^{l1}$ and $u_i^{\mathrm{tr}}$.

As shown in Fig. 3.13, an intermediate boundary segment is added with displacements $v_i$ that may be interpolated with any order polynomial functions, independent of the interpolations for $u_i^{l1}$ or $u_i^{\mathrm{tr}}$. The Lagrange multipliers $\lambda_i^{l1}$ and $\lambda_i^{\mathrm{tr}}$ correspond to the interface tractions on $\partial\Omega_{l1}$ and $\partial\Omega_{\mathrm{tr}}$, respectively. The displacements and the Lagrange multipliers on the

intermediate boundary segment are interpolated from nodal values using suitably assumed shape functions

$$\{\mathrm{v}\} = \left[L_{\mathrm{int}}\right]\{\mathbf{q}_{\mathrm{int}}\}, \quad \left\{\lambda^{l1}\right\} = \left[L_{\lambda^{l1}}\right]\{\mathbf{\Lambda}_{\mathrm{l1}}\}, \quad \left\{\lambda^{\mathrm{tr}}\right\} = \left[L_{\lambda^{\mathrm{tr}}}\right]\{\mathbf{\Lambda}_{\mathrm{tr}}\}. \tag{3.39}$$

To examine the effectiveness of the relaxed displacement constraint method, a composite laminate problem with two sandwiched lamina is solved. The top lamina consists of a uniform distribution of circular fibers of 30% volume fraction, while the bottom lamina has fibers of 10% volume fraction.

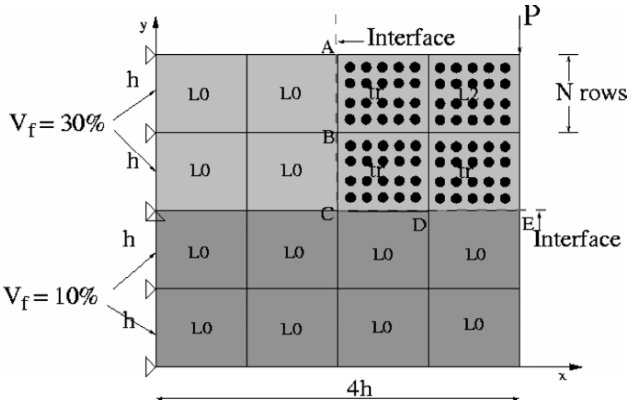


(a)

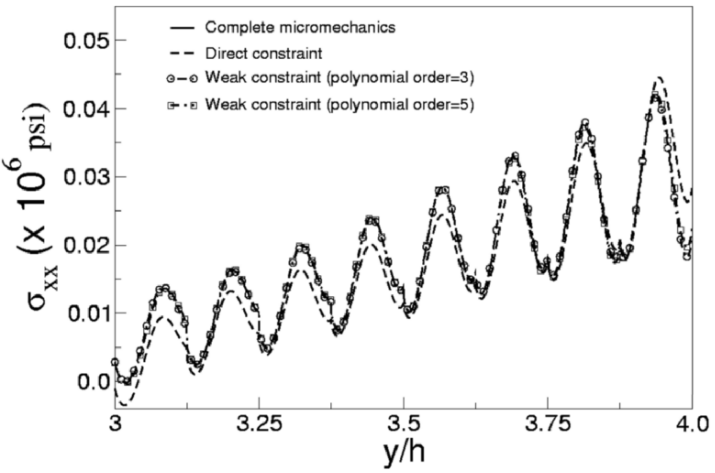


(b)

**Fig. 3.14.** (**a**) Composite laminate subjected to a point load; (**b**) stress $\sigma_{xx}$ produced by the load along the interface A–B by micromechanics, direct displacement, and relaxed displacement constraint methods

A $10^6$ lb point load is applied on the laminate as shown in Fig. 3.14. The fiber material has $E_{\text{fiber}} = 60\times10^6$ psi and $\nu_{\text{fiber}} = 0.2$, while the matrix material has $E_{\text{matrix}} = 0.5\times10^6$ psi and $\nu_{\text{matrix}} = 0.34$. As shown in the Fig. 3.14a, a portion of the top lamina is modeled using VCFEM-based *level-2* and transition elements.

This region consists of eight rows of fiber and, hence, each *level-2* or transition element may contain up to 64 fibers. The remaining elements are *level-0* with homogenized moduli. In the relaxed displacement constraint method, increasing order polynomials are considered for the displacement interpolation $\left[L_{\text{int}}\right]$ on the intermediate boundary segment between A and E. The shape functions $\left[L_{\lambda^{l1}}\right]$ and $\left[L_{\lambda^{\text{tr}}}\right]$ in (3.39) are assumed to be linear. The critical stress $\sigma_{xx}$ distribution is shown along the section A–B for different interfacial conditions. The solutions of the multilevel models are compared with that of a fully micromechanical model analyzed by VCFEM. The plots in Fig. 3.14b show that relaxed displacement constraint method yields much better results compared with a direct constraint method done in [61, 62].

### 3.3.3 Coupling Levels in the Concurrent Multilevel FEM

The global stiffness matrix and load vectors are derived for the multilevel model consisting of *level-0*, *level-1*, *level-2*, and transition elements, i.e., $\Omega_{\text{het}} = \left\{\Omega_{l0}\bigcup\Omega_{l1}\bigcup\Omega_{\text{tr}}\bigcup\Omega_{l2} : \Omega_{l0} = \bigcup_{k=1}^{N_{l0}} E_{l0}; \bigcup_{k=1}^{N_{l1}} E_{l1}; \bigcup_{k=1}^{N_{tr}} E_{\text{tr}}; \bigcup_{k=1}^{N_{l2}} E_{l2}\right\}$. The boundary is decomposed as $\Gamma_{\text{het}} = \left\{\Gamma_{l0}\bigcup\Gamma_{l1}\bigcup\Gamma_{l2}\bigcup\Gamma_{\text{tr}}\right\}$, where $\Gamma_{l0} = \partial\Omega_{l0}\bigcap\Gamma_{\text{het}}$, $\Gamma_{l1} = \partial\Omega_{l1}\bigcap\Gamma_{\text{het}}$, $\Gamma_{\text{tr}} = \partial\Omega_{\text{tr}}\bigcap\Gamma_{\text{het}}$ and $\Gamma_{l2} = \partial\Omega_{l2}\bigcap\Gamma_{\text{het}}$. The principle of virtual work equation for the entire multilevel computational domain for multiscale analysis is expressed as

$$
\begin{aligned}
&\int_{\Omega_{l0}}\Sigma_{ij}\frac{\partial\delta u_i^{10}}{\partial x_j}\mathrm{d}\Omega - \int_{\Omega_{l0}} f_i\delta u_i^{10}\,\mathrm{d}\Omega + \int_{\Omega_{l1}}\Sigma_{ij}\frac{\partial\delta u_i^{11}}{\partial x_j}\mathrm{d}\Omega - \int_{\Omega_{l1}} f_i\delta u_i^{11}\,\mathrm{d}\Omega \\
&+\int_{\Omega_{l2}}\sigma_{ij}\frac{\partial\delta u_i^{12}}{\partial x_j}\mathrm{d}\Omega - \int_{\Omega_{l2}} f_i\delta u_i^{12}\,\mathrm{d}\Omega + \int_{\Omega_{tr}}\sigma_{ij}\frac{\partial\delta u_i^{\text{tr}}}{\partial x_j}\mathrm{d}\Omega - \int_{\Omega_{\text{tr}}} f_i\delta u_i^{\text{tr}}\,\mathrm{d}\Omega \\
&-\int_{\Gamma_{10}} t_i\delta u_i^{10}\,\mathrm{d}\Gamma - \int_{\Gamma_{11}} t_i\delta u_i^{11}\,\mathrm{d}\Gamma - \int_{\Gamma_{12}} t_i\delta u_i^{12}\,\mathrm{d}\Gamma - \int_{\Gamma_{\text{tr}}} t_i\delta u_i^{\text{tr}}\,\mathrm{d}\Gamma \\
&+\delta\int_{\Gamma_{\text{int}}}\lambda_i^{10/11}(v_i - u_i^{10/11})\mathrm{d}\Gamma + \delta\int_{\Gamma_{\text{int}}}\lambda_i^{\text{tr}}(v_i - u_i^{\text{tr}})\mathrm{d}\Gamma = 0.
\end{aligned}
\tag{3.40}
$$

The traction continuity between *level-0* and *level-1*, as well as *level-2* and transition elements are satisfied in a weak sense. The boxed terms in (3.40) involve integration over the microstructural domains $\Omega_{l2}$ and $\Omega_{\text{tr}}$, and are analyzed using VCFEM, described in Sect. 3.2.2. It is necessary to couple these terms with the other terms using homogenized properties, analyzed by conventional finite element models. To make the connection with the macroscopic elements in the model, the total energy in the ensemble of Voronoi cell elements in (3.25) is identified as the energy of the *level-2* or transition elements, i.e., $\Pi^{E_{l2}/E_{\text{tr}}} = \Pi^{\text{VCE}}_{\text{Total}}$. Furthermore, element boundaries of all Voronoi cell elements are split as $\sum_{e=1}^{N_{\text{VCE}}} \partial\Omega_e^{\text{VCE}} = \partial\Omega^{\text{ext}} \bigcup \partial\Omega^{\text{int}}$. $\partial\Omega^{\text{ext}}$ is the aggregate of all Voronoi element boundaries that coincides with *level-2* or transition element boundaries, shown with thicker lines in Fig. 3.12b, and $\partial\Omega^{\text{int}}$ corresponds to all other internal boundaries of VC elements. Substitution in (3.26c) yields

$$-\int_{\partial\Omega^{\text{int}}} \boldsymbol{\sigma}\cdot\mathbf{n}^e\cdot\delta\mathbf{u}^e\,\mathrm{d}\partial\Omega - \int_{\partial\Omega^{\text{ext}}} \boldsymbol{\sigma}\cdot\mathbf{n}^e\cdot\delta\mathbf{u}^e\,\mathrm{d}\partial\Omega + \sum_{e=1}^{N_\Gamma}\int_{\Gamma_{\text{t}}^{\text{VCE}}} \overline{\mathbf{t}}\cdot\delta\mathbf{u}^e\,\mathrm{d}\Gamma = 0. \quad (3.41)$$

In the absence of body forces, the boxed terms in (3.40) corresponding to the micromechanical energy in each *level-2 or transition* element can be restated by using divergence theorem as

$$\begin{aligned}
&\int_{E_{12}/E_{\text{tr}}} \boldsymbol{\sigma}\cdot\nabla\delta\mathbf{u}^{12/\text{tr}}\,\mathrm{d}\Omega - \int_{\Gamma_{12}/\Gamma_{\text{tr}}} \mathbf{t}\cdot\delta\mathbf{u}^{12/\text{tr}}\,\mathrm{d}\Gamma = \int_{\partial E_{12}/\partial E_{\text{tr}}} \boldsymbol{\sigma}\cdot\mathbf{n}^e\cdot\delta\mathbf{u}^{12/\text{tr}}\,\mathrm{d}\partial\Omega \\
&-\int_{E_{12}/E_{\text{tr}}} \nabla\boldsymbol{\sigma}\cdot\delta\mathbf{u}^{12/\text{tr}}\,\mathrm{d}\Omega - \int_{\Gamma_{12}/\Gamma_{\text{tr}}} \mathbf{t}\cdot\delta\mathbf{u}^{12/\text{tr}}\,\mathrm{d}\Gamma = \int_{\partial\Omega^{\text{ext}}} \boldsymbol{\sigma}\cdot\mathbf{n}^e\cdot\delta\mathbf{u}^{12/\text{tr}}\,\mathrm{d}\partial\Omega \qquad (3.42)\\
&-\sum_{e=1}^{N_{\text{VCE}}}\int_{\Omega_e^{\text{VCE}}} \nabla\boldsymbol{\sigma}\cdot\delta\mathbf{u}^{12/\text{tr}}\,\mathrm{d}\Omega - \sum_{e=1}^{N_\Gamma}\int_{\Gamma_{\text{t}}^{\text{VCE}}} \mathbf{t}\cdot\delta\mathbf{u}^{12/\text{tr}}\mathrm{d}\Gamma.
\end{aligned}$$

The term containing $\nabla\boldsymbol{\sigma}$ in (3.42) drops out, since equilibrated stress fields are used in VCFEM. It should be noted that the boundary vector $\mathbf{u}^{12/\text{tr}}$ is a subset of the VCFEM boundary displacements $\mathbf{u}^e$. The first term on the right-hand side is the contribution to the global stiffness and is obtained from VCFEM analysis by using static condensation in (3.41) to remove internal degrees of freedom on $\partial\Omega^{\text{int}}$ from the global stiffness. The displacement field along the edges of VCFEM elements is interpolated as

$$\left\{\mathbf{u}^e\right\} = \left[L_{\text{VCE}}\right]\left\{\mathbf{q}_{\text{VCE}}\right\}. \quad (3.43)$$

The degrees of freedom $\mathbf{q}_{\mathrm{VCE}}$ can be separated into $\mathbf{q}_{\mathrm{VCE}}^{\mathrm{ext}}$ and $\mathbf{q}_{\mathrm{VCE}}^{\mathrm{int}}$ depending on whether they belong to $\partial\Omega^{\mathrm{ext}}$ or $\partial\Omega^{\mathrm{int}}$, respectively. The stiffness matrix and the load vector of the ensemble of all Voronoi cell elements belonging to a *level-2* element or transition element can thus be partitioned as

$$\begin{pmatrix} K_{\mathrm{VCE}}^{\mathrm{ext,ext}} & K_{\mathrm{VCE}}^{\mathrm{ext,int}} \\ K_{\mathrm{VCE}}^{\mathrm{int,ext}} & K_{\mathrm{VCE}}^{\mathrm{int,int}} \end{pmatrix} \begin{Bmatrix} \mathbf{q}_{\mathrm{VCE}}^{\mathrm{ext}} \\ \mathbf{q}_{\mathrm{VCE}}^{\mathrm{int}} \end{Bmatrix} = \begin{Bmatrix} \mathbf{F}_{\mathrm{VCE}}^{\mathrm{ext}} \\ \mathbf{F}_{\mathrm{VCE}}^{\mathrm{int}} \end{Bmatrix}. \tag{3.44}$$

Static condensation of the internal degrees of freedom leads to

$$\begin{aligned} &\left[\left[K_{\mathrm{VCE}}^{\mathrm{ext,ext}}\right] - \left[K_{\mathrm{VCE}}^{\mathrm{ext,int}}\right]\left[K_{\mathrm{VCE}}^{\mathrm{int,int}}\right]^{-1}\left[K_{\mathrm{VCE}}^{\mathrm{int,ext}}\right]\right]\left\{\mathbf{q}_{\mathrm{VCE}}^{\mathrm{ext}}\right\} = \left\{\mathbf{F}_{\mathrm{VCE}}^{\mathrm{ext}}\right\} \\ &- \left[K_{\mathrm{VCE}}^{\mathrm{ext,int}}\right]\left[K_{\mathrm{VCE}}^{\mathrm{int,int}}\right]^{-1}\left\{\mathbf{F}_{\mathrm{VCE}}^{\mathrm{int}}\right\}. \end{aligned} \tag{3.45}$$

This form is used in global assembly. The displacements $u_i^{l0}$ and $u_i^{l1}$ in each *level-0* and *level-1* element are interpolated by the standard or hierarchical shape functions based on Legendre polynomials as

$$\{\mathbf{u}\}^{10} = \left[N_{10}\right]\{\mathbf{q}_{10}\} = \left[N_{10}^{\mathrm{I}} N_{10}^{\mathrm{O}}\right]\begin{Bmatrix} \mathbf{q}_{10}^{\mathrm{I}} \\ \mathbf{q}_{10}^{\mathrm{O}} \end{Bmatrix}, \{\mathbf{u}\}^{11} = \left[N_{11}\right]\{\mathbf{q}_{11}\} = \left[N_{11}^{\mathrm{I}} N_{11}^{\mathrm{O}}\right]\begin{Bmatrix} \mathbf{q}_{11}^{\mathrm{I}} \\ \mathbf{q}_{11}^{\mathrm{O}} \end{Bmatrix}, \tag{3.46}$$

where $\left\{\mathbf{q}_{10}^{\mathrm{I}}\right\} / \left\{\mathbf{q}_{11}^{\mathrm{I}}\right\}$ corresponds to the nodal degrees of freedom at the interface with transition elements and $\left\{\mathbf{q}_{10}^{\mathrm{O}}\right\} / \left\{\mathbf{q}_{11}^{\mathrm{O}}\right\}$ corresponds to the remaining degrees of freedom. A similar separation can also be done for nodal displacements of transition elements into displacements on this interface. The displacements and the Lagrange multipliers on the intermediate boundary segment between the *level-0/1* and transition elements are interpolated according to (3.39). Substituting (3.45), (3.46), and (3.39) in (3.40) results in a coupled set of matrix equations for the multilevel domain:

$$\begin{bmatrix} K_{10/11}^{\mathrm{I,I}} & K_{10/11}^{\mathrm{I,O}} & 0 & 0 & 0 & P_{10/11} & 0 \\ K_{10/11}^{\mathrm{O,I}} & K_{10/11}^{\mathrm{O,O}} & 0 & 0 & 0 & 0 & 0 \\ 0 & 0 & K_{\mathrm{tr}}^{\mathrm{I,I}} & K_{12/\mathrm{tr}}^{\mathrm{I,O}} & 0 & 0 & P_{\mathrm{tr}} \\ 0 & 0 & K_{12/\mathrm{tr}}^{\mathrm{O,I}} & K_{12/\mathrm{tr}}^{\mathrm{O,O}} & 0 & 0 & 0 \\ 0 & 0 & 0 & 0 & 0 & Q_{10/11} & Q_{\mathrm{tr}} \\ P_{10/11}^{\mathrm{T}} & 0 & 0 & 0 & Q_{10/11}^{\mathrm{T}} & 0 & 0 \\ 0 & 0 & P_{\mathrm{tr}}^{\mathrm{T}} & 0 & Q_{\mathrm{tr}}^{\mathrm{T}} & 0 & 0 \end{bmatrix} \begin{Bmatrix} \mathbf{q}_{10/11}^{\mathrm{I}} \\ \mathbf{q}_{10/11}^{\mathrm{O}} \\ \mathbf{q}_{\mathrm{tr}}^{\mathrm{I}} \\ \mathbf{q}_{12/\mathrm{tr}}^{\mathrm{O}} \\ \mathbf{q}_{\mathrm{int}} \\ \mathbf{\Lambda}_{10/11} \\ \mathbf{\Lambda}_{\mathrm{tr}} \end{Bmatrix} = \begin{Bmatrix} \mathbf{F}_{10/11}^{\mathrm{I}} \\ \mathbf{F}_{10/11}^{\mathrm{O}} \\ \mathbf{F}_{\mathrm{tr}}^{\mathrm{I}} \\ \mathbf{F}_{12/\mathrm{tr}}^{\mathrm{O}} \\ 0 \\ 0 \\ 0 \end{Bmatrix}. \tag{3.47}$$

Superscript I represents quantities on the interface with transition elements, while superscript O corresponds to other regions. The submatrices $K_{10/11}$, $K_{12}$, and $K_{\text{tr}}$ and vectors $\mathbf{F}_{10/11}$, $\mathbf{F}_{12}$, and $\mathbf{F}_{\text{tr}}$ correspond to stiffness matrices and load vectors from the respective subdomains. The stiffness $[K_{12/\text{tr}}]$ and the load vectors $\{\mathbf{F}_{12/\text{tr}}\}$ are obtained from VCFEM analysis. The coupling between the *level-0/1* and transition elements is achieved through the $[P]$ and $[Q]$ matrices. The system of equations is solved using an iterative solver with the Lanczos method.

### 3.3.4 Numerical Examples with the Adaptive Multilevel Model

Three sets of numerical examples are solved to study the effectiveness of the multilevel computational model for heterogeneous materials.

#### *Composite laminate with a free edge*

A classical problem of a composite laminate with a free edge that was introduced by Pagano and Rybicki [58, 67] is solved by the multilevel adaptive computational model. The problem to be solved is illustrated in Fig. 3.3 with out-of-plane loading. The homogenized solution of this problem yields a singular stress field near the free edge between the composite ply and the monolithic material layer, due to the constraints imposed by the free edge and Poisson's effect. The stress singularity has been reported in [58] as ($d^{-a}$), where $d$ is the radial distance from the edge and the exponent $a < 0.1$. However, the micromechanics solution does not show any singularity and hence the macroscopic solution is grossly misrepresented in this region. The material properties for the boron fiber and epoxy matrix are:

| $E_{\text{bo}}$ (psi) | $\nu_{\text{bo}}$ | $E_{\text{epoxy}}$ (psi) | $\nu_{\text{epoxy}}$ |
|---|---|---|---|
| $60\times10^6$ | 0.2 | $0.5\times10^6$ | 0.34 |

The ratio of fiber radius to edge length in the RVE is $r/l = 0.3$, corresponding to a local volume fraction of 28.2%. For 40 rows of fiber, the microstructural RVE is assumed to be a unit cell of size $l = h/40$. The homogenized orthotropic stiffness coefficients are obtained as: $E_{xx} = E_{yy} = 0.99\times10^6$ psi, $E_{xx} = E_{yy} = 0.99\times10^6$ psi, $E_{zz} = 1.72\times10^6$ psi, $G_{xy} = 0.27\times10^6$ psi, $\nu_{xy} = 0.43$, $\nu_{zx} = \nu_{zy} = 0.29$. Only a quarter of the laminate

is modeled, accounting for symmetry about $xz$ and $yz$ planes by imposing symmetry boundary conditions on $x = 0$ and $y = 0$ surfaces. The top ($y = 2h$) and right ($x = 4h$) surfaces are assumed to be traction free. The out-of-plane loading is simulated using a generalized plane strain condition with prescribed $\varepsilon_{zz} = 1$. The problem solved is for the number of fiber rows ($n = 40$) corresponding to approximately 6,400 fibers. The initial mesh in the multilevel model consists of 200 QUAD4 *level-0* elements. The adaptive model consists of *hp*-adaptation, and the three level transitions for control of the discretization and modeling errors, respectively.

The *level-0* to *level-1* transition parameter $C_1 = 0.3$ in (3.32), $E_k$ is based on traction discontinuity defined by (3.33c) and *level-1* to *level-2* transition takes place according to (3.34) with

$$\hat{\mathbf{F}} = \frac{1}{A_c}\int_{\omega} \sigma_{yy}(\mathbf{v})\, \mathrm{d}A_c. \tag{3.48}$$

$\hat{\mathbf{F}}$ is an inclusion area averaged stress and $A_c$ is its cross-sectional area. Figure 3.15a shows the multilevel mesh consisting of 242 *level-0* elements, four *level-1* elements, six *transition* elements, and five *level-2* elements. Each *level-2* element in this model is assumed to contain a single unit cell or RVE. The same problem is also solved using the commercial code ANSYS with a mesh of 30,000 elements (50,000 nodes). A $3 \times 3$ array of nine fibers near the free edge and laminate interface are explicitly modeled using a highly refined mesh (see Fig. 3.15c) and coupled with the remaining macroscopic analysis mesh. The multilevel model has a significantly smaller size with DOF=2,000 ($2 \times$ no. of nodes in *level-0* + *level-1* + *level-2* elements + # of $\beta$s in *level-2* elements). Fig. 3.16a compares the stress $\sigma_{yy}$ along the line $y/h = 1$ near the free edge $x/h = 4$ for two values of $C_1$ by (a) the homogenized material law (gives rise to a singularity), (b) the microscopic stress obtained by VCFEM, and (c) the microscopic stress from the ANSYS analysis. The singularity vanishes for the microscopic results and the ANSYS and multilevel model results compare very well.

In a second study, the effect of *level-1 to level-2* switch-over criteria in (3.35)–(3.37) are examined with $C_3 = 3.0$ and $C_4 = 1.5$. The criteria (a) and (b) in (3.35) and (3.36) lead to 242 *level-0* elements, four *level-1* elements, six transition elements, and five *level-2* elements. Criterion (c) in (3.37)

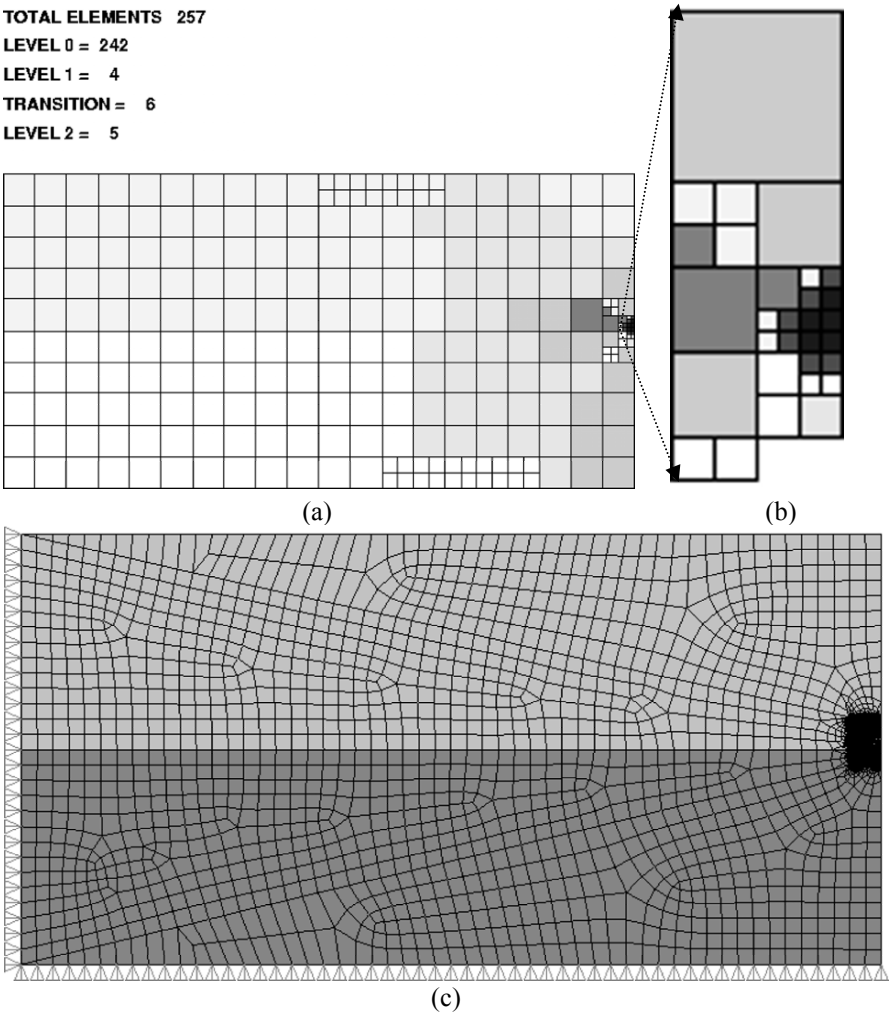


**Fig. 3.15.** (**a**) hp-Adapted multilevel mesh showing *level-0*, *level-1*, and *level-2* elements; (**b**) blow-up of the free-edge interface region mesh; and (**c**) ANSYS mesh with detailed microstructure modeled near the free edge

yields 245 *level-0* elements, four *level-1* elements, five transition elements, and three *level-2* elements, and criterion (d) in (3.34) yields 245 *level-0* elements, five *level-1* elements, five transition elements, and two *level-2* elements.

The stress $\sigma_{yy}$ along $y/h = 1$ near $x/h = 4$ is compared in Fig. 3.16b. The agreement between the ANSYS and multilevel model results is excellent. Criteria (c,d) are more efficient due to a lesser number of *level-2* elements.

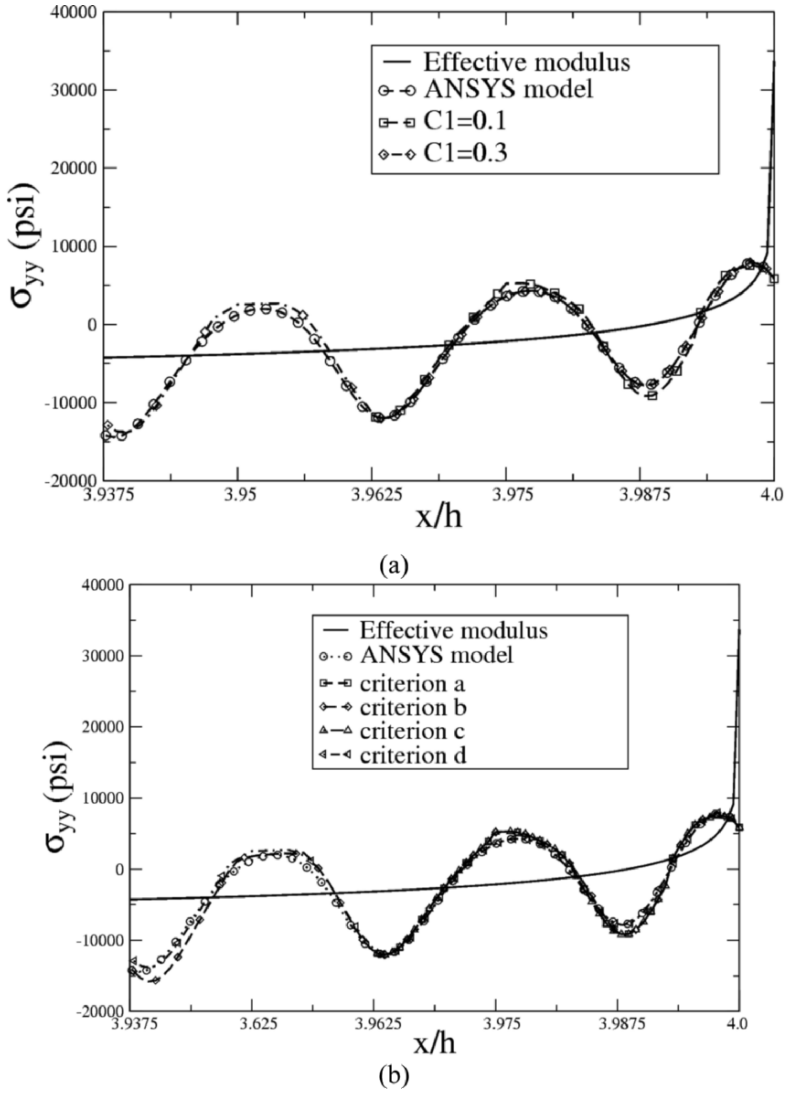


**Fig. 3.16.** Convergence of microscopic *level-2* stress $\sigma_{yy}$ along section A–A near the critical free edge with different: (**a**) *level-0* to *level-1* and (**b**) *level-1* to *level-2* transition criteria

### *Comparison with GOALS algorithm-based multiscale modeling*

In [56, 79], Oden et al. have introduced a theory of a posteriori modeling error estimates based on local quantities of interest, cast in terms of a linear functional $L(\mathbf{u})$. The goal-oriented adaptive local solution or GOALS

algorithm is applied to the homogenized solution for estimating the local error in quantities of interest due to modeling a heterogeneous material as a homogenized medium. Subsequent to estimating the error, the algorithm adaptively adjusts the calculated quantities by adding microscale data until preset levels of accuracy are attained. The method entails solving an additional adjoint homogenized problem, in which $L(\mathbf{u})$ serves as the load vector. A measure $\beta$ is defined as a local estimator of the modeling error as

$$| L(\mathbf{u}-\mathbf{u}^0) | \leq \beta = \zeta_{\text{upp}}\overline{\zeta}_{\text{upp}} + \zeta_{\text{upp}} \| \mathbf{w}^0 \|_{E(\Omega)}, \tag{3.49}$$

where $\zeta_{\text{upp}}$ and $\overline{\zeta}_{\text{upp}}$ are the upper bound of the energy norm-based modeling error in the primal problem and the adjoint problem respectively and $\| \mathbf{w}^0 \|_{E(\Omega)}$ is the energy norm of the influence function. A domain of influence is determined as a local region or "cell" *k* for which the local error estimator $\beta_k$ exceeds a prescribed tolerance. An *m-shaped* domain with randomly distributed cylindrical inclusions, having an average volume fraction 0.3 is depicted in Fig. 3.17a. The matrix material properties are $E = 100\,\text{MPa}$, $\nu = 0.2$, and inclusion properties are $E = 1,000\,\text{MPa}$, $\nu = 0.2$. The domain is subjected to a distributed load of $\mathbf{W} = 1\,\text{MN m}^{-1}$ under plane strain conditions. The domain is initially discretized into 42 *level-0* elements and homogenized properties for *level-0* and *level-1* elements are computed using a unit cell consisting of a single circular inclusion of 30% volume fraction. A local quantity of interest is ascertained in [79] as the inclusion area-averaged stress $\sigma_{xx}$:

$$L(\mathbf{v}) = \frac{1}{A_c}\int_{\omega} \sigma_{xx}(\mathbf{v})\mathrm{d}A_c, \tag{3.50}$$

where $A_c$ is the inclusion cross-sectional area. The distribution of $\beta_k$ is shown in the contour plot of Fig. 3.17b. In the application of the multilevel model, adaptation criteria in (3.32), (3.33a), and (3.34) are chosen. Consistent with (3.34), *the level-1 to level-2* switch takes place if

$$\hat{\sigma}_{xx}^{level\text{-}1} - \hat{\sigma}_{xx}^{\text{RVE}} \geq C_2 \hat{\sigma}_{xx}^{\text{RVE}}, \tag{3.51}$$

where

$$\hat{\sigma}_{xx} = \sum_{i}^{\#\,\text{inclusions}} \frac{1}{A_{ci}}\int_{\omega_i} \sigma_{xx}(\mathbf{v})\mathrm{d}A_{ci}.$$

The adaptation parameters are chosen as $C_1 = 0.1$ and $C_2 = 0.1$. The domain of influence has been calculated in [79] by the GOALS algorithm using the local quantity corresponding to an inclusion marked as $\omega$, shown in Fig. 3.17a. The corresponding distribution of levels in the computational domain with the multilevel model are shown in Fig. 3.17c.

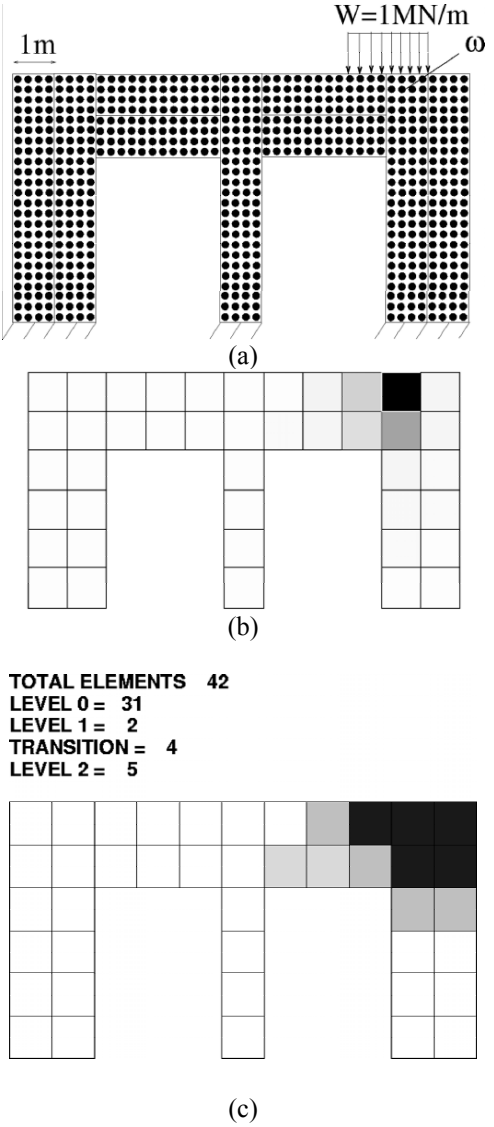


**Fig. 3.17.** (a) An *m*-shaped domain with uniformly distributed inclusions; (b) plot of $\beta_k$ normalized with respect to its maximum for the quantity of interest $L_2$; (c) multilevel mesh with adaptation tolerances $C_1 = 0.1$, $C_2 = 0.1$

The GOALS algorithm [56, 79] conducts a microscopic analysis on six adjacent cells with high $\beta_k$ (see Fig. 3.17b) to achieve 0.5% relative modeling error $(L(\mathbf{u}-\tilde{\mathbf{u}})/L(\mathbf{u}))\times 100\%$. In the present multilevel model, error is computed using $(L(\mathbf{u}-\mathbf{u}^{\mathbf{0}})/L(\mathbf{u}))= 0.743$ (as reported in [79]) and $L(\tilde{\mathbf{u}}) = 0.1554$ calculated from the solution of the *level-2* VCFEM in the same inclusion. The corresponding value of relative modeling error $(L(\mathbf{u}-\tilde{\mathbf{u}})/L(\mathbf{u}))\%$ is 0.45%, in comparison with the 0.5% in [56]. Thus the modeling error with multilevel adaptation is quite satisfactory.

***A double lap aluminum-composite bonded joint***

Adhesive bonded joints consisting of different materials are used to repair damaged structures in aircraft industries [66]. They can induce high stresses near the interface leading to failure initiation by fiber cracking, fiber–matrix interfacial debonding or interfacial delamination. A double-lap bonded joint with aluminum and boron-epoxy composite as the adherents is analyzed as shown in Fig. 3.18a. The dimension *h* is 64 mm with a total of 14 million fibers in the composite laminate. A perfect interface, corresponding to displacement continuity, is assumed between the aluminum and composite materials. Symmetry boundary conditions are employed in a quarter symmetry model with displacement component $u_y = 0$ on $y = 0$ and $u_x = 0$ along $x = 0$ as depicted in Fig. 3.18b. Displacement $u_x = 1$ is applied on the face $x = h$. The microstructure and RVE are the same as in Sect. 3.2.3. The material properties are

| Material | Young's modulus, *E* (GPa) | Poisson ratio |
|---|---|---|
| Aluminum | $E_{\text{al}} = 73.8$ | $\nu_{\text{al}} = 0.25$ |
| Epoxy (matrix) | $E_{\text{epoxy}} = 3.45$ | $\nu_{\text{epoxy}} = 0.3$ |
| Boron (fiber) | $E_{\text{boron}} = 413$ | $\nu_{\text{boron}} = 0.2$ |

The components of the homogenized elastic stiffness matrix for the composite are

| $E_{1111}$ (GPa) | $E_{1122}$ (GPa) | $E_{1133}$ (GPa) | $E_{2222}$ (GPa) | $E_{2233}$ (GPa) | $E_{1212}$ (GPa) | $E_{3333}$ (GPa) |
|---|---|---|---|---|---|---|
| 9.93 | 4.39 | 4.14 | 10.59 | 4.27 | 2.58 | 137.32 |

The initial *level-0* mesh consists of 225 *level-0* QUAD4 elements. *Level-0* macroscopic stresses at the bonded interface $y = 0.5h$ are plotted

in Fig. 3.19. In the composite, a high gradient of the tensile stress $\Sigma_{xx}$ results near the interface A at $x = 0.25h$, with a high peak at A. Subsequently, $\Sigma_{xx}$ drops to a very small value between $x = 0.25h$ and $x = 0.5h$. The composite stress $\Sigma_{yy}$ (not shown) is compressive and exhibits a singular behavior at $x = 0.25h$ due to material mismatch and free edge constraints. The shear stress $\Sigma_{xy}$ is generally zero in the composite along this line,

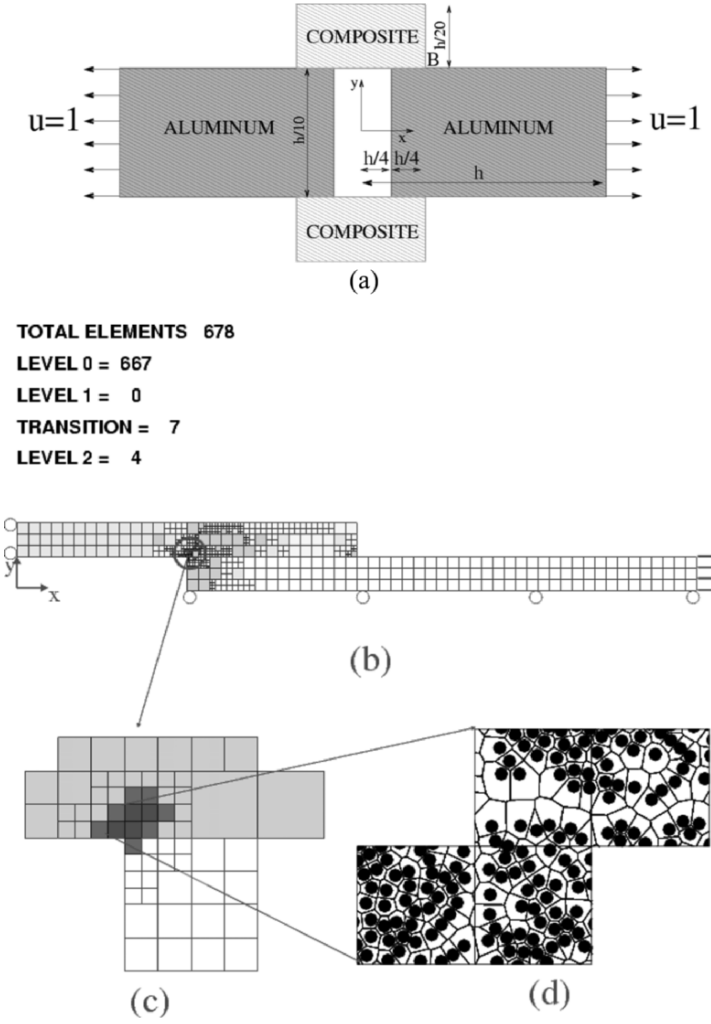


**Fig 3.18.** (**a**) Double-lap aluminum/boron-epoxy composite bonded joint, (**b**) macroscopic model of multilevel mesh, (**c**) zoomed in region of the macroscopic mesh undergoing level transition, (**d**) microscopic VCFEM analysis *level-2* regions

with the exception near A, where it exhibits a sharp gradient with a sign reversal. The small peaks at $x = 0.5h$ result from free edge conditions. In the aluminum panel, the stresses $\Sigma_{xx}$ and $\Sigma_{xy}$ start from zero at $x = 0.25h$ and reach a maximum with a very high gradient near the point A. Subsequently, they stabilize at lower values, satisfying the traction free boundary conditions on the top surface $y = 0.05h$. The stress $\Sigma_{yy}$ is also compressive and very high near the interface $x = 0.25h$. These macroscopic results

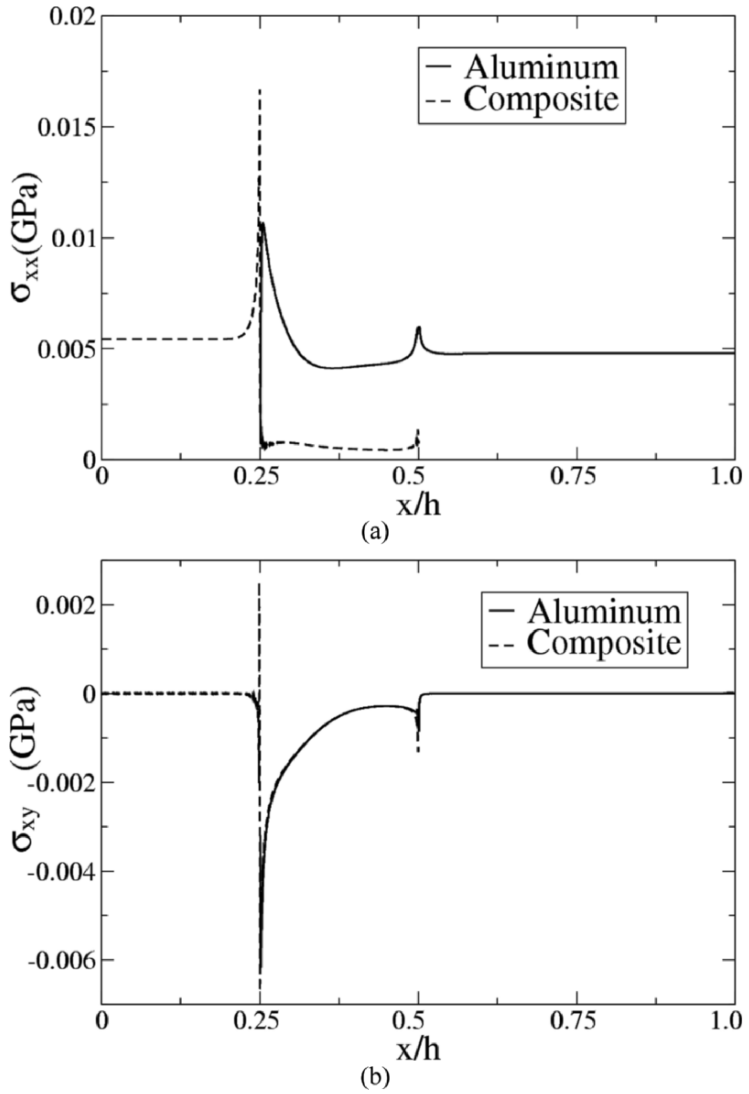


**Fig. 3.19.** Stresses (**a**) $\Sigma_{xx}$ ; (**b**) $\Sigma_{xy}$ in aluminum and composite at $y = 0.05h$

qualitatively match the predictions of stresses made in [66]. The adapted multiple levels showing the microstructural region are depicted in Fig. 3.18. $E_k$ in (3.32) is based on $\Sigma_{xx}$ and *level-1* to *level-2* transition takes place according to (3.51). The evolved multilevel mesh in Fig. 3.18b, c has 667 *level-0* elements, seven transition elements, and four *level-2* elements. The *level-2* elements consist of a total of 203 microstructural Voronoi cell elements. Plots in Fig. 3.20 compares (a) the *level-0* macroscopic stress, (b) the *level-2* microscopic stress, and (c) the average microscopic stress, in the *x*-direction near the critical point A. The homogenized stresses do not match with the average microscopic stresses near A. However, they are

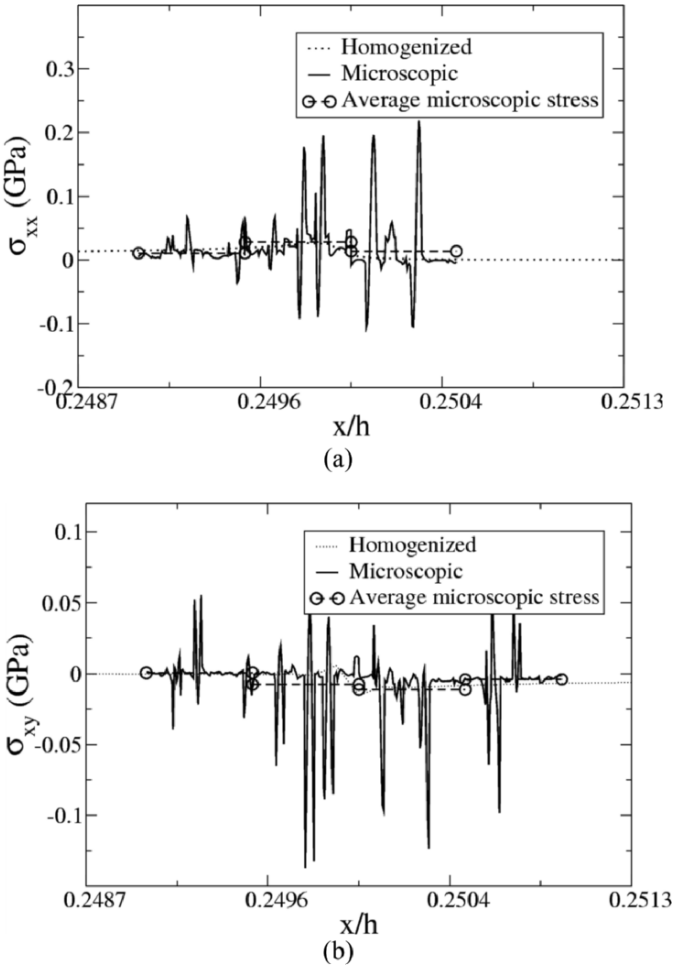


**Fig. 3.20.** *Level-2* stress (**a**) $\sigma_{xx}$; (**b**) $\sigma_{xy}$ in aluminum and composite at $y = 0.05h$

the same away from the critical region, proving that homogenization is not effective at critical singular regions. The solution demonstrates the ability of the multilevel computational model in analyzing real problems with high efficiency and accuracy.

## 3.4 Multilevel Model for Damage Analysis in Composites

The adaptive concurrent multiscale modeling framework developed in Sect. 3.3 is extended to problems of composite structures undergoing damage initiation and growth due to microstructural damage induced by debonding at the fiber–matrix interface. Important changes in the three-level framework in the presence of damage are:

1. Incremental formulation is necessary to account for the history and path dependence of evolving damage.
2. The Voronoi cell FEM explicitly incorporates evolving damage (by interfacial debonding here) in the microstructure with inclusions.
3. An anisotropic continuum damage mechanics (CDM) model is developed for constitutive modeling of *level-0* elements to replace the constant homogenized stiffness in pure elastic problems.

The CDM model has been developed for unidirectional fiber-reinforced composites undergoing interfacial debonding by using homogenization theory in [36, 63]. It homogenizes the damage incurred through initiation and growth of interfacial debonding in a microstructural RVE and can effectively handle arbitrary loading conditions. An important assumption that is made in the derivation of this CDM is that the size of the RVE SERVE remains the same throughout the damage process. Extensive discussion of evolving damage in composites is provided in Talreja et al. [12, 76]. In [73], it has been shown that as the extent of damage increases with increasing strain, the SERVE size also increases. Continual increase in the SERVE size with evolving damage provides ground for its restricted use in homogenization schemes that use RVEs for evaluating continuum constitutive models. The breakdown of SERVE leads to the consideration of the *level-2* elements in these regions.

In [36], the CDM model of [63] is incorporated in an adaptive concurrent multilevel computational model to analyze multiscale evolution of damage in composites. Damage by fiber–matrix interface debonding is explicitly modeled over extended microstructural regions at critical locations using the Voronoi cell FEM developed in [34, 45], where a layer of cohesive springs model in the fiber–matrix interface. In this section, the

adaptive multilevel modeling framework is discussed for composites with evolving damage with numerical examples demonstrating its effectiveness.

### 3.4.1 Voronoi Cell FEM with Microstructural Damage

The micromechanical Voronoi cell FEM outlined in Sect. 3.3.2 is extended for incorporating explicit damage evolution in the form of interfacial debonding as detailed in [34, 45]. Figure 3.21a shows a schematic of a typical Voronoi cell element with nonlinear cohesive zone springs characterizing the matrix–inclusion interface springs. Cohesive zone models are effective in depicting material failure as a separation process across an extended crack tip [36, 42, 63]. They introduce softening constitutive equations relating crack surface tractions to the material separation across the crack. The tractions across the interface reach a maximum, subsequently decrease, and eventually vanish with increasing interfacial separation. Motivated by interatomic potentials in atomistic modeling, many cohesive laws use a potential function $\phi$ to describe the traction–displacement relation during material separation. The traction–displacement relation of a bilinear model in [57] is depicted in Fig. 3.21b, c. The magnitude of traction $t$ is expressed as a bilinear function of the interfacial separation as

$$t = \frac{\delta}{\delta_c}\sigma_{\max} \quad \forall \delta < \delta_c \quad \text{and} \quad t = \frac{\delta - \delta_e}{\delta_c - \delta_e}\sigma_{\max} \quad \forall \delta \geq \delta, \tag{3.52}$$

from which the normal and tangential traction components are derived as

$$T_n = \frac{\partial \phi}{\partial \delta_n} = \begin{cases} \sigma_{\max}\dfrac{\delta_n}{\delta_c} \\ \sigma_{\max}\dfrac{\delta - \delta_e}{\delta_c - \delta_e}\dfrac{\delta_n}{\delta} \\ 0 \end{cases} \quad \text{and} \quad T_t = \frac{\partial \phi}{\partial \delta_t} = \begin{cases} \beta^2\sigma_{\max}\dfrac{\delta_t}{\delta_c} & \forall \delta \leq \delta_c \\ \beta^2\sigma_{\max}\dfrac{\delta - \delta_e}{\delta_c - \delta_e}\dfrac{\delta_t}{\delta} & \forall \delta_c < \delta \leq \delta_e \\ 0 & \forall \delta > \delta_e \end{cases}. \tag{3.53}$$

When the normal displacement $\delta_n$ is positive, the traction at the interface increases linearly to a maximum value of $\sigma_{\max}$ (point $A$ in Fig. 3.21b, c) corresponding to a value of $\delta_c$ before it starts decreasing to zero at a value of $\delta_e$ (point $C$). The unloading behavior in the hardening region is linear

following the loading path. In the softening region, the unloading proceeds along a different linear path from the current position to the origin with a reduced stiffness given by the traction–displacement relation (line *BO*):

$$t = \sigma_{\max} \frac{\delta_{\max} - \delta_e}{\delta_c - \delta_e} \frac{\delta}{\delta_{\max}} \quad \forall \delta_c \le \delta_{\max} \le \delta_e \quad \text{and} \quad \delta \le \delta_{\max} \tag{3.54}$$

An irreversible damage path (*OBC*) is followed for reloading. Both normal and tangential tractions vanish when $\delta > \delta_e$. When the normal displacement is negative in compression, stiff penalty springs with high stiffness are introduced between the node pairs at the interface. The location of the separation at the debonding point is independent of the location of the peak of the curve for the bilinear model. This gives flexibility to adjust interfacial parameters for the peak and debonding locations to match the experimental observations as discussed in [34, 45].

In an incremental formulation, the complementary energy functional for each element in (3.24) is expressed in terms of the incremented stresses and displacements as

$$\begin{aligned}
&\Pi^{\mathrm{VCE}}_{e}\left(\sigma^m_{ij}, \Delta\sigma^m_{ij}, \sigma^c_{ij}, \Delta\sigma^c_{ij}, u^e_i, \Delta u^e_i, u^m_i, \Delta u^m_i, u^c_i, \Delta u^c_i\right) = \\
&-\int_{\Omega^{\mathrm{VCE}}_m \cup \Omega^{\mathrm{VCE}}_c} \frac{1}{2} S_{ijkl} \Delta\sigma_{ij} \Delta\sigma_{kl} \mathrm{d}\Omega - \int_{\Omega^{\mathrm{VCE}}_m \cup \Omega^{\mathrm{VCE}}_c} S_{ijkl} \Delta\sigma_{ij} \sigma_{kl} \mathrm{d}\Omega \\
&+\int_{\partial\Omega^{\mathrm{VCE}}_e} \left(\sigma^m_{ij} + \Delta\sigma^m_{ij}\right) n^e_j \left(u^e_i + \Delta u^e_i\right) \mathrm{d}\partial\Omega - \int_{\partial\Omega^m_c} \left(\sigma^m_{ij} + \Delta\sigma^m_{ij}\right) n^c_j \left(u^m_i + \Delta u^m_i\right) \mathrm{d}\partial\Omega \\
&+\int_{\partial\Omega^c_c} \left(\sigma^c_{ij} + \Delta\sigma^c_{ij}\right) n^c_j \left(u^c_i + \Delta u^c_i\right) \mathrm{d}\partial\Omega - \int_{\partial\Omega^{\mathrm{VCE}}_c} \int_{u^m_n - u^c_n}^{u^m_n + \Delta u^m_n - u^c_n - \Delta u^c_n} T^m_n \mathrm{d}\left(u^m_n - u^c_n\right) \mathrm{d}\partial\Omega \\
&-\int_{\partial\Omega^{\mathrm{VCE}}_c} \int_{u^m_t - u^c_t}^{u^m_t + \Delta u^m_t - u^c_t - \Delta u^c_t} T^m_t \mathrm{d}\left(u^m_t - u^c_t\right) \mathrm{d}\partial\Omega - \int_{\Gamma^{\mathrm{VCE}}_{im}} \left(t_i + \Delta t_i\right)\left(u^e_i + \Delta u^e_i\right) \mathrm{d}\Gamma
\end{aligned} \tag{3.55}$$

Terms $\frac{1}{2}\sigma_{ij}\mathbf{S}_{ijkl}\sigma_{kl}$ and $\frac{1}{2}\mathbf{S}_{ijkl}\Delta\sigma_{ij}\Delta\sigma_{kl} + \mathbf{S}_{ijkl}\Delta\sigma_{ij}\sigma_{kl}$ are the complementary energy density and its increment, respectively. The prefix $\Delta$ corresponds to increments, and subscripts *n* and *t* correspond to the normal and tangential directions at the matrix–inclusion interface. Here $\mathbf{n}^e$ and $\mathbf{n}^c$ are the outward normal on $\partial\Omega_e$ and $\partial\Omega_c$, respectively. The two terms on the matrix–inclusion interface $\partial\Omega^{\mathrm{VCE}}_c$ provide the work done by the interfacial tractions $\mathbf{T}^m = T^m_n \mathbf{n}^m + T^m_t \mathbf{t}^m$ due to interfacial separation $\left(\mathbf{u}^m - \mathbf{u}^c\right)$. The integration over the incremental displacements at the interface $\partial\Omega_c$ is conducted by the backward Euler method. The total energy functional for each *level-2* or *transition* element containing $N_{\mathrm{VCE}}$ Voronoi cell elements is obtained by adding individual element contributions as in (3.25).

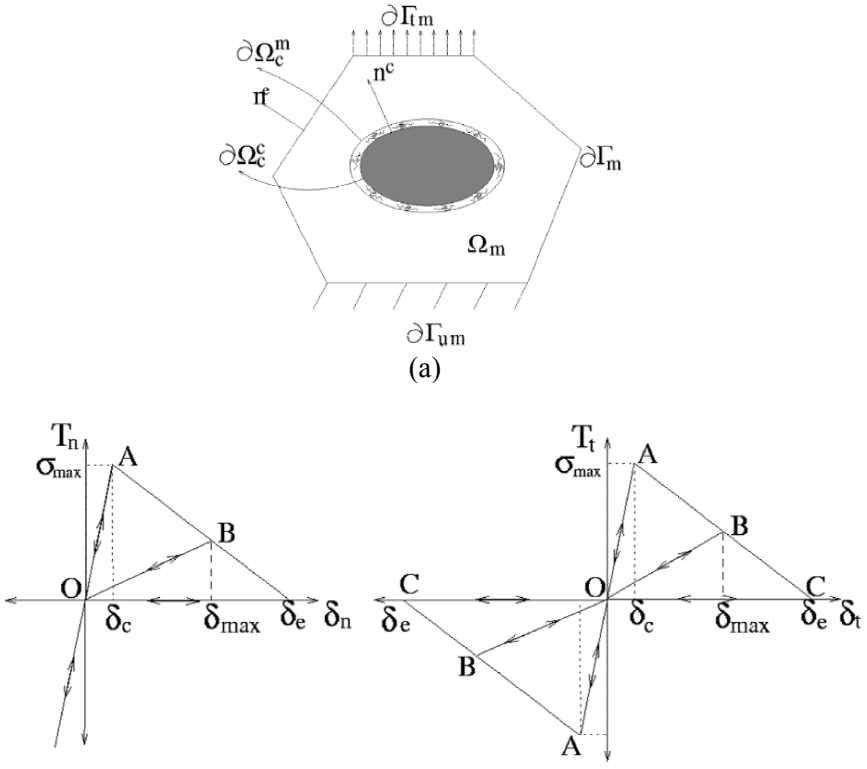


**Fig. 3.21.** (**a**) Voronoi cell FE with fiber–matrix interface using cohesive springs, (**b**) normal, and (**c**) tangential, traction–displacement behavior for bilinear cohesive zone model

Substituting stress and displacement increment interpolations of (3.26) in (3.71) and setting variations with respect to the stress coefficients $\Delta\boldsymbol{\beta}^m$ and $\Delta\boldsymbol{\beta}^m$, respectively, to zero, results in the weak form of the element kinematic relation, stated in a condensed matrix form as

$$\left[\mathbf{H}^e\right]\begin{Bmatrix}\boldsymbol{\beta}^m+\Delta\boldsymbol{\beta}^m\\ \boldsymbol{\beta}^c+\Delta\boldsymbol{\beta}^c\end{Bmatrix}=\left[\mathbf{G}^e\right]\begin{Bmatrix}\mathbf{q}^e+\Delta\mathbf{q}^e\\ \mathbf{q}^m+\Delta\mathbf{q}^m\\ \mathbf{q}^n+\Delta\mathbf{q}^n\end{Bmatrix}. \tag{3.56}$$

The weak forms of the global traction continuity conditions are subsequently solved by setting the variation of the total energy function,

with respect to $\Delta\mathbf{q}^e$, $\Delta\mathbf{q}^m$, and $\Delta\mathbf{q}^c$, to zero. This results in the weak form of the traction reciprocity conditions, stated in a condensed form as

$$\sum_{e=1}^{N_{ss}}\left[\mathbf{G}^e\right]\begin{Bmatrix}\boldsymbol{\beta}^m+\Delta\boldsymbol{\beta}^m\\ \boldsymbol{\beta}^c+\Delta\boldsymbol{\beta}^c\end{Bmatrix}=\sum_{e=1}^{N_{ss}}\left\{\mathbf{R}^e\right\}. \tag{3.57}$$

Substituting (3.56) into (3.57) yields

$$\sum_{e=1}^{N_{ss}}\left[\mathbf{G}^e\right]\left[\mathbf{H}^e\right]^{-1}\left[\mathbf{G}^e\right]\{\mathbf{q}+\Delta\mathbf{q}\}=\sum_{e=1}^{N_{ss}}\left\{\mathbf{R}^e\right\} \tag{3.58}$$

that is solved iteratively. Several numerical examples, validating this VCFE model, are solved in [34, 45].

As discussed in Sect. 3.3.2, the postprocessing phase for *level-1* elements requires the evaluation of different variables in the RVE from known values of macroscopic strains. A small variant of the formulation in (3.55) is needed for the energy functional of a SERVE ($\boldsymbol{Y}$). The functional with $Y$-periodic displacements, $Y$-antiperiodic tractions on the boundary and imposed macroscopic strain $(e_{ij}+\Delta e_{ij})$ is written as

$$\begin{aligned}\Pi_e=&-\int_{Y_m}\frac{1}{2}S^m_{ijkl}\Delta\sigma^m_{ij}\Delta\sigma^m_{kl}\mathrm{d}Y-\int_{Y_m}S^m_{ijkl}\sigma^m_{ij}\Delta\sigma^m_{kl}\mathrm{d}Y-\int_{Y_c}\frac{1}{2}S^c_{ijkl}\Delta\sigma^c_{ij}\Delta\sigma^c_{kl}\mathrm{d}Y\\&-\int_{Y_c}S^c_{ijkl}\sigma^c_{ij}\Delta\sigma^c_{kl}\mathrm{d}Y+\int_{\partial Y_e}\left(\sigma^m_{ij}+\Delta\sigma^m_{ij}\right)n^e_j\left(u^e_i+\Delta u^e_i\right)\mathrm{d}\partial\Omega\\&-\int_{\partial Y^m_c}\left(\sigma^m_{ij}+\Delta\sigma^m_{ij}\right)n^c_j\left(u^m_i+\Delta u^m_i\right)\mathrm{d}\partial\Omega+\int_{\partial Y^c_c}\left(\sigma^c_{ij}+\Delta\sigma^c_{ij}\right)n^c_j\left(u^c_i+\Delta u^c_i\right)\mathrm{d}\partial\Omega\\&-\int_{\partial Y_c}\int_{u^m_n-u^c_n}^{u^m_n+\Delta u^m_n-u^c_n-\Delta u^c_n}T^m_n\mathrm{d}\left(u^m_n-u^c_n\right)\mathrm{d}\partial\Omega-\int_{\partial Y_c}\int_{u^m_t-u^c_t}^{u^m_t+\Delta u^m_t-u^c_t-\Delta u^c_t}T^m_t\mathrm{d}\left(u^m_t-u^c_t\right)\mathrm{d}\partial\Omega\\&-\int_{Y_m}(e_{ij}+\Delta e_{ij})\Delta\sigma^m_{ij}\mathrm{d}\Gamma-\int_{Y_c}(e_{ij}+\Delta e_{ij})\Delta\sigma^c_{ij}\mathrm{d}\Gamma.\end{aligned} \tag{3.59}$$

The boxed term corresponds to the additional energy due to the imposed macroscopic strain field on $Y$. Euler–Lagrange equations for this functional are the multiscale kinematic relations,

$$\begin{aligned}&\varepsilon_{ij}(\mathbf{x},\mathbf{y})+\Delta\varepsilon_{ij}(\mathbf{x},\mathbf{y})=S_{ijkl}(\sigma_{ij}+\Delta\sigma_{ij})=(e_{ij}(\mathbf{x})+\Delta e_{ij}(\mathbf{x}))\\&+\frac{1}{2}\left[\frac{\partial(u_i(\mathbf{y})+\Delta u_i(\mathbf{y}))}{\partial y_j}+\frac{\partial(u_j(\mathbf{y})+\Delta u_j(\mathbf{y}))}{\partial y_i}\right]\quad\forall\mathbf{y}\in Y_m,Y_c\end{aligned} \tag{3.60}$$

### 3.4.2 Anisotropic CDM Model for *Level-0* Subdomain $\Omega^{l0}$

For microstructures with randomly evolving microcracks or debonding causing diffused damage, the homogenized material behavior is best represented by a CDM law [2, 12, 20, 76]. An anisotropic CDM model with a fourth-order damage tensor has been developed from rigorous micromechanical analyses in [36, 63]. The general form of CDM models [2, 42, 70, 75] introduce a fictitious effective stress $\tilde{\Sigma}_{ij}$ acting on an effective resisting area $\tilde{A}$, which is caused by reduction of the original resisting area $A$ due to material degradation from the presence of microcracks and stress concentration in the vicinity of cracks. The effective stress $\tilde{\Sigma}_{ij}$ is related to the actual Cauchy stress $\Sigma_{ij}$ through the relation $\tilde{\Sigma}_{ij} = M_{ijkl}(\mathbf{D})\Sigma_{kl}$, where $M_{ijkl}$ is a fourth-order damage effect tensor that is a function of the fourth-order damage tensor $\mathbf{D}(=D_{ijkl}\mathbf{e}_i \otimes \mathbf{e}_j \otimes \mathbf{e}_k \otimes \mathbf{e}_l)$. The hypothesis of equivalent elastic energy is used to evaluate $M_{ijkl}$, and hence establish a relation between the damaged and undamaged stiffnesses [15, 19, 80]. Equivalence is established by equating the elastic energy in the damaged state to that in a hypothetical undamaged state as

$$W(\boldsymbol{\Sigma}, \mathbf{D}) = \frac{1}{2}\Sigma_{ij}(E_{ijkl}(\mathbf{D}))^{-1}\Sigma_{kl} = W(\tilde{\boldsymbol{\Sigma}}, \mathbf{0}) = \frac{1}{2}\tilde{\Sigma}_{ij}(E^{\mathrm{o}}_{ijkl})^{-1}\tilde{\Sigma}_{kl}, \tag{3.61}$$

where $E^{\mathrm{o}}_{ijkl}$ is the elastic stiffness tensor in the undamaged state and $E_{ijkl}(\mathbf{D})$ is the stiffness in a damaged state. The relation between the damaged and undamaged stiffnesses is thus

$$E_{ijkl} = (M_{pqij})^{-1}E^{\mathrm{o}}_{pqrs}(M_{rskl})^{-1} \tag{3.62}$$

with an appropriate assumption of a function for $M_{ijkl}$, (3.62) can be used to formulate a damage evolution model using micromechanics and homogenization. A damage evolution surface is introduced to delineate the interface between damaged and undamaged domains in the strain $e_{ij}$-space as

$$F = \frac{1}{2}e_{ij}P_{ijkl}e_{kl} - \kappa(\alpha W_{\mathrm{d}}) = 0. \tag{3.63}$$

Here $W_{\mathrm{d}}\left(=\int \frac{1}{2}e_{ij}e_{kl}\mathrm{d}E_{ijkl}\right)$ corresponds to the dissipation of the strain energy density due to stiffness degradation for constant strain without an external work supply. Also called the degrading dissipation energy, it is an

internal variable denoting the current state of damage. $P_{ijkl}$ is a symmetric negative-definite fourth-order tensor that will be expressed as a function of the strain tensor $e_{ij}$, $\alpha$ is a scaling parameter and $\kappa$ is a function of $W_{\mathrm{d}}$. Assuming associativity rule in the stiffness space, the evolution of the fourth-order secant stiffness is obtained as

$$\dot{E}_{ijkl} = \dot{\lambda} \frac{\partial F}{\partial \left( \frac{1}{2} e_{ij} e_{kl} \right)} = \dot{\lambda} P_{ijkl}. \tag{3.64}$$

$P_{ijkl}(e_{mn})$ corresponds to the direction of the rate of stiffness degradation tensor $\dot{E}_{ijkl}$. For a composite material with interfacial debonding, the direction of rate of stiffness degradation varies with increasing damage and hence $P_{ijkl}(e_{mn})$ does not remain a constant throughout the loading process. The model requires the evaluation of $\kappa$, $\alpha$, and $P_{ijkl}$ in (3.63). These are determined from the results of VCFEM-based micromechanical simulations of an RVE with periodic boundary conditions. The function $\kappa(W_{\mathrm{d}})$ is evaluated for a reference loading path and all other strain paths are scaled with respect to this reference. Upon determination of the maximum value $W_{\mathrm{d}}$ for a reference loading condition, the value of $\alpha$ for any strain path can be obtained by simple scaling. To account for the variation of $P_{ijkl}(e_{mn})$, any macroscopic strain evolution path is discretized into a finite set of points. The values of $P_{ijkl}$ are explicitly evaluated at these points from RVE-based simulations. Values of $P_{ijkl}$ for any arbitrary macroscopic strain value can then be determined by interpolating between nodal values using shape functions of a 3D linear hexahedral element. Details of the parameter evaluation process in the macroscopic CDM model are discussed in [36, 63]. Gradients of important field variables are evaluated from macroscopic analysis using the CDM to assess the deviation of macroscopic uniformity. Such gradients may be the effect of microscopic nonhomogeneity in the form of highly localized stresses and strains or damage.

#### *Numerical example with the anisotropic CDM*

The macroscopic finite element model with its constitutive relations represented by the CDM model is validated by comparison of results with those obtained by homogenizing micromechanical solutions. The macroscopic model consists of a single QUAD4 element. For the

microstructure, a nonuniform RVE with 20 circular fibers of volume fraction 21.78% (see Fig. 3.22a) is constructed with periodic boundary. As explained in [62, 64] and Sect. 3.3.2 (Fig. 3.8b), a local microstructure is first constructed by repeating the set of randomly distributed fibers that lie in a window in both the $x$ and $y$ directions for several period lengths. The multifiber domain is tessellated into a network of Voronoi cells for the entire region, and the boundary of the RVE is generated as the aggregate of the outside edges of Voronoi cells associated with the original set of fibers. Periodicity constraint conditions on nodal displacements can then be easily imposed by constraining the node pairs to move identically.

The material properties of the elastic matrix (m) and fibers (f) and the cohesive zone model parameters are:

| $E_{\mathrm{m}}$ (GPa) | $\nu_{\mathrm{m}}$ | $E_{\mathrm{f}}$ (GPa) | $\nu_{\mathrm{f}}$ | $\delta_c$ (m) | $\delta_e$ (m) | $\sigma_{\max}$ (GPa) |
|---|---|---|---|---|---|---|
| 4.6 | 0.4 | 210.0 | 0.3 | $5.0\times10^{-5}$ | $20.0\times10^{-4}$ | 0.2 |

Three different macroscopic strain paths are considered for loading conditions, viz.:

(L1) $\varepsilon_{xx} \neq 0, \quad \varepsilon_{yy} = \varepsilon_{xy} = 0$

(L2) $\varepsilon_{xy} \neq 0, \quad \varepsilon_{yy} = \varepsilon_{xx} = 0$

(L3) $\varepsilon_{xx} = \varepsilon_{yy} = -\varepsilon_{xy} \neq 0$

The parameter $\kappa(W_{\mathrm{d}})$ is evaluated from the reference loading (L1) corresponding to uniaxial tension. The strain state (L2) corresponds to shear loading condition, while the load (L3) represents a combination of all strain components. The macroscopic stress–strain plots by the CDM model are compared with the homogenized micromechanical analyses results in Figs. 3.21b–d. All the nonzero stress components are plotted for each of the loading conditions, and excellent agreement is observed. In the shear loaded case, while $\sigma_{xx}$ and $\sigma_{yy}$ are zero prior to the onset of damage, they continue to increase with softening and debonding of the interface. This is due to the different interface behavior in tension and compression. For the combined straining case, a more complex stress–strain behavior is observed. The debonding initiation and propagation is dispersed in the microstructure with 20 fibers and hence a very gradual reduction of stiffness is observed. The homogenized CDM model developed, predicts the true macroscopic damage behavior with high accuracy and efficiency.

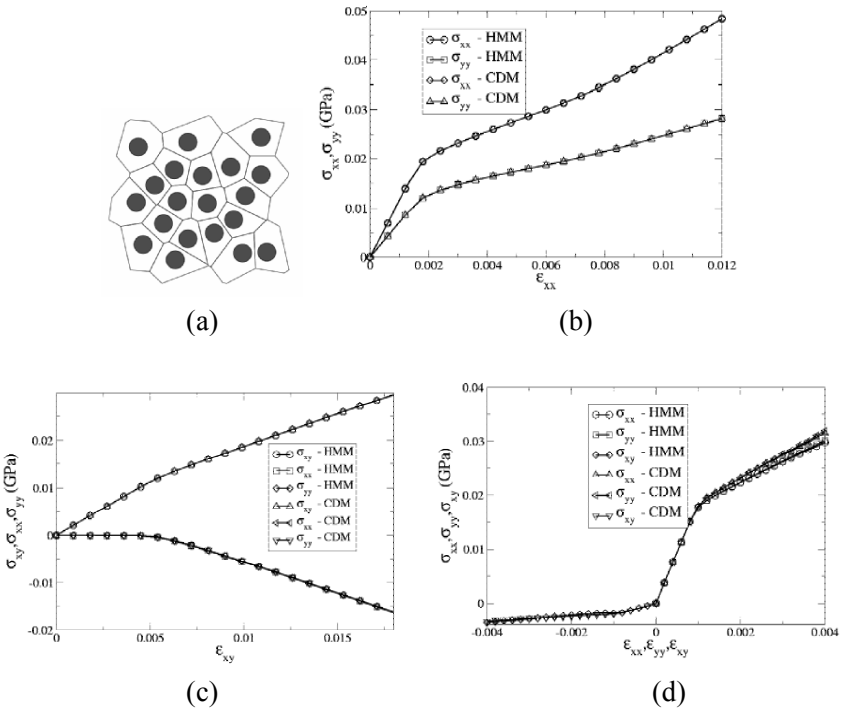


**Fig. 3.22.** Comparison of macroscopic stress–strain curves by CDM and homogenizing micromechanical solution: (**a**) a statistically equivalent RVE with 20 circular fibers, stress–strain plots for load cases, (**b**) L1, (**c**) L2, and (**d**) L3

### 3.4.3 Coupling Levels in the Concurrent Multiscale Algorithms

In a manner similar to Sect. 3.3.3, the incremental form of the equation of principle of virtual work equation for $\Omega_{\text{het}}$ at the end of an increment can be written as the sum of contributions from each individual domain as

$$\int_{\Omega_{10}} (\Sigma_{ij} + \Delta\Sigma_{ij}) \frac{\partial \delta u_i^{10}}{\partial x_j} \mathrm{d}\Omega - \int_{\Gamma_{10}} (t_i + \Delta t_i) \delta u_i^{10} \mathrm{d}\Gamma + \int_{\Omega_{11}} (\Sigma_{ij} + \Delta\Sigma_{ij}) \frac{\partial \delta u_i^{11}}{\partial x_j} \mathrm{d}\Omega$$

$$- \int_{\Gamma_{11}} (t_i + \Delta t_i) \delta u_i^{11} \mathrm{d}\Gamma + \int_{\Omega_{12}} (\sigma_{ij} + \Delta\sigma_{ij}) \frac{\partial \delta u_i^{12}}{\partial x_j} \mathrm{d}\Omega - \int_{\Gamma_{12}} \left(t_i + \Delta t_i\right) \delta u_i^{12} \mathrm{d}\Gamma$$

$$+ \int_{\Omega_{\text{tr}}} \sigma_{ij} \frac{\partial \delta u_i^{\text{tr}}}{\partial x_j} \mathrm{d}\Omega - \int_{\Gamma_{\text{tr}}} (t_i + \Delta t_i) \delta u_i^{\text{tr}} \mathrm{d}\Gamma$$

$$+ \delta \int_{\Gamma_{\text{int}}} \left(\lambda_i^{\text{tr}} + \Delta\lambda_i^{\text{tr}}\right) \left(v_i + \Delta v_i - u_i^{\text{tr}} - \Delta u_i^{\text{tr}}\right) \mathrm{d}\Gamma$$

$$+ \delta \int_{\Gamma_{\text{int}}} \left(\lambda_i^{10/11} + \Delta\lambda_i^{10/11}\right) \left(v_i + \Delta v_i - u_i^{10/11} - \Delta u_i^{10/11}\right) \mathrm{d}\Gamma = 0. \tag{3.65}$$

The discretized algebraic form of (3.65) is solved by using the Newton–Raphson iterative solver. Setting up the tangent stiffness matrix requires consistent linearization by taking directional derivative of (3.65) along incremental displacement vectors $\Delta\mathbf{u}$ and $\Delta\mathbf{v}$ and the Lagrange multipliers $\Delta\boldsymbol{\lambda}$. For the *i*th iteration in the solution of the incremental variables, assembled matrix equations have the following structure.

$$\begin{bmatrix} K^{\mathrm{I,I}}_{10/11} & K^{\mathrm{I,O}}_{10/11} & 0 & 0 & 0 & P_{10/11} & 0 \\ K^{\mathrm{O,I}}_{10/11} & K^{\mathrm{O,O}}_{10/11} & 0 & 0 & 0 & 0 & 0 \\ 0 & 0 & K^{\mathrm{I,I}}_{\mathrm{tr}} & K^{\mathrm{I,O}}_{12/\mathrm{tr}} & 0 & 0 & P_{\mathrm{tr}} \\ 0 & 0 & K^{\mathrm{O,I}}_{12/\mathrm{tr}} & K^{\mathrm{O,O}}_{12/\mathrm{tr}} & 0 & 0 & 0 \\ 0 & 0 & 0 & 0 & 0 & Q_{10/11} & Q_{\mathrm{tr}} \\ P^{\mathrm{T}}_{10/11} & 0 & 0 & 0 & Q^{\mathrm{T}}_{10/11} & 0 & 0 \\ 0 & 0 & P^{\mathrm{T}}_{\mathrm{tr}} & 0 & Q^{\mathrm{T}}_{\mathrm{tr}} & 0 & 0 \end{bmatrix}^{i} \begin{Bmatrix} \Delta\mathbf{q}^{\mathrm{I}}_{10/11} \\ \Delta\mathbf{q}^{\mathrm{O}}_{10/11} \\ \Delta\mathbf{q}^{\mathrm{I}}_{\mathrm{tr}} \\ \Delta\mathbf{q}^{\mathrm{O}}_{12/\mathrm{tr}} \\ \Delta\mathbf{q}_{\mathrm{int}} \\ \Delta\boldsymbol{\Lambda}_{10/11} \\ \Delta\boldsymbol{\Lambda}_{\mathrm{tr}} \end{Bmatrix}^{i} = \begin{Bmatrix} \Delta\mathbf{F}^{\mathrm{I}}_{10/11} \\ \Delta\mathbf{F}^{\mathrm{O}}_{10/11} \\ \Delta\mathbf{F}^{\mathrm{I}}_{\mathrm{tr}} \\ \Delta\mathbf{F}^{\mathrm{O}}_{12/\mathrm{tr}} \\ \Delta\mathbf{F}_{\mathrm{int}} \\ \Delta\mathbf{F}_{\lambda^{10/11}} \\ \Delta\mathbf{F}_{\lambda^{12/tr}} \end{Bmatrix}^{i} . \tag{3.66}$$

All the components have the same meaning as explained in Sect. 3.3.3. The stiffness $K_{12/\mathrm{tr}}$ and the load vector $\Delta\mathbf{F}_{12/\mathrm{tr}}$ for *level-2* and transition elements are obtained by VCFEM calculations followed by static condensation to represent the virtual work in terms of the boundary terms only.

### 3.4.4 Adaptation Criteria for Mesh Refinement and Level Change

The following criteria are used for mesh-refinement and level transitions due to discretization and modeling error, respectively, in the multilevel model. Many of these adaptation criteria are physically based, depending on the problem in consideration, since rigorous mathematical error bounds may not even exist for these nonlinear problems with damage. Consequently, other indicators may be used as appropriate.

#### *Refinement of level-0 and level-1 meshes by h-adaptation*

Computational models in *level-0* and *level-1* subdomains are enriched by *h-adaptation* to reduce discretization "error" and to identify regions of modeling error by zooming in on regions of localization with high gradients. For simulations using the CDM model, the adaptation criterion is formulated in terms of the traction jump across adjacent element boundaries, representing local stress gradients. The condition is stated as:

Refine element *"k,"* if the traction jump error satisfies the condition

$$E_k^{ij} \geq C_1 * E_{\text{avg}}^{ij}, \quad \text{where} \quad E_{\text{avg}}^{ij} = \left( \frac{\sum_{i=1}^{\text{NE}} \left( E_k^{ij} \right)^2}{\text{NE}} \right)^{1/2}$$
$$\text{and} \quad (E^{ij})_k^2 = \frac{\int_{\partial\Omega_e} \left( [[T_x]]^2 + [[T_y]]^2 \right) \text{d}\partial\Omega}{\int_{\partial\Omega_e} \text{d}\partial\Omega}. \tag{3.67}$$

Here NE is the total number of *level-0* and *level-1* elements in the entire computational domain, $T_x$, $T_y$ are the components of element boundary tractions in the $x$ and $y$ directions, and [[ ]] is the jump operator across element boundary $\partial\Omega_e$. $C_1 < 1$ is chosen from numerical experiments.

### *Criteria for switching from level-0 to level-1 elements*

*Level-0* to *level-1* element transition takes place according to criteria signaling the departure from conditions of homogenizability. The criteria are based on macroscopic variables in the CDM model of *level-0* elements. The degrading dissipation energy $W_{\text{d}}$ is a strong indicator of localized damage evolution and hence, a criterion is formulated as:

Switch element "$k$" from *level-0* to *level-1* if:

$$E_k^{\text{gde}} * (W_{\text{d}})_k > C_2 * E_{\text{max}}^{\text{gde}} * (W_{\text{d}})_{\text{max}}, \tag{3.68}$$

where $E_k^{\text{gde}}$ is the norm of the local gradient of $(W_{\text{d}})_k$, expressed as $E_e^{\text{gde}} = \sqrt{\left( \frac{\partial (W_{\text{d}})_e}{\partial x_1} \right)^2 + \left( \frac{\partial (W_{\text{d}})_e}{\partial x_2} \right)^2}$, $E_{\text{max}}^{\text{gde}}$ is the maximum value of $E_k^{\text{gde}}$ in all elements and $C_2 (< 1)$ is a prescribed tolerance. The criterion (3.68) is helpful for seeking out regions with high gradients of $W_{\text{d}}$ in regions of high $W_{\text{d}}$ itself. The local gradient is accurately evaluated using the Zienkiewicz–Zhu (ZZ) gradient patch recovery method [81], where $W_{\text{d}}$ is interpolated using a polynomial function over a patch of elements connected to a nodal point. The gradients of $W_{\text{d}}$ in each element are calculated from the nodal values using element shape functions.

### *Criteria for switching from level-1 to level-2 elements*

For elements in which macroscopic uniformity does not hold in the sense of (3.68), departure from RVE periodicity condition is used to trigger a

switch from *level-1* to *level-2*. The switching criterion is developed in terms of evolving variables, e.g., the average strain at the fiber–matrix interface in the local microstructural RVE. The average strain is defined as

$$D_{ij} = \frac{1}{\int_{\cup \partial\Omega_c} \mathrm{d}\partial\Omega} \int_{\cup \partial\Omega_c} \varepsilon_{ij} \mathrm{d}\partial\Omega = \frac{1}{\int_{\cup \partial\Omega_c} \mathrm{d}\partial\Omega} \int_{\cup \partial\Omega_c} ([u_i]n_j + [u_j]n_i) \mathrm{d}\partial\Omega, \quad (3.69)$$

where the integral is evaluated over all fiber–matrix interfaces in the RVE. The jump in displacement across the fiber–matrix interface with a normal $n_i$ is denoted by $[u_i]$. For perfect interfaces $[u_i]$ will be zero. Thus, $D_{ij}$ corresponds to the contributions to the macroscopic strain due to damage only, since $D_{ij} = 0$ in the absence of damage. Departure from periodicity will result in a significantly altered averaged strain $D_{ij}$ in response to different conditions on the boundary of the microstructural region. For example, let $D_{ij}^{e,l2}$ correspond to a solution of the boundary value problem of the local microstructure included in a *level-2* element (see Fig. 3.12), subject to boundary displacements that have been obtained from macroscopic *level-0/level-1* analysis. The microstructural scale is explicit in this analysis, since periodicity is not imposed on the boundary. On the other hand, let $D_{ij}^{e,\mathrm{RVE}}$ be from the solution of a boundary value problem of the local RVE with imposed macroscopic strains and subjected to periodic boundary displacements constraints. The difference in these two strains for a *level-1* element *k* is quantified as

$$E_k^{\mathrm{dper}} = \max\left(\left|D_{11}^{k,l2} - D_{11}^{k,\mathrm{RVE}}\right|, \left|D_{22}^{k,l2} - D_{22}^{k,\mathrm{RVE}}\right|, \left|D_{12}^{k,l2} - D_{12}^{k,\mathrm{RVE}}\right|\right). \quad (3.70)$$

For evaluating $D_{ij}^{e,l2}$ in the incremental solution, only the increments in the present step are calculated by the *level-1* macroscopic displacement boundary conditions. It is assumed that the RVE-based solution is valid all the way up to (but excluding) the present step. The departure from periodicity is measured in terms of the difference in averaged strains $E_e^{\mathrm{dper}}$. The criterion thus reads:

Switch element "*k*" from *level-1* to *level-2* if:

$$E_e^{\mathrm{dper}} > C_3 D_{\max}^{\mathrm{RVE}}, \quad (3.71)$$

where $D_{\max}^{\mathrm{RVE}}$ is the maximum value of $D_{ij}^{k,\mathrm{RVE}}$ in all *level-1* elements.

*Remark*: Once the level-2 and transition elements have been identified, it is important to update the local states of stress, strain, and damage to the

current state. This step should precede the coupled concurrent analysis. For this analysis, the history of the macroscopic displacement solution on the boundaries of the *level-0/level-1* elements is used. The local micromechanical (VCFEM) boundary value problem for the *level-2* element is incrementally solved from the beginning to obtain the stress, strain, and damage history in the microstructure from the macroscopic boundary displacement history.

### 3.4.5 Numerical Examples with the Adaptive Multilevel Model

Two numerical examples are solved to study the effectiveness of the multilevel computational model in analyzing damage in composite materials.

#### *Multilevel model vs. micromechanical analysis*

This example is aimed at establishing the effectiveness of the multilevel model in analyzing a nonuniform composite microstructure by comparing its predictions with those by pure micromechanical analysis. It is computationally intensive to conduct the reference micromechanical analysis with evolving damage for very large microstructural regions. Consequently, a computational domain with a small population of fibers, as shown in the optical micrograph of Fig. 3.23a, is considered. The polymer matrix composite micrograph has a random dispersion of uniaxial fibers. The dimensions of the micrograph analyzed are $100\,\mu\text{m} \times 70.09\,\mu\text{m}$, containing 264 circular fibers. Each fiber has a diameter of $1.645\,\mu\text{m}$ for a total volume fraction of 32%. Though the domain is not adequate for a clear separation between continuum and micromechanical regions (since relatively large regions are needed to realize an RVE), the results of this example show the effectiveness of the overall framework.

The optical micrograph is mapped onto a simulated microstructure with circular fibers that is tessellated into a mesh of 264 Voronoi cell elements, shown in Fig. 3.23b. The constituent materials are an epoxy resin matrix, stainless steel reinforcing fibers, and a very thin film of freekote ($< 0.1\,\mu\text{m}$) at the fiber–matrix interface. The freekote imparts weak strength to the steel–epoxy interface, which allows a stable growth of the debond crack for experimental observation. The experimental methods of material and interface characterization have been discussed in [34]. Both the matrix and fiber materials are characterized by isotropic elasticity properties, viz. $E_{\text{epoxy}} = 4.6\,\text{GPa}$, $\nu_{\text{epoxy}} = 0.4$, $E_{\text{steel}} = 210\,\text{GPa}$, $\nu_{\text{steel}} = 0.3$.

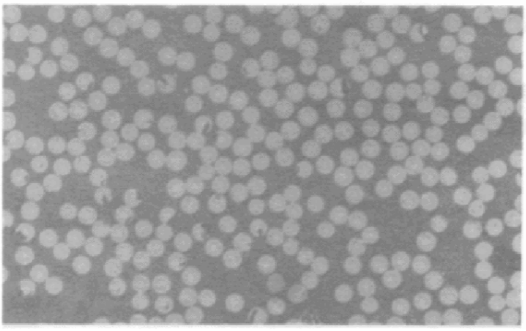

(a)

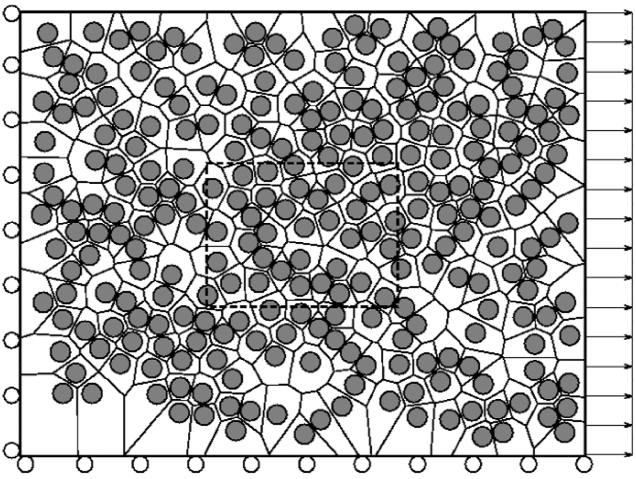

(b)

**Fig. 3.23.** (**a**) Optical micrograph of a steel fiber–epoxy matrix composite with 264 fibers and (**b**) the simulated computational model with a Voronoi cell mesh

The cohesive model properties are: $\delta_c = 5.1e-5m$, $\delta_e = 3.1e-4m$, and $\sigma_{\max} = 0.005\,\text{GPa}$. The micrograph is stretched in horizontal tension by 20 equal increments of $0.1\,\mu\text{m}$, to a total strain of $\varepsilon_{xx} = 0.1\%$. The displacement is imposed on the right edge, as shown in Fig. 3.23b.

The pure micromechanical VCFEM solution using the mesh of Fig. 3.23b is presented in [45] and is used here as reference solutions for the multiscale simulation. Figure 3.26a shows the contour plot of microscopic stress $\sigma_{xx}$ at the final step of the micromechanical simulation, with a depiction of interfacial debonding. The right side of the microstructure

shows significant localized damage. Debonding initiates at the top and percolates to the bottom of the microstructure along a narrow band. Multiscale analysis is performed by the concurrent multilevel model and the results are compared with those from the micromechanical VCFEM analysis. For the multilevel model, the entire computational region of 264 fibers is first divided into nine macroscopic finite elements as shown in Fig. 3.24a. For evaluating the homogenized constitutive properties for each element, the statistically equivalent representative volume element, or SERVE, for the microstructure underlying each macroscopic element is first identified. Statistical methods for identification of the SERVE have been discussed in Sect. 3.3.2.3 and also in [13, 32, 33, 60, 69, 72, 73]. However, since the number of fibers in the micrograph is limited in this exercise, the SERVE for each element is assumed to consist of all the fibers belonging to that element. For example, to generate the SERVE for an element window in the micrograph of Fig. 3.23b, all fibers whose centers are located within this window are first identified as constituents of the RVE and the SERVE is then created. The number of fibers and their distribution in the SERVE of each macroscopic element is shown in Fig. 3.24a.

The number of elements is only nine in this example. Consequently, *level-0* simulations with the CDM model are bypassed, and all elements are *level-1* at the start of the multilevel simulation. The factor $C_3$ in (3.71) is taken as 0.2. However the $D_{ij}^{k,l2} - D_{ij}^{k,\mathrm{RVE}}$ terms for each element in (3.70) are replaced by the difference in RVE-based averaged strains between adjacent elements, i.e., $D_{ij}^{e1,\mathrm{RVE}} - D_{ij}^{e2,\mathrm{RVE}}$. Also, instead of transition elements, a single layer of microscopic Voronoi cell elements is included for transitioning between the *level-1* and *level-2* elements. In Fig. 3.24b the Voronoi elements containing the grey fibers constitute the *transition* layer, while those containing the black fibers belong to *level-2*. An interface segment $\Gamma_{\mathrm{int}}$ is inserted between the *transition* and *level-1* elements at a distance $\mathbf{L}_{\mathrm{tr}/l2}$ from the right edge. Convergence properties of the multilevel model are studied for two cases, viz. $\mathbf{L}_{\mathrm{tr}/l2} / \mathbf{L} = 0.35$ and $\mathbf{L}_{\mathrm{tr}/l2} / \mathbf{L} = 0.45$. This is achieved by changing the initial *level-1* element size.

In Fig. 3.24b, only three elements (3, 6, and 9) on the right side of the initial mesh switch from *level-1* to *level-2*. A comparison of results by (a) VCFEM-based micromechanical analyses (all *level-2* elements), (b) homogenization-based macroscopic analysis (all *level-1* elements), and (c) concurrent multilevel analysis (*level-1* and *level-2* elements) is made.

Contour plots of $\sigma_{11}$ (GPa) showing interfacial debonding at the end of the simulation are shown in Fig. 3.24b, c. The discrepancy between the

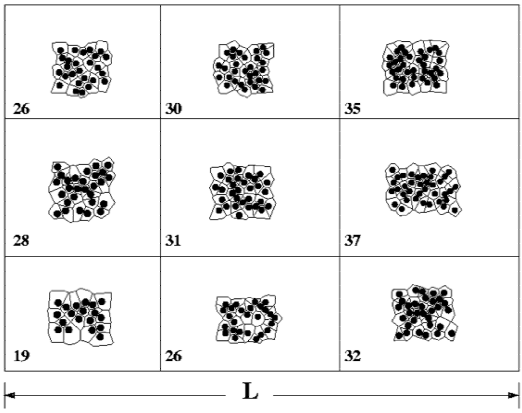


(a)

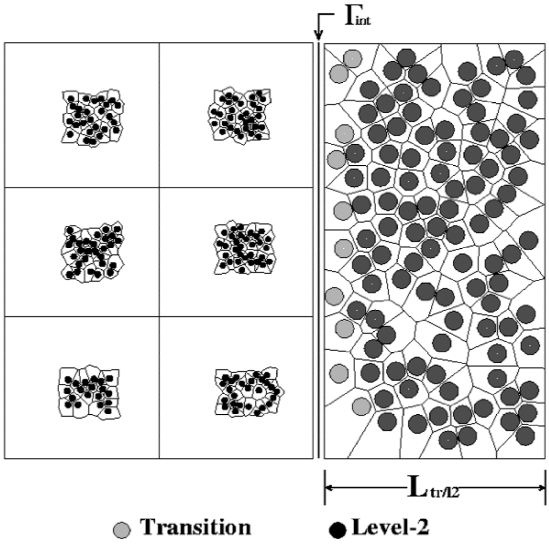


(b)

**Fig. 3.24.** Mesh for the computational domain: (**a**) macroscopic mesh with different RVE in every element and (**b**) multilevel model with the interface between macroscopic and microscopic VCFE elements

damage paths predicted by the micromechanical and the multilevel analyses reduces sharply with increasing $\mathbf{L}_{\mathrm{tr}/l2}/\mathbf{L}$ value. This can be attributed to the fact that the damage path is very sensitive to the macro–micro interface conditions. Since the sample size is small and there is no real periodicity in the microstructure, the proximity of the *level-1* boundary to the damage localization zone alters the local boundary conditions. However, as this distance is increased, the microscopic stress distribution, debonding pattern and damage zone replicates the micromechanical analysis results. This is due to the fact that the damage localization has little effect on the *level-1/level-2* boundary with increasing distance. The distribution of the micromechanical stresses $\sigma_{11}$, generated by pure micromechanical and multilevel analyses, is plotted along a line through the middle of the micrograph in Fig. 3.25. The micromechanical stresses show only minor oscillations about an average value of 0.005 GPa in the region to the left of the *level-1–level-2* interface. In the region to the right, where damage is predominant, there is clearly convergence of the stresses with increasing $\mathbf{L}_{\mathrm{tr}/l2}/\mathbf{L}$ value. The macroscopic or averaged stress–strain response for element 1 (always *level-1*) and element 9 (changes levels) are plotted in Fig. 3.25. The volume averaged stresses and strains are evaluated by averaging the local fields over the microscopic domain as

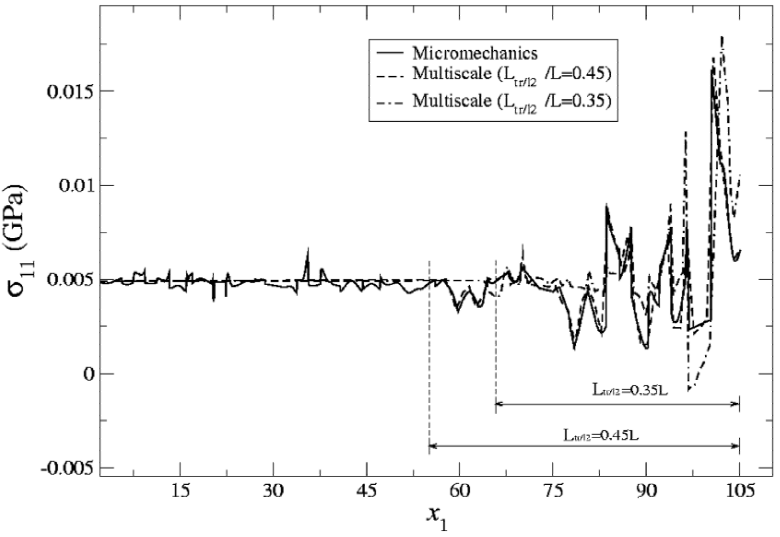


**Fig. 3.25.** Comparison of microscopic stress $\sigma_{11}$ by different methods along a line through the middle of microstructure

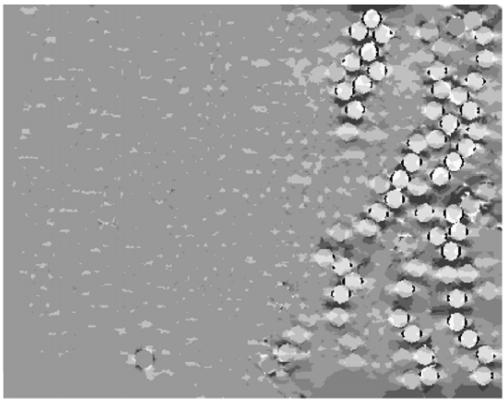

(a)

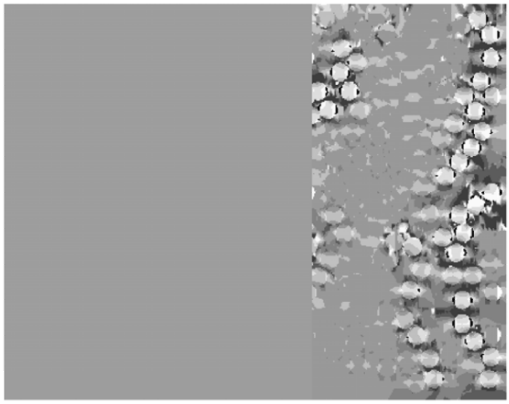

(b)

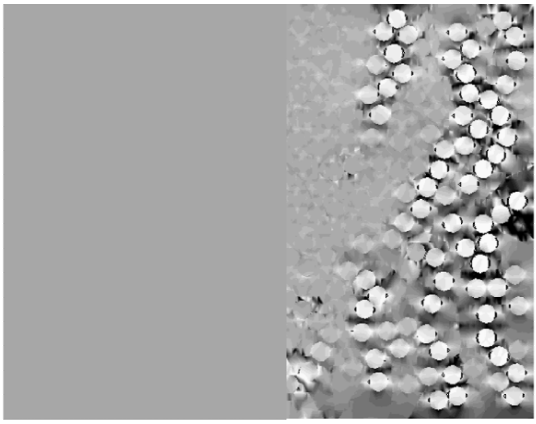

(c)

**Fig. 3.26.** Contour plot of $\sigma_{11}$ showing interfacial debonding at the end of simulation for: (**a**) pure micromechanical analysis, (**b**) multiscale analysis with $\mathbf{L}_{\mathrm{tr}/l2} / \mathbf{L} = 0.35$, and (**c**) multiscale analysis with $\mathbf{L}_{\mathrm{tr}/l2} / \mathbf{L} = 0.45$

$$\Sigma_{ij} = \frac{1}{\Omega}\int_{\Omega} \sigma_{ij}(x_1, x_2)\mathrm{d}\Omega \quad \text{and} \quad e_{ij=} \frac{1}{\Omega}\int_{\Omega} \varepsilon_{ij}(x_1, x_2)\mathrm{d}\Omega - D_{ij}, \tag{3.72}$$

where $D_{ij}$ is the strain jump defined in (3.68). The results for all the models are in good agreement for element 1, where there is no significant microstructural damage. The small difference is due to the periodicity constraints imposed on the microstructure. Also, there is a difference between the results of $\mathbf{L}_{\mathrm{tr}/l2}/\mathbf{L} = 0.35$ and $\mathbf{L}_{\mathrm{tr}/l2}/\mathbf{L} = 0.45$, due to the interface conditions at $\Gamma_{\mathrm{int}}$. However, as is expected, the results are quite different for element 9, where significant damage is observed in Fig. 3.26. The *level-1* analysis shows significant deviation from the micromechanical analysis due to imposed periodicity in the damage zone. Once again, the results improve significantly with increasing $\mathbf{L}_{\mathrm{tr}/l2}/\mathbf{L}$ ratio.

### *A composite double lap joint with microstructural debonding*

The double lap bonded adhesive joint with boron–epoxy composites, discussed in Sect. 3.4.3, is again analyzed with interfacial damage. An adhesive, ABCD in Fig. 3.27a, is used to bond the two composite materials. Both plies above and below the adhesive are made of uni-directional boron fiber–epoxy matrix composite materials. The fibers are uniformly arranged in a square array, implying a square unit cell with a single circular fiber of $V_{\mathrm{f}} = 20\%$. The epoxy matrix and boron fibers have the same properties as described in the previous section. The material properties of the isotropic adhesive and the bilinear cohesive law parameters for the matrix–fiber interface are:

| $E_{\mathrm{adhesive}}$ (GPa) | $\nu_{\mathrm{adhesive}}$ | $\delta_c$ (m) | $\delta_e$ (m) | $\sigma_{\max}$ (GPa) |
|---|---|---|---|---|
| 4.6 | 0.4 | $5.0\times10^{-5}$ | $20.0\times10^{-4}$ | 0.2 |

Only a quarter of the joint is modeled from considerations of symmetry in boundary and loading conditions. In the model, the top ply above the adhesive is assumed to consist of ten rows of fiber, while the bottom row consists of five rows resulting in a total of 450 fibers. The number of fibers is kept low, so that a reference micromechanical analysis can be easily done for this example with a mesh of 450 Voronoi elements (square unit cell). The displacement component is $u_1 = 0$ along the face $x_2 = 0$ due to

symmetry about the $x_2$ axis. The displacement components along the face $x_1 = 8h$ are $u_1 = 0$ and $u_2 = 0$ corresponding to a fixed edge. A total tensile displacement $u_1 = 1.2 \times 10^{-3} h$ is applied on the face of the lower ply at $x_1 = 0$ in 15 uniform increments. Three different approaches are used to solve this problem (1) a macroscopic model using the CDM model, (2) a detailed micromechanical VCFEM analysis, and (3) multiscale analysis by the multilevel model.

The starting mesh in the multilevel model of the bonded joint consists of a uniform grid of 470 QUAD4 elements for macroscopic analysis as shown in Fig. 3.27b. The constitutive relation for each element is a fourth-order anisotropic CDM model developed for this unit cell with interfacial cohesive zone in [63]. Figure 3.27d shows the gradient of the dissipation energy, i.e., $\nabla W_d$, at the final stage of loading. Damage initiates near the bottom left corner A of the adhesive joint and propagates downward to span the entire region on the left of point A. Level transition parameters are $C_2 = 0.5$ and $C_3 = 0.1$. The corresponding evolution of various levels

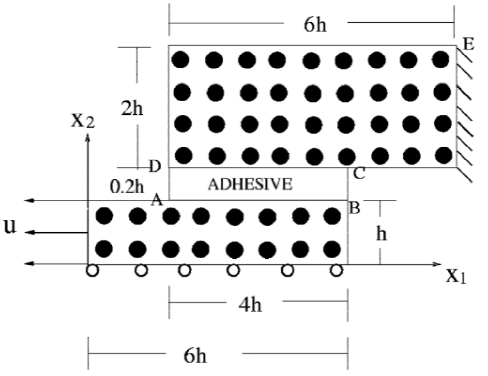


(a)

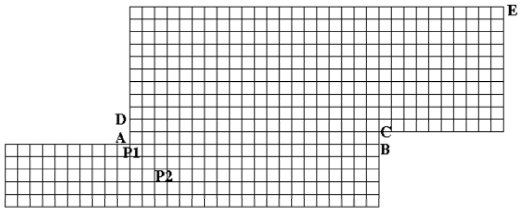


(b)

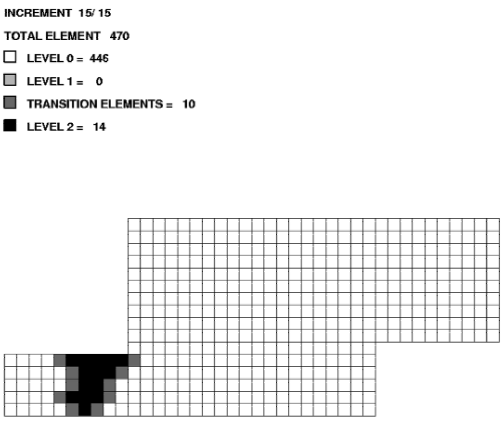


(c)

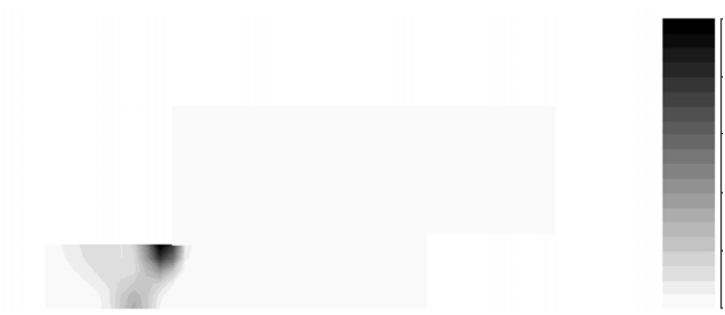

(d)

**Fig. 3.27.** (**a**) A composite double lap joint, (**b**) *level-0* computational mesh, (**c**) evolution of the multilevel computational model with level transition at the final loading stage, and (**d**) contour plot of dissipation energy gradient $\nabla W_{\mathrm{d}}$

in the model is depicted in Fig. 3.27c. At the final step, the multilevel mesh consists of 446 *level-0* elements, 0 *level-1* elements, 14 *level-2* elements, and 10 *transition* elements. All *level-2* elements emerge in critical regions where both $\nabla W_{\mathrm{d}}$ and $W_{\mathrm{d}}$ are high.

Figure 3.28a, b depicts the contours of microscopic stress $\sigma_{11}$ and the regions of debonding. The results of the multilevel model are in excellent agreement with the micromechanical analysis, both with respect to

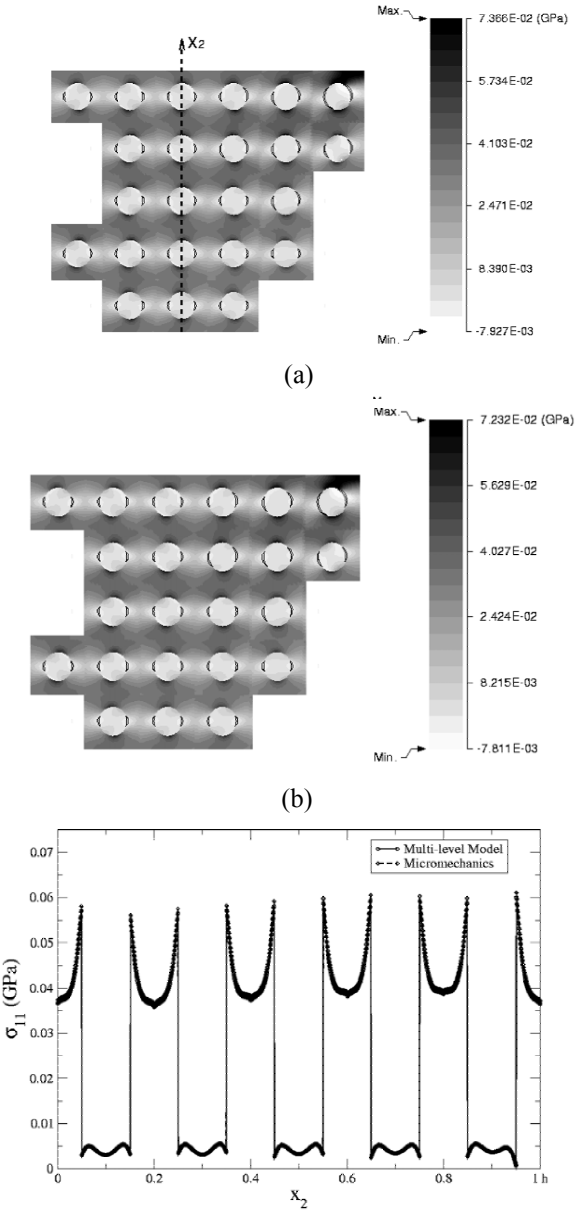


**Fig. 3.28.** *Level-2* solution near the corner A showing microscopic stress distribution (GPa) and interfacial debonding at the end of the analysis by: (**a**) pure micromechanical analysis, (**b**) multiscale analysis, and (**c**) comparison of $\sigma_{11}$ along the vertical line through the microstructure by multilevel and micromechanical analysis

debonding regions and evolving variables. The maximum error in $\sigma_{11}$ is around 1%. The excellent agreement is further corroborated in the plot of $\sigma_{11}$ along the vertical line through the microstructure in Fig. 3.28c. Figure 3.29a shows the macroscopic $\Sigma_{11}$– $e_{11}$ plots obtained from (a) macroscopic CDM-based analysis, (b) micromechanical analysis followed by

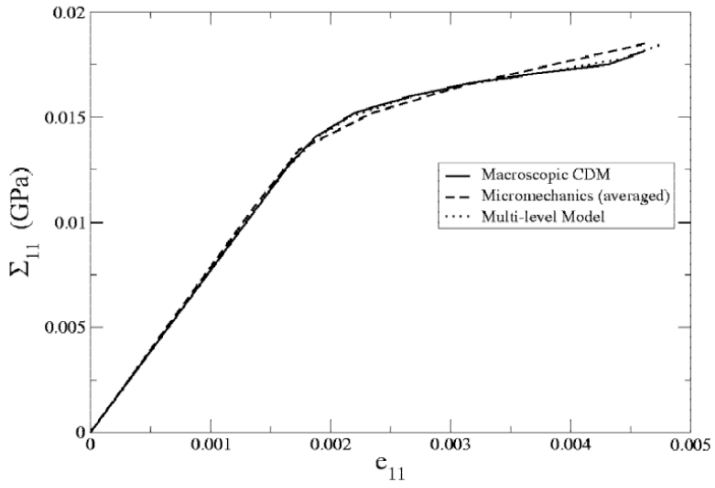


(a)

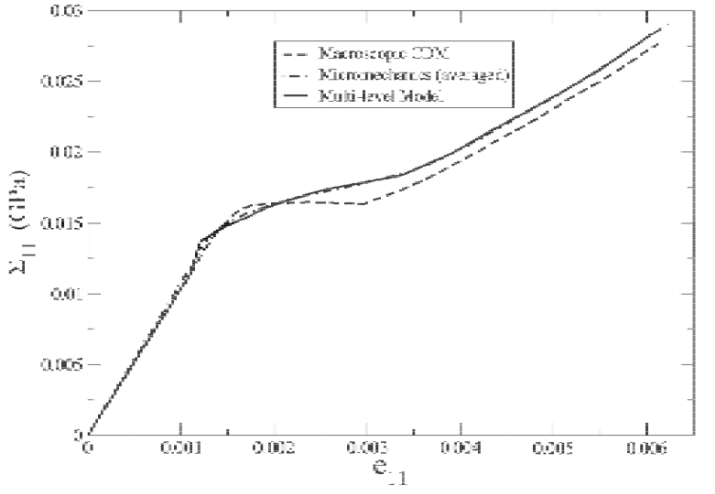


(b)

**Fig. 3.29.** Macroscopic $\Sigma_{11} - e_{11}$ plot by different methods at: (**a**) P2 and (**b**) P1

averaging, and (c) multiscale analysis with the multilevel model at two different locations, P1 and P2 shown in Fig. 3.27b. At P2, with low damage and its gradient, solutions by the CDM model and micromechanics are in relatively good agreement. At this point, the multiscale model uses the CDM constitutive law. However, the CDM results are quite different from the other two at P1, a hotspot where the damage and its gradient are high. The multilevel model and micromechanics results match quite well here.

Computational efficiency of the multilevel model is examined by a comparison of the CPU time on an IA32 computer cluster for the different models. The relative CPU times are as follows: (1) 71 s for all *level-0*, (2) 300,330 s for all *level-1*, (3) 300,310 s for all *level-2*, and (4) 42,260 s for the multilevel model. Although the macroscopic CDM analysis is faster, it can lead to significant errors. The complete *level-1* solution is even slower than the micromechanics solution. Accurate analysis with the multilevel model is at least seven times faster than the complete micromechanics and *level-1* solutions. The efficiency increases rapidly with increasing number of fibers in the analysis as shown in [36].

## 3.5 Conclusions

A comprehensive framework for adaptive concurrent multilevel computational analysis is developed in this chapter for multiscale analysis of fiber-reinforced composite materials with damage prediction. While, microstructural damage is manifested by fiber–matrix interfacial debonding here, any possible mode, e.g., multicrack evolution [46], can be incorporated into this framework. The multilevel model invokes two-way coupling of scales, viz. a bottom-up coupling with homogenization at lower scales to introduce reduced order continuum models and a top-down coupling at critical hot spots to transcend scales for following the microstructural damage evolution. Adaptive capabilities enable effective domain decomposition in the evolving problem with damage, keeping a balance between computational efficiency and accuracy. Numerical examples establish the accuracy and efficiency aspects of the model, as well as demonstrate its capability in handling problems involving large composite domains. Overall, this work lays an effective foundation for solving multiscale problems involving localization, damage, and crack evolution that may be impossible to achieve using any single scale model.

## Acknowledgments

This work has been supported by the Air Force Office of Scientific Research (Program Director: Dr. B. L. Lee). This sponsorship is gratefully acknowledged. Computer support by the Ohio Supercomputer Center is also gratefully acknowledged. The author would like to thank his graduate students P. Raghavan, H. Bhatnagar, J. Bai, J. Jain, S. Manchiraju, G. Venkatramani, and K. Kennedy for their help with the results and editing of this document.

Figures 3.1–3.19 in this chapter are reprinted from*: Journal*: Computer Methods in Applied Mechanics and Engineering, *Vol.* 193(6–8), *Authors*: P. Raghavan and S. Ghosh, *Title of article*: Concurrent multiscale analysis of elastic composites by a multilevel computational model, *Copyright year* (2004) with permission from Elsevier. Figures 3.20 and 3.21 are reprinted from: *Journal*: Mechanics of Materials, *Vol.* 37 (9), *Authors*: P. Raghavan and S. Ghosh, *Title of article*: A continuum damage mechanics model for unidirectional composites undergoing interfacial debonding, *Copyright year* (2005) with permission from Elsevier.

## References

1. Ainsworth M, Oden JT (1992) A procedure for a posteriori error estimation for hp-finite element methods. Comput Meth Appl Mech Engng 101:73–96
2. Allen DH (2002) Homogenization principles and their application to continuum damage mechanics. Comp Sci Tech 61:2223–2230
3. Allen DH, Yoon C (1998) Homogenization techniques for thermoviscoelastic solids containing cracks. Int J Solids Struct 35:4035–4054
4. Aminpour MA, Ransom JB, McCleary SL (1995) A coupled analysis method for structures with independently modeled finite element subdomains. Int J Num Meth Engng 38:3695–3718
5. Argon AS, Im J (1975) Separation of second phase particles in spheroidized 1045 steel, Cu-0.6Cr alloy, and maraging steel in plastic straining. Metall Trans 6A:839–851
6. Babuska I, Strouboulis T, Upadhyay CS, Gangaraj SK (1995) A-posteriori estimation and adaptive control of the pollution error in the h-version of the finite element method. Int J Numer Meth Engng 38:4208–4235
7. Benssousan A, Lions JL, Papanicoulau G (1978) Asymptotic Analysis for Periodic Structures. North Holland, Amsterdam
8. Benveniste Y (1987) A new approach to the application of Mori–Tanaka's theory in composite materials. Mech Mater 6:147–157

9. Boehm HJ (2004) A short introduction to continuum micromechanics. In: Boehm HJ (ed) Mechanics of Microstructured Materials, CISM Courses and Lectures, Vol 464. Int Centre for Mech Sci, Springer Wien, NY, pp 1–40
10. Boehm HJ, Rammerstoffer FG, Weissenbek E (1993) Some simple models for micromechanical investigations of fiber arrangement effects in MMC's. Comp Mater Sci 1:177–194
11. Budiansky B (1965) On the elastic moduli of some heterogeneous materials. J Mech Phys Solids 13:223–227
12. Bulsara VN, Talreja R, Qu J (1999) Damage in ceramic matrix composites with arbitrary microstructures. ASME MD 80:441–446
13. Bulsara VN, Talreja R, Qu J (1999) Damage initiation under transverse loading of unidirectional composites with arbitrarily distributed fibers. Comp Sci Tech 59:673–682
14. Chen HS, Acrivos A (1978) The effective elastic moduli of composite materials containing spherical inclusions at non-dilute concentrations. Int J Solids Struct 14:349–364
15. Chow CL, Wang J (1987) An anisotropic theory of elasticity for continuum damage mechanics. Int J Frac 20:381–390
16. Christensen RM, Lo KH (1979) Solutions for effective shear properties in three phase sphere and cylinder models. J Mech Phys Solids 27:315–330
17. Chung PW, Tamma KK, Namburu RR (2000) A finite element thermo-viscoelastic creep for heterogeneous structures with dissipative correctors. Finite Elem Anal Des 36:279–313
18. Clyne TW, Withers PJ (1993) An Introduction to Metal Matrix Composites. Cambridge University Press
19. Cordebois JP, Sidoroff F (1982) Anisotropic damage in elasticity and plasticity. J Mech Theor Appl 45–60
20. Costanzo F, Boyd JG, Allen DH (1996) Micromechanics and homogenization of inelastic composite materials with growing cracks. J Mech Phys Solids 44(3):333–370
21. Devries F, Dumontet H, Duvaut G, Lene F (1989) Homogenization and damage for composite structures. Int J Num Meth Engng 27:285–298
22. Eshelby JD (1957) The determination of the elastic field of an ellipsoidal inclusion and related problems. Proc R Soc (London) A 241:376–396
23. Fish J, Belsky V (1995) Multigrid method for periodic heterogeneous media, part II: multiscale modeling and quality control in multidimensional case. Comp Meth Appl Mech Engng 126:17–38
24. Fish J, Shek K (2000) Multiscale analysis of composite materials and structures. Comp Sci Tech 60:2547–2556
25. Fish J, Yu Q, Shek K (1999) Computational damage mechanics for composite materials based on mathematical homogenization. Int. J Num Meth Engng 45:1657–1679
26. Ghosh S, Moorthy S (1998) Particle fracture simulation in non-uniform microstructures of metal–matrix composites. Acta Mater 46:965–982

27. Ghosh S, Moorthy S (2004) Three dimensional Voronoi cell finite element model for modeling microstructures with ellipsoidal heterogeneities. Comput Mech 34 (6):510–531
28. Ghosh S, Mukhopadhyay SN (1991) A two dimensional automatic mesh generator for finite element analysis of random composites. Comp Struct 41:245–256
29. Ghosh S, Raghavan P (2004) Multiscale model for damage analysis in fiber reinforced composites with interfacial debonding materials. Int J Multiscale Comp Engng 2(4):621–645
30. Ghosh S, Lee K, Moorthy S (1995) Multiple scale analysis of heterogeneous elastic structures using homogenization theory and Voronoi cell finite element method. Int J Solids Struct 32:27–62
31. Ghosh S, Lee K, Moorthy S (1996) Two scale analysis of heterogeneous elastic-plastic materials with asymptotic homogenization and Voronoi cell finite element model. Comp Meth Appl Mech Engng 132:63–116
32. Ghosh S, Nowak Z, Lee K (1997) Quantitative characterization and modeling of composite microstructures by Voronoi cells. Acta Mater 45:2215–2234
33. Ghosh S, Nowak Z, Lee K (1997) Tessellation based computational methods for the characterization and analysis of heterogeneous microstructures. Comp Sci Tech 57:1187–1210
34. Ghosh S, Ling Y, Majumdar BS, Kim R (2000) Interfacial debonding in multiple fiber-reinforced composites. Mech Mater 32:561–591
35. Ghosh S, Lee K, Raghavan P (2001) A multi-level computational model for multiscale damage analysis in composite and porous materials. Int J Solids Struct 38(14):2335–2385
36. Ghosh S, Bai J, Raghavan P (2007) Concurrent multi-level model for damage evolution in microstructurally debonding composites. Mech Mater 39(3):241–266
37. Guedes JM, Kikuchi N (1991) Preprocessing and post processing for materials based on the homogenization method with adaptive finite element methods. Comp Meth Appl Mech Engng 83:143–198
38. Guo BQ, Babuska I (1986), The h–p version of the finite element method: Part I: The basic approximation results. Comp Mech 1:21–41
39. Hashin Z, Strikman S (1963) A variational approach to the theory of the elastic behavior of multiphase materials. J Mech Phys Solids 11:127–140
40. Hill R (1965) A self consistent mechanics of composite materials. J Mech Phys Solids 13:213–222.
41. Hill R (1967) The essential structure of constitutive laws for metal composites and polycrystals. J Mech Phys Solids 15:79–95
42. Kachanov LM (1987) Introduction to Continuum Damage Mechanics. Martinus Nijhoff, Dordrecht, Netherlands
43. Lee K, Ghosh S (1996) Small deformation multiscale analysis of heterogeneous materials with the Voronoi Cell finite element model and homogenization theory. Comp Mater Sci 7:131–146

44. Lene F (1986) Damage Constitutive Relations for Composite Materials. Engng Fract Mech 25(5):713–728
45. Li S, Ghosh S (2004) Debonding in composite microstructures with morphological variations. Int J Comput Meth 1(1):121–149
46. Li S, Ghosh S (2006) Extended Voronoi cell finite element model for multiple cohesive crack propagation in brittle materials. Int J Numer Meth Engng 65:1028–1067
47. Lions JL (1980) On some homogenization problems. Z Angew Math Mech 62:251–262
48. Moorthy S, Ghosh S (1996) A model for analysis of arbitrary composite and porous microstructures with Voronoi cell finite elements. Int J Numer Meth Engng 39:2363–2398
49. Moorthy S, Ghosh S (1998) A Voronoi cell finite element model for particle cracking in composite materials. Comp Meth Appl Mech Engng 151:377–400
50. Moorthy S, Ghosh S (2000) Adaptivity and convergence in the Voronoi cell finite element model for analyzing heterogeneous materials. Comp Meth Appl Mech Engng 185:37–74
51. Morgan RC, Babuska I (1991) An approach for constructing families of homogenized equations for periodic media, Part I: An integral representation and its consequences: SIAM J Math Anal 22:1–15
52. Mura T (1987) Micromechanics of Defects in Solids, 2nd edn. Kluwer Academic Publishers, Dordrecht
53. Nemat-Nasser S, Yu N, Hori M (1993) Bounds and estimates of overall moduli of composites with periodic microstructure. Mech Mater 15:163–181
54. Oden JT, Feng Y (1996) Local and pollution error estimation for finite element approximations of elliptic boundary value problems. J Comp Appl Math 74:245–293
55. Oden JT, Zohdi TI (1997) Analysis and adaptive modeling of highly heterogeneous elastic structures. Comput Meth Appl Mech Engng 148:367–391
56. Oden JT, Vemaganti K, Moes N (1999) Hierarchical modeling of heterogeneous solids. Comput Meth Appl Mech Engng 172:3–25
57. Ortiz M, Pandolfi (1999) A finite-deformation irreversible cohesive element for three-dimensional crack-propagation analysis. Int J Numer Meth Eng 44:1267–1282
58. Pagano NJ, Rybicki EF (1974) On the significance of effective modulus solutions for fibrous composites. J Comp Mater 8:214–228
59. Pagano NJ, Yuan FG (2000) Significance of effective modulus theory (homogenization) in composite laminate mechanics. Comp Sci Tech 60:2471–2488
60. Pyrz R (1994) Correlation of microstructure variability and local stress field in two-phase materials. Mat Sci Eng A 177:253–259
61. Raghavan P, Ghosh S (2004) Adaptive multiscale computational modeling of composite materials. Comp Model Engng Sci 5(2):151–170

62. Raghavan P, Ghosh S (2004) Concurrent multiscale analysis of elastic composites by a multi-level computational model. Comp Meth Appl Mech Engng 193(6–8):497–538
63. Raghavan P, Ghosh S (2005) A continuum damage mechanics model for unidirectional composites undergoing interfacial debonding. Mech Mater 37 (9):955–979
64. Raghavan P, Moorthy S, Ghosh S, Pagano NJ (2001), Revisiting the composite laminate problem with an adaptive multi-level computational model. Comp Sci Tech 61:1017–1040
65. Raghavan P, Li S, Ghosh S (2004) Two scale response and damage modeling of composite materials. Finite Elem Anal Des 40(12):1619–1640
66. Rastogi N, Soni SR, Nagar A (1998) Thermal stresses in aluminum-to-composite double-lap bonded joints. Adv Engng Software 29:273–281
67. Rybicki EF, Pagano NJ (1976) A study of the influence of microstructure on the modified effective modulus approach for composite laminates. In: Proceedings of the 1975 Int Conf Comp Mater 2, pp 198–207
68. Sanchez-Palencia E (1980) Non-homogeneous media and vibration theory. (Lecture notes in Physics, Vol 127, Springer, Berlin Heidelberg New York)
69. Shan Z, Gokhale AM (2002) Representative volume element for non-uniform micro-structure. Comp Mater Sci 24:361–379
70. Simo JC, Ju JW (1987) Strain and stress-based continuum damage models, Part I: Formulation. Int J Solids Struct 23(7):821–840
71. Smit RJM, Brekelmans WAM, Meijer HEH (1998) Prediction of the mechanical behavior of nonlinear heterogeneous systems by multi-level finite element modeling. Comp Meth Appl Mech Engng 155(1–2):181–192
72. Swaminathan S, Ghosh S, Pagano NJ (2006) Statistically equivalent representative volume elements for composite microstructures, Part I: Without damage. J Comp Mater 40(7):583–604
73. Swaminathan S, Ghosh S, Pagano NJ (2006) Statistically equivalent representative volume elements for composite microstructures, Part II: With evolving damage. J Comp Mater 40(7):605–621
74. Szabo B, Babuska I (1991) Finite Element Analysis. John Wiley & sons
75. Talreja R (1991) Continuum modeling of damage in ceramic matrix composites. Mech Mater 12:165–180
76. Talreja R (1994) Damage Mechanics of Composite Materials. Elsevier Science Ltd
77. Tamma KK, Chung PW (1999) Woven Fabric Composites: Developments in Engineering Bounds, Homogenization and Applications. Int J Numer Meth Engng 45:1757–1790
78. Terada K, Kikuchi N (2000) Simulation of the multiscale convergence in computational homogenization approaches. Int J Solids Struct 37:2285–2311
79. Vemaganti K, Oden JT (2001) Estimation of local modeling error and goal-oriented adaptive modeling of heterogeneous materials, Part II: a computational environment for adaptive modeling of heterogeneous elastic solids. Comp Meth Appl Mech Engng 190:6029–6214

80. Zhu YY, Cescotto S (1995) A fully coupled elasto-visco-plastic damage theory for anisotropic materials. Int J Solids Struct 32 (11):1607–1641
81. Zienkiewicz OC, Zhu JZ (1992) The super-convergence patch recovery and a posteriori error estimates, Part 1: The recovery technique. Inter J Numer Methods Engrg 33:1331–1364
82. Zohdi TI, Wriggers P (1999) A domain decomposition method for bodies with heterogeneous microstructure based on material regularization. Int J Solids Struct 36:2507–2525
83. Zohdi TI, Wriggers P (2004) Introduction to Computational Micromechanics. (Lecture Notes in Applied and Computational Mechanics, Vol 20)
84. Zohdi TI, Oden JT, Rodin GJ (1999) Hierarchical modeling of heterogeneous solids. Comput Meth Appl Mech Engng 172:3–25